Alexander Prüll

Monte Carlo Simulations for Manganites

DISSERTATION

zur Erlangung des akademischen Grades

Doktor der Technischen Wissenschaften

eingereicht an der

Technischen Universität Graz

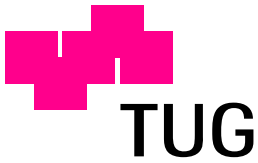

Begutachter:

Univ.-Prof.Dipl.-Ing.Dr. Wolfgang von der Linden
Institut für Theoretische Physik
Technische Universität Graz

Univ.-Prof.Mag.Dr. Wolfgang Ernst
Institut für Experimentalhysik
Technische Universität Graz

Februar 2003

Abstract

Manganese oxides such as $La_{1-x}Sr_xMnO_3$ and $La_{1-x}Ca_xMnO_3$ have been attracting considerable attention since the discovery of colossal magnetoresistance. In this theoretical work we investigate the ferromagnetic (FM) Kondo model with classical corespins, which covers several aspects of these materials. This is done by the use of several approximation schemes.

First an effective spinless fermion model for strong Hund coupling is derived with a projection technique. The complexity of the model is thereby drastically reduced, though the main physical properties are maintained. Thorough Monte Carlo simulations show the reliability of this approach for both static and dynamic variables.

In a second step, we introduce what we call uniform hopping approach (UHA). The influence of the fluctuating spins is replaced by mean values of certain parameters, which again simplifies the system enormously. The main aspects of the Kondo model are captured in regions of the parameters, where the system is homogeneous.

Calculations for the FM Kondo model revealed features which have often been interpreted as phase separation in the literature. Our analysis of Monte Carlo data rather supports the formation of FM polarons. To stress this point, we further improve UHA to deal even with the inhomogeneous case of polarons. This picture is able to describe even dynamical features like the spectral density of the original Kondo model in simple physical terms.

Zusammenfassung

Durch die Entdeckung des kolossalen Magnetowiderstandes in einigen Manganoxyden, wie $La_{1-x}Sr_xMnO_3$ und $La_{1-x}Ca_xMnO_3$ sind diese Materialien in den Blickpunkt wissenschaftlichen Interesses gerückt. In dieser theoretischen Arbeit untersuchen wir das ferromagnetische (FM) Kondo-Modell mit klassischen Corespins, das einige der Aspekte dieser Materialien beschreibt. Dazu wenden wir mehrere Approximationen an.

Als ersten Schritt leiten wir mittels Projektortechnik ein spinloses Fermionen Modell ab. Dieses in seiner Komplexität stark reduzierte Modell zeigt nach wie vor quantitativ die wesentliche Physik, wie ausführliche Monte Carlo Simulationen zeigen.

Weiters führen wir den "uniform hopping approach" (UHA) ein, der den Einfluss der fluktuierenden Corespins durch Mittelwerte gewisser Parameter ersetzt, was eine weitere drastische Reduktion der Komplexität bewirkt. Parameterbereiche des Kondo-Modells, die zu einem homogenen System führen, werden dadurch gut beschrieben.

Gewisse Merkmale, die Rechnungen zum FM Kondo-Modell enthüllten, wurden in der Literatur oft als Phasenseparation gedeutet. Die Analyse unserer Monte Carlo Daten deutet jedoch eher auf FM Polaronen hin. Um diese Fakten zu untermauern, erweitern wir das UHA, um auch den inhomogenen Fall der Polaronen zu inkludieren. In diesem polaronischen Bild lassen sich sogar dynamische Observable wie die Spektraldichte physikalisch anschaulich deuten.

Contents

Chapter 1

Introduction

First[1] interest was drawn on manganites when Jonker and van Santen [3] revealed the existence of ferromagnetism in mixed crystals of $LaMnO_3$-$SrMnO_3$, $LaMnO_3$-$CaMnO_3$, and $LaMnO_3$-$BaMnO_3$ in 1950. In their paper and in many other studies on manganese oxides the chemical formula is $T_{1-x}D_xMnO_3$, where T is a trivalent rare earth or Bi^{3+} cation, and D is a divalent alkaline or Pb^{2+} cation. Oxygen is in a O^{2-} state, and the abundance of Mn^{4+} and Mn^{3+} is regulated by x.

A second boom on manganites started in the 1990's. Large magnetoresistance (MR) effects were found in several manganese oxides [4, 5]. The DC resistivity changes remarkably when a magnetic field is applied. However, in manganites relatively large magnetic fields of about 1 Tesla are necessary, which makes technical application rather unlikely. In what follows we want to focus on $La_{1-x}Sr_xMnO_3$ (LSMO), which is the compound with the largest bandwidth and is the most canonical double-exchange (DE) system.

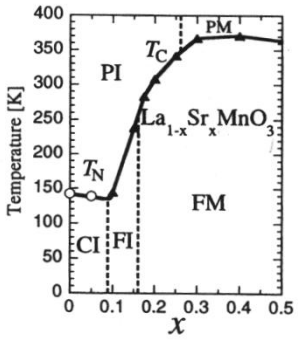

Figure 1.1: *Phase diagram of $La_{1-x}Sr_xMnO_3$ in the plane of doping concentration x and temperature [6]. Abbreviations: PI, paramagnetic insulating; PM, paramagnetic metallic; CI, spin-canted insulating; FI, ferromagnetic insulating.*

[1] after [1, 2]

Figure 1.1 shows the phase diagram of LSMO. At hole concentrations $x \approx 0.4$ the compound is a metal ($d\rho_{\rm dc}/dT > 0$) both at low temperature and high temperature. In this region there is a transition from ferromagnetic (FM) order to paramagnetism at a relatively high Curie temperature $T_C \approx 350$ K. At lower hole concentration $x \lesssim 0.3$, the state above the Curie temperature becomes a paramagnetic insulator. This curious behavior is a key property of all manganites. At densities $x \lesssim 0.17$ even the low temperature state is an insulating one. Between $x \simeq 0.08$ and $x \simeq 0.17$ a FM insulating state develops below T_C, whereas below $x \simeq 0.08$ the low temperature state is a spin-canted state.

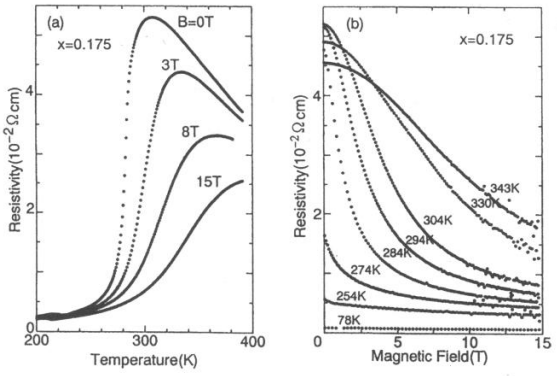

Figure 1.2: *Magnetic-field effects on the resistivity of* $La_{1-x}Sr_xMnO_3$ *(*$x = 0.174$*) crystal [7]: (a)* T *dependence of resistivity; (b) isothermal magnetoresistance.*

In Fig. 1.2 the MR effect is illustrated. The magnetic field greatly reduces the resistivity near T_C by shifting the resistivity maximum to a higher temperature due to suppression of the spin-scattering of the carriers. The MR effect is maximized in the density region separating the insulating from metallic states at low temperature [7], $x \simeq 0.175$. Thus a profound knowledge of the competing mechanisms which lead to the different phases of manganites seems to be necessary in order to understand the MR effect.

This theses is organized as follows. In Chapter 2 both the lattice and the electronic structure of LSMO is discussed. From the analysis of d electrons in a cubic lattice the derivation of model Hamiltonians is sketched. Chapter 3 outlines some basic physical properties of the model Hamiltonians. The influence of the various degrees of freedom such as orbitals, spins, and phonons is discussed. The remaining Chapters are papers submitted to Phys. Rev. B. An effective spinless fermion model is derived in Chapter 5 [8]. By means of the projection perturbation theory the dimensionality of the Hamiltonian can be reduced drastically. An additional simplification for $T = 0$ calculations is introduced through the uniform hopping approach (UHA). Chapter 6 further improves the UHA allowing for finite temperature calculations [9]. By this means the phase diagram of the 3D DE model is calculated and compared to

experimental data. Coulomb interactions can be included in calculations easily because of the reduction of the Hilbert space. A simple polaronic model is introduced in Chapter 7 in order to explain some of the physical properties in simple terms [10]. A comparison of the simple model with full Monte Carlo (MC) simulations in 1D reveal that at low and high carrier concentrations small polarons form and determine the physics of the systems. Spin-spin correlations, charge-charge correlations, and spectral functions can be described within this picture.

Chapter 2

Structure and Hamiltonians

This chapter follows primary the review article [11] and the article [12]. In the first Section the lattice structure and the electronic structure of LSMO is discussed. The cubic symmetry of the lattice influences strongly the electronic behavior. The second Section tries to motivate the specific shape of the model Hamiltonians used to describe manganites.

2.1 Structure

$La_{1-x}Sr_xMnO_3$ (LSMO) crystallizes in a three-dimensional perovskite structure displayed in Fig. 2.1. The manganese ions (Mn^{3+} or Mn^{4+}, depending on the Sr doping concentration x) generate a cubic lattice. The bridge positions between two nearest neighbor manganese ions are occupied by oxygen ions (O^{2-}) forming octahedra. The lanthanum ions (La^{3+}) or alternatively the strontium ions (Sr^{2+}) lie in the body center of manganese cubes. However, this high symmetry is not stable. The existence of degenerate electronic orbitals in a structure of high symmetry leads to a distortion of the lattice (Jahn-Teller effect [13], Sec. 3.2). The degeneracy is lifted by this mechanism [14]. We introduce the phononic contributions to the Hamiltonian which account for the Jahn-Teller effect in Sec. 2.2.3.

2.1.1 The Electronic Structure

Mn^{3+} (Mn^{4+}) has four (three) electrons in $3d$-states, the other electrons are in closed shells (argon configuration). The cubic symmetry of the compound influences the character of d-states. In order to reveal their behavior we consider a cubic representation of the d-orbitals. This partially lifts the degeneracy of the d-levels known as crystal-field splitting.

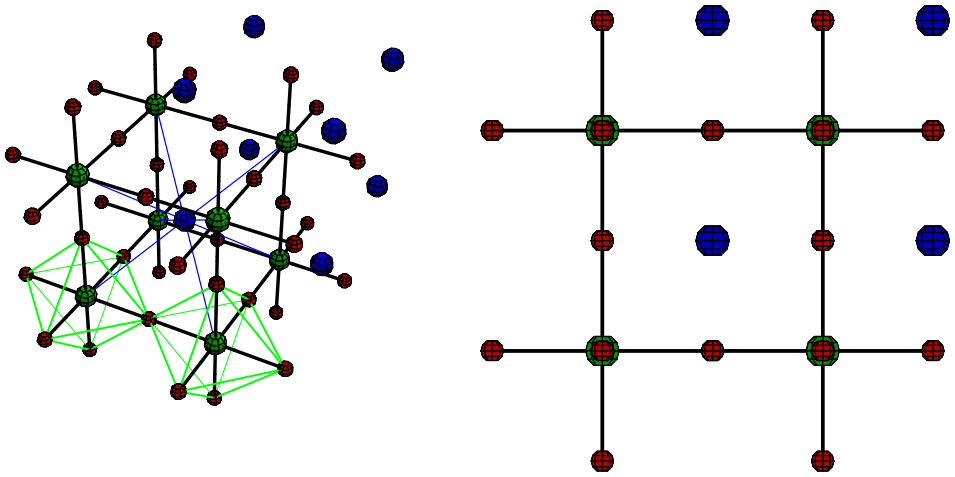

Figure 2.1: *The structure of $La_{1-x}Sr_xMnO_3$. The oxygen ions (red balls) form octahedra around the manganese ions (green balls). The manganese ions form cubes with the lanthanum ions or the strontium ions (blue balls) positioned in their centers. The black lines indicate the paths where the itinerant electrons (e_g) can move. It should be mentioned that the MnO_6 octahedra are distorted due to phononic interactions (Jahn-Teller effect, Sec. 3.2).*

e_g- and t_{2g}-Orbitals

The angular part of the wave functions of the d-states can be described by spherical harmonics $Y_{l=2}^m(\vartheta,\varphi)$ where $m \in \{-2,-1,0,1,2\}$:

$$Y_2^{-2} = \sqrt{\frac{15}{32\,\pi}}\,\sin^2(\vartheta)\,\exp(-2\,i\,\varphi) \qquad \propto \qquad (x-iy)^2\,, \tag{2.1a}$$

$$Y_2^{-1} = \sqrt{\frac{15}{8\,\pi}}\,\cos(\vartheta)\,\sin(\vartheta)\,\exp(-i\,\varphi) \qquad \propto \qquad (x-iy)z\,, \tag{2.1b}$$

$$Y_2^{\ 0} = \sqrt{\frac{5}{16\,\pi}}\,\left(3\,\cos^2(\vartheta)-1\right) \qquad \propto \qquad 3z^2-r^2\,, \tag{2.1c}$$

$$Y_2^{+1} = \sqrt{\frac{15}{8\,\pi}}\,\cos(\vartheta)\,\sin(\vartheta)\,\exp(i\,\varphi) \qquad \propto \qquad (x+iy)z\,, \tag{2.1d}$$

$$Y_2^{+2} = \sqrt{\frac{15}{32\,\pi}}\,\sin^2(\vartheta)\,\exp(2\,i\,\varphi) \qquad \propto \qquad (x+iy)^2\,. \tag{2.1e}$$

Substituting Cartesian coordinates x, y, z, and r for ϑ and φ

$$\begin{aligned} x &= \sin(\vartheta)\cos(\varphi)\,,\\ y &= \sin(\vartheta)\sin(\varphi)\,,\\ z &= \cos(\vartheta)\,,\\ r^2 &= x^2+y^2+z^2 = 1 \end{aligned} \tag{2.2}$$

yields the results given on the right hand side of equations (2.1). The orbitals are visualized in Fig. 2.2. Note that orbitals with equal $|m|$ look identical.

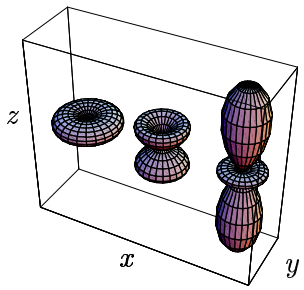

Figure 2.2: *The orbitals belonging to the spherical harmonics with l=2 (d-electrons). From left to right:* $|Y_2^{\pm 2}|^2$, $|Y_2^{\pm 1}|^2$, *and* $|Y_2{}^0|^2$.

However, the choice of the spherical harmonics as a basis of all d-configurations is not optimal in sight of the cubic symmetry of the perovskite structure. To deal with the symmetry we introduce the following linear combination of spherical harmonics

$$\frac{1}{\sqrt{2}}\left(Y_2^{-1} + Y_2^{+1}\right) \quad \propto \quad yz\ , \tag{2.3a}$$

$$\frac{1}{\sqrt{2}}\left(Y_2^{-1} - Y_2^{+1}\right) \quad \propto \quad zx\ , \tag{2.3b}$$

$$\frac{1}{\sqrt{2}}\left(Y_2^{-2} - Y_2^{+2}\right) \quad \propto \quad xy\ . \tag{2.3c}$$

These three states, called t_{2g}-sates, form a subspace of the d-configurations which is invariant under the application of the cubic symmetry group. This can be seen both from the right hand side of Eq. (2.3), and the graphical representation depicted in the left panel of Fig. 2.3. Note that the optical

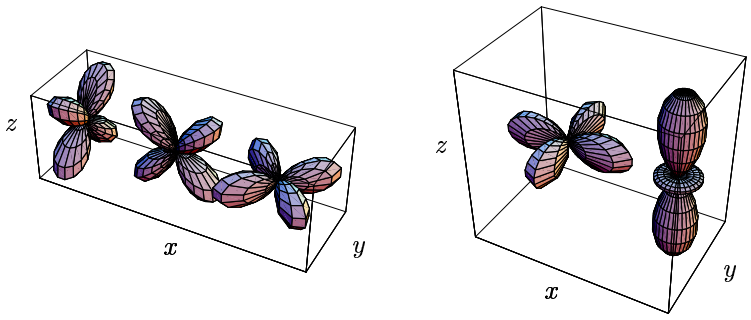

Figure 2.3: *The* t_{2g}*- (left) and* e_g*- (right) orbitals.*

appearance of the states can be derived easily from their representation in Cartesian coordinates.

The remaining two orthogonal states

$$\psi_2 := \frac{1}{\sqrt{2}}(Y_2^{-2} + Y_2^{+2}) \qquad \propto \qquad x^2 - y^2 \,, \tag{2.4a}$$

$$\psi_3 := Y_2^0 \qquad \propto \qquad 3z^2 - r^2 \tag{2.4b}$$

are called e_g-orbitals. They too span a subspace which is invariant under cubic transformations as can be verified effortlessly. For example, rotating $\psi_2 \propto (x^2 - y^2)$ around the x-axes by $\pi/2$ results in $(x^2 - z^2) \propto 1/2\,\psi_2 - \sqrt{3}/2\,\psi_3$. Analogous one can show the other invariances. The right hand side of Fig. 2.3 shows these orbitals.

In order to derive certain contributions to the model Hamiltonian (see Sec. 2.2) of manganites it is advantageous to introduce an over-complete basis in the e_g-space

$$\psi_x := \frac{\sqrt{3}}{2}\psi_2 - \frac{1}{2}\psi_3 \qquad \propto \qquad 3x^2 - r^2 \,, \tag{2.5a}$$

$$\psi_y := -\frac{\sqrt{3}}{2}\psi_2 - \frac{1}{2}\psi_3 \qquad \propto \qquad 3y^2 - r^2 \,, \tag{2.5b}$$

$$\psi_z := \psi_3 \qquad \propto \qquad 3z^2 - r^2 \,. \tag{2.5c}$$

These states have the advantage of being extended merely along one specific Cartesian axis, as can be seen in the left hand panel of Fig. 2.4.

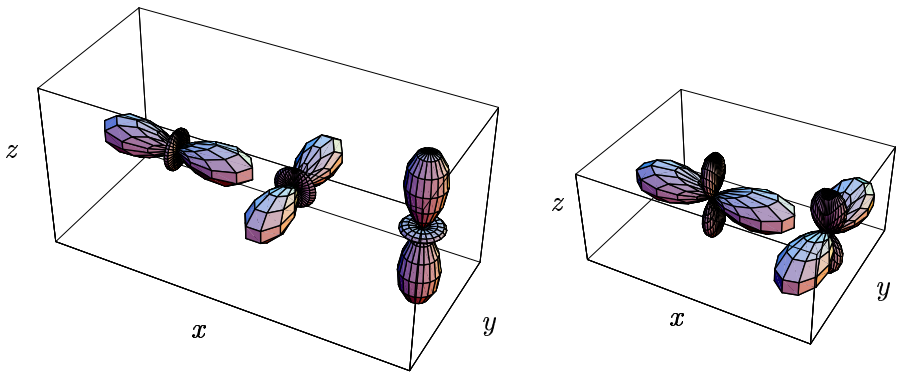

Figure 2.4: *The over-complete e_g-orbitals (left hand side, from left to right: ψ_x, ψ_y, ψ_z.) and an alternative basis (right hand side, from left to right: ψ_X, ψ_Y).*

However, the following basis can be used favorably in some special cases, e.g. for the description of phonons [12] (see Sec. 3.2):

$$\psi_X := \frac{1}{\sqrt{2}}(\psi_2 - \psi_3) \qquad = \qquad \frac{1}{\sqrt{6}}\left[(\sqrt{3}+1)\psi_x + (\sqrt{3}-1)\psi_y\right] \,, \tag{2.6a}$$

$$\psi_Y := -\frac{1}{\sqrt{2}}(\psi_2 + \psi_3) \qquad = \qquad \frac{1}{\sqrt{6}}\left[(\sqrt{3}-1)\psi_x + (\sqrt{3}+1)\psi_y\right] \,. \tag{2.6b}$$

This is an orthonormal basis. It is shown in the right hand side of Fig. 2.4.

Switching between the different bases is mediated by

$$\begin{pmatrix}\psi_X\\ \psi_Y\end{pmatrix} = \frac{1}{\sqrt{6}}\begin{pmatrix}\sqrt{3}+1 & \sqrt{3}-1\\ \sqrt{3}-1 & \sqrt{3}+1\end{pmatrix}\begin{pmatrix}\psi_x\\ \psi_y\end{pmatrix}\ , \tag{2.7a}$$

$$\begin{pmatrix}\psi_x\\ \psi_y\end{pmatrix} = \frac{1}{\sqrt{6}}\begin{pmatrix}\sqrt{3}+1 & 1-\sqrt{3}\\ 1-\sqrt{3} & \sqrt{3}+1\end{pmatrix}\begin{pmatrix}\psi_X\\ \psi_Y\end{pmatrix}\ , \tag{2.7b}$$

$$\begin{pmatrix}\psi_X\\ \psi_Y\end{pmatrix} = \frac{1}{\sqrt{2}}\begin{pmatrix}1 & -1\\ -1 & -1\end{pmatrix}\begin{pmatrix}\psi_2\\ \psi_3\end{pmatrix}\ , \tag{2.7c}$$

$$\begin{pmatrix}\psi_2\\ \psi_3\end{pmatrix} = \frac{1}{\sqrt{2}}\begin{pmatrix}1 & -1\\ -1 & -1\end{pmatrix}\begin{pmatrix}\psi_X\\ \psi_Y\end{pmatrix}\ . \tag{2.7d}$$

The relation between the different basis systems of the e_g-orbitals is viewed in Fig. 2.5. The angle between the different states of the over-complete basis from

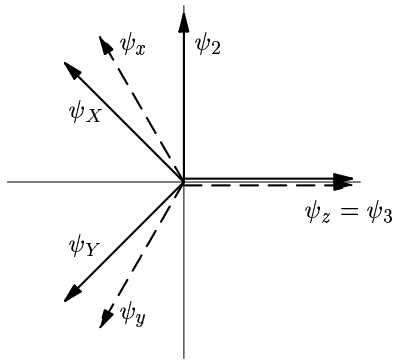

Figure 2.5: *The two-dimensional space of e_g-orbitals, with vertical and horizontal axes being the usual orthogonal basis functions ψ_2 and ψ_3. Both, the symmetrical over-complete basis functions ψ_x, ψ_y, and ψ_z, Eq. (2.5) (dashed lines), and the symmetrical orthogonal basis ψ_X and ψ_Y, Eq. (2.6) lie in the second and third quadrant.*

Eq. (2.5) is $2\pi/3$. The states ψ_x (ψ_y) and ψ_X (ψ_Y) point almost in the same direction, implying that they look similar in a graphical representation.

The Electronic Structure

The electronic structure of the compound can be briefly pictured as follows. The La^{3+} (Sr^{2+}) has the same electronic configuration as xenon (krypton), and therefore it is electronically inactive. Mn^{3+} (Mn^{4+}) has four (three) electrons in $3d$-states, the other electrons are in closed shells (argon configuration). The electrons of O^{2-} are in neon configuration.

First we discuss the electronic structure of $LaMnO_3$. The d-orbitals of the manganese ions are bridged by p-states of the oxygen ions (see Fig. 2.1). The

p_σ- or p_π-orbitals hybridize with the respective d-orbitals of either e_g- or t_{2g}-symmetry. Exactly these orbitals are occupied, which have the smallest overlap with the neighboring orbitals. Comparing t_{2g}- and e_g-states in Fig. 2.3 and bearing in mind that the three p-orbitals are directed along the x, y, and z axis respectively, one concludes that each t_{2g}-state is occupied, in particular the degeneracy between the t_{2g}- and e_g-states is lifted. This mechanism is called *crystal-field splitting*. The remaining d-electron occupies an e_g-orbital. Thus a model Hamiltonian should deal at least with e_g-orbitals of manganese and the bridging p_σ-orbitals of oxygen.

The physical properties of these *charge transfer models* are mainly determined by the ratio of two parameters. The on-site Coulomb interaction U has to be compared to the splitting of the $3d$- and the $2p$-states. The latter energy is called the charge-transfer energy $\Delta = |\varepsilon_p - \varepsilon_d|$, where ε_p and ε_d are the energies of a particle in these states, respectively. If $U < \Delta$ these systems are *Mott-Hubbard insulators*, in the opposite case they are called *charge-transfer insulators* [15]. In the former case holes are sited on manganese ions, in the latter case the holes have predominantly $2p$-character. The question which mechanism applies is not completely answered so far, although it is widely believed that doped holes in $LaMnO_3$ have mainly e_g-symmetry [11, 16].

This allows to further simplify the model Hamiltonian to one dealing only with e_g-degrees of freedom and localized corespins, which are formed by the t_{2g}-electrons of the manganese ions. These electrons are aligned in parallel because of the large Hund's rule coupling J_H (see Sec. 2.2.1), and thus forming a $S = 3/2$ spin. The e_g-electrons can hop from one manganese ion to the next by means of the *double exchange mechanism* [17] involving the oxygen ion in-between. The next section gives some details in how to derive the main contributions to the Hamiltonian.

2.2 Hamiltonians

The next subsections present a derivation of the contributions to an effective model Hamiltonian for the description of LSMO.

2.2.1 The Coulomb Interactions

The on-site Coulomb interactions of d-electrons at site i are generally given by [1, 18, 19]

$$\hat{\mathbf{H}}_{\mathrm{int},i} = \frac{1}{2} \sum_{\substack{\alpha_1,\alpha_2 \\ \alpha_1',\alpha_2'}} \sum_{\sigma_1,\sigma_2} I_{\alpha_1\alpha_2;\,\alpha_1'\alpha_2'}\; c^\dagger_{i\alpha_1\sigma_1}\, c^\dagger_{i\alpha_2\sigma_2} c_{i\alpha_2'\sigma_2}\, c_{i\alpha_1'\sigma_1} \;,$$

with the Coulomb matrix element

$$I_{\alpha_1\alpha_2;\,\alpha_1'\alpha_2'} = \iint d\mathbf{r}\, d\mathbf{r}'\, \phi^*_{\alpha_1}(\mathbf{r})\, \phi^*_{\alpha_2}(\mathbf{r}')\, g_{\mathbf{r}-\mathbf{r}'}\, \phi_{\alpha_1'}(\mathbf{r})\, \phi_{\alpha_2'}(\mathbf{r}') \;. \tag{2.8}$$

Here $g_{\mathbf{r}-\mathbf{r}'}$ is the screened Coulomb potential, and $\phi_\alpha(\mathbf{r})$ is the Wannier function for a d-electron in the α orbital at position $\mathbf{r}$. There are only a few different matrix elements, the so-called *Kanamori parameters* [20]. The intraband Coulomb interaction U, the interband Coulomb interaction U', the interband exchange interaction J, and the pair-hopping amplitude between different orbitals J' are shown in Tab. 2.1.

Table 2.1: Nonzero Coulomb matrix elements.

parameter	conditions	value
U	$\alpha_1 = \alpha_2 = \alpha_1' = \alpha_2',\ \sigma_1 \neq \sigma_2$	$I_{\alpha_1\alpha_1;\alpha_1\alpha_1}$
U'	$\alpha_1 = \alpha_1' \neq \alpha_2 = \alpha_2'$	$I_{\alpha_1\alpha_2;\alpha_1\alpha_2}$
J	$\alpha_1 = \alpha_2' \neq \alpha_2 = \alpha_1'$	$I_{\alpha_1\alpha_2;\alpha_2\alpha_1}$
J'	$\alpha_1 = \alpha_2 \neq \alpha_1' = \alpha_2',\ \sigma_1 \neq \sigma_2$	$I_{\alpha_1\alpha_2;\alpha_1'\alpha_1'}$

Analyzing Eq. (2.8) it can be shown that $J = J'$. Furthermore, for interactions between d-orbitals the relation

$$U = U' + J + J' = U' + 2J \tag{2.9}$$

holds. These relations can be shown using group theory [21].

Using the above parameters it is convenient to rewrite the Coulomb interaction in the following form:

$$\begin{aligned}\hat{\mathbf{H}}_{\mathrm{int},i} = &\frac{U}{2}\sum_{\alpha,\sigma} n_{i\alpha\sigma}\, n_{i\alpha\,-\sigma} + \frac{U'}{2}\sum_{\substack{\sigma,\sigma'\\ \alpha\neq\alpha'}} n_{i\alpha\sigma}\, n_{i\alpha'\sigma'} \\ &+ \frac{J}{2}\sum_{\substack{\sigma,\sigma'\\ \alpha\neq\alpha'}} c^\dagger_{i\alpha\sigma}\, c^\dagger_{i\alpha'\sigma'} c_{i\alpha\sigma'}\, c_{i\alpha'\sigma} \\ &+ \frac{J'}{2}\sum_{\substack{\sigma\\ \alpha\neq\alpha'}} c^\dagger_{i\alpha\sigma}\, c^\dagger_{i\alpha\,-\sigma} c_{i\alpha'\,-\sigma}\, c_{i\alpha'\sigma}\,,\end{aligned} \tag{2.10}$$

with $n_{i\alpha\sigma} = c^\dagger_{i\alpha\sigma} c_{i\alpha\sigma}$. It is important to note that the values of U' and J ($J' = J$) depend on the combination of orbitals involved, whereas the value of U is independent [1, 21]. Within the t_{2g}-orbitals a unique set of U' and J exists. Another set of parameters holds within the e_g-orbitals. Interactions between t_{2g}- and e_g-orbitals have different values for U' and J.

The above relation Eq. (2.9) can also be shown in the simple case of two orbitals ($\{a, b\}$) and two particles placed at one single site. Moreover this system shows how the spins get aligned in the groundstate giving rise to the so-called *Hund's*

rule. We introduce the following basis

$$
\begin{aligned}
|1\rangle &:= c^\dagger_{a\uparrow} c^\dagger_{a\downarrow}|0\rangle & |4\rangle &:= c^\dagger_{a\downarrow} c^\dagger_{b\uparrow}|0\rangle \\
|2\rangle &:= c^\dagger_{a\uparrow} c^\dagger_{b\uparrow}|0\rangle & |5\rangle &:= c^\dagger_{a\downarrow} c^\dagger_{b\downarrow}|0\rangle \\
|3\rangle &:= c^\dagger_{a\uparrow} c^\dagger_{b\downarrow}|0\rangle & |6\rangle &:= c^\dagger_{b\uparrow} c^\dagger_{b\downarrow}|0\rangle \ .
\end{aligned}
$$

Then the Hamiltonian Eq. (2.10) is represented by the matrix

$$
\mathbf{H} = \begin{pmatrix}
U & 0 & 0 & 0 & 0 & J' \\
0 & U'-J & 0 & 0 & 0 & 0 \\
0 & 0 & U' & -J & 0 & 0 \\
0 & 0 & -J & U' & 0 & 0 \\
0 & 0 & 0 & 0 & U'-J & 0 \\
J' & 0 & 0 & 0 & 0 & U
\end{pmatrix} .
$$

Its eigenvalues and eigenstates are shown in Tab. 2.2. The eigenstates can

Table 2.2: Eigenvalues and eigenstates of the two orbital and two particle situation. Two of the orbital triplet states are no eigenvectors of the operator $\hat{\mathbf{T}}^z$ (denoted with NE).

eigenvector	eigenvalue	spin	S^z	orbital	T^z
$\|2\rangle$	$U'-J$	triplet	$+1$	singlet	0
$\|5\rangle$	$U'-J$		-1		
$\frac{1}{\sqrt{2}}(\|3\rangle + \|4\rangle)$	$U'-J$		0		
$\frac{1}{\sqrt{2}}(\|3\rangle - \|4\rangle)$	$U'+J$	singlet	0	triplet	0
$\frac{1}{\sqrt{2}}(\|1\rangle - \|6\rangle)$	$U-J'$				NE
$\frac{1}{\sqrt{2}}(\|1\rangle + \|6\rangle)$	$U+J'$				NE

be analyzed according to their spin and orbital properties. For this purpose, orbital operators

$$
\begin{aligned}
\hat{\mathbf{T}}^x_i &= \frac{1}{2}\sum_\sigma (c^\dagger_{ia\sigma}\ c^\dagger_{ib\sigma}) \begin{pmatrix} 0 & 1 \\ 1 & 0 \end{pmatrix} \begin{pmatrix} c_{ia\sigma} \\ c_{ib\sigma} \end{pmatrix} , \\
\hat{\mathbf{T}}^y_i &= \frac{1}{2}\sum_\sigma (c^\dagger_{ia\sigma}\ c^\dagger_{ib\sigma}) \begin{pmatrix} 0 & -i \\ i & 0 \end{pmatrix} \begin{pmatrix} c_{ia\sigma} \\ c_{ib\sigma} \end{pmatrix} , \\
\hat{\mathbf{T}}^z_i &= \frac{1}{2}\sum_\sigma (c^\dagger_{ia\sigma}\ c^\dagger_{ib\sigma}) \begin{pmatrix} 1 & 0 \\ 0 & -1 \end{pmatrix} \begin{pmatrix} c_{ia\sigma} \\ c_{ib\sigma} \end{pmatrix} , \\
\hat{\mathbf{T}}^2_i &= (\hat{\mathbf{T}}^x_i)^2 + (\hat{\mathbf{T}}^y_i)^2 + (\hat{\mathbf{T}}^z_i)^2
\end{aligned}
$$

can be introduced in analogy to the spin operators

$$\begin{aligned}
\hat{\mathbf{S}}_i^x &= \frac{1}{2}\sum_\alpha (c_{i\alpha\uparrow}^\dagger \; c_{i\alpha\downarrow}^\dagger) \begin{pmatrix} 0 & 1 \\ 1 & 0 \end{pmatrix} \begin{pmatrix} c_{i\alpha\uparrow} \\ c_{i\alpha\downarrow} \end{pmatrix} \; , \\
\hat{\mathbf{S}}_i^y &= \frac{1}{2}\sum_\alpha (c_{i\alpha\uparrow}^\dagger \; c_{i\alpha\downarrow}^\dagger) \begin{pmatrix} 0 & -i \\ i & 0 \end{pmatrix} \begin{pmatrix} c_{i\alpha\uparrow} \\ c_{i\alpha\downarrow} \end{pmatrix} \; , \\
\hat{\mathbf{S}}_i^z &= \frac{1}{2}\sum_\alpha (c_{i\alpha\uparrow}^\dagger \; c_{i\alpha\downarrow}^\dagger) \begin{pmatrix} 1 & 0 \\ 0 & -1 \end{pmatrix} \begin{pmatrix} c_{i\alpha\uparrow} \\ c_{i\alpha\downarrow} \end{pmatrix} \; , \\
\hat{\mathbf{S}}_i^2 &= (\hat{\mathbf{S}}_i^x)^2 + (\hat{\mathbf{S}}_i^y)^2 + (\hat{\mathbf{S}}_i^z)^2 \; .
\end{aligned}$$

By means of these operators orbital degrees of freedom can be classified using the spin language. Table 2.2 shows the result of such an analysis. The lowest eigenvalue $U' - J$ has degeneracy three. It corresponds to a spin-triplet orbital-singlet state. The next eigenvalue $U' + J$ is a spin-singlet state and part of the orbital-triplet with $T^z = 0$. The next two states with energies $U \pm J'$ are both spin-singlets and combinations of orbital-triplets ($T^z|1\rangle = +1\,|1\rangle$, $T^z|6\rangle = -1\,|6\rangle$). However, the state with the highest energy $U + J'$ is invariant under orbital rotations, whereas the other two orbital-triplet states are not. But they form a subspace which is invariant against orbital rotations. Thus by demanding $U'+J = U-J'$, or equivalently $U = U'+J+J' = U'+2J$, the orbital symmetry can be restored. This is exactly the relation cited in Eq. (2.9).

For the case of three orbitals a similar study can be carried out. Again one finds the condition Eq. (2.9) to achieve orbital invariance.

In the case of a Mn^{4+} ion the three electrons are in the t_{2g}-states because of the *crystal-field splitting* (last paragraph of Sec. 2.1.1). The largest energy scale among the several Coulombic interactions is the intraband repulsion U. Thus no orbital is doubly occupied by both a spin-up and a spin-down electron and each of the three orbitals is occupied once. To take advantage of J, the spins of those three electrons point in the same direction (compare with the two orbital situation introduced above). This mechanism is called the *Hund's rule*.

Next we want to add an additional electron to deal with the Mn^{3+} ion. Two possibilities are accessible to the fourth electron depending on the ratio of the crystal-field splitting and the Coulomb interactions. In the case of manganites the so-called *high-spin state* is favored: an e_g-state is occupied with the spin parallel to the spins of the t_{2g}-orbitals. The second possibility, the *low-spin state* with all four electrons in t_{2g}-orbitals, lies energetically higher.

Model Hamiltonians for Coulomb Interactions

Now that we have analyzed the physical behavior due to Coulomb interactions in the case of manganites, we want to introduce a simplified model to deal with this situation. Of course this should be done without loss of the essential physics. It is reasonable to treat the three spin-polarized t_{2g}-electrons as a

localized corespin expressed by $\mathbf{S}_i$ at site i, since the overlap between the t_{2g}-orbitals and the occupied p-orbitals of the oxygen ions is small (as discussed in the last paragraph of Sec. 2.1.1). In this work another approximation is made, namely, instead of dealing with $S = 3/2$ (quantum-)corespins, we apply the classical limit $S \to \infty$. Thus at each site i there is a unit vector $\mathbf{S}_i$, which can be parameterized by a polar angle θ_i and an azimuthal angle ϕ_i

$$\mathbf{S}_i = (\sin\theta_i \cos\phi_i, \sin\theta_i \sin\phi_i, \cos\theta_i) \; .$$

The validity of this approximation with respect to manganites has been tested e.g. by Dagotto *et al.* [22].

The effect of the strong Hund's rule coupling is taken into account by introducing

$$\hat{\mathbf{H}}_{\mathrm{H}} = -J_H \sum_i \mathbf{S}_i \cdot \mathbf{S}_i^{e_g} = -J_H \sum_{\substack{i,\alpha \\ \sigma,\sigma'}} \mathbf{S}_i \cdot (c^\dagger_{i\alpha\sigma} \boldsymbol{\sigma}_{\sigma\sigma'} c_{i\alpha\sigma'}) \, , \tag{2.11}$$

where $\boldsymbol{\sigma}$ is the vector of Pauli matrices and $J_H > 0$ is the Hund coupling, which is of the order of J. The summation α goes only over the e_g-orbitals, which are quantized as in Eq. (2.4). The operators $c^\dagger_{i2\sigma}$ and $c^\dagger_{i3\sigma}$ create electrons in states ψ_2 and ψ_3 on site i with spin σ, respectively. The magnitudes of the spins are absorbed into J_H.

Even the remaining Coulomb Hamiltonian, which only concerns the e_g-electrons, will be treated approximatively with

$$\hat{\mathbf{H}}_{\text{el-el}} = U \sum_{i,\alpha} n_{i\alpha\uparrow} n_{i\alpha\downarrow} + U' \sum_i n_{i2} n_{i3} + V \sum_{<ij>} n_i n_j \, , \tag{2.12}$$

with $n_{i\alpha\sigma} = c^\dagger_{i\alpha\sigma} c_{i\alpha\sigma}$, $n_{i\sigma} = \sum_\alpha n_{i\alpha\sigma}$, $n_{i\alpha} = \sum_\sigma n_{i\alpha\sigma}$, and $n_i = \sum_{\alpha\sigma} n_{i\alpha\sigma}$. A nearest neighbor repulsion V has been introduced to account for long range Coulomb interactions. Note that we work in the quantization $\alpha = 2, 3$ (Eq. (2.4)).

2.2.2 The Kinetic Hamiltonian

A simple way to derive an expression for the kinetic part of e_g-electrons hopping to a nearest neighbor position is to use the over-complete basis (2.5). As can be seen in Fig. 2.4 ψ_x (ψ_y, ψ_z) points in the x-direction (y-, z-direction). Therefore if two neighboring orbitals in x-direction are of ψ_x type the hopping amplitude will be nonzero. A ψ_x electron can jump via a mediating p_σ-orbital of the oxygen ion to the ψ_x orbital of the neighboring manganese ion in x-direction. Contrary if only one of these two states is ψ_y or ψ_z the corresponding hopping amplitude will be negligible. The respective considerations about neighbors in $y-$ and $z-$direction hold. Thus the kinetic Hamiltonian reads

$$\hat{\mathbf{H}}_{\mathrm{t}} = t \sum_{\delta=x,y,z} \sum_{\substack{<ij>_\delta \\ \sigma}} c^\dagger_{i\delta\sigma} c_{j\delta\sigma} \; + \; H.c. \, , \tag{2.13}$$

where i numbers the manganese sites, $< ij >_\delta$, $\delta = x, y, z$, are nearest neighbors in δ direction. $c^\dagger_{ix\sigma}$, $c^\dagger_{iy\sigma}$, and $c^\dagger_{iz\sigma}$ are creation operators for the orbitals ψ_x, ψ_y, and ψ_z on site i with spin σ, respectively. Using Eq. (2.5), Eq. (2.13) can be re-expressed:

$$\hat{\mathbf{H}}_{\rm t} = t \sum_{\delta=x,y,z} \sum_{\substack{<ij>_\delta \\ \sigma}} \left(c^\dagger_{i2\sigma}\; c^\dagger_{i3\sigma} \right) T^{23}_\delta \begin{pmatrix} c_{j2\sigma} \\ c_{j3\sigma} \end{pmatrix} + H.c.\,, \tag{2.14}$$

with

$$T^{23}_x = \begin{pmatrix} \frac{3}{4} & -\frac{\sqrt{3}}{4} \\ -\frac{\sqrt{3}}{4} & \frac{1}{4} \end{pmatrix}, \quad T^{23}_y = \begin{pmatrix} \frac{3}{4} & \frac{\sqrt{3}}{4} \\ \frac{\sqrt{3}}{4} & \frac{1}{4} \end{pmatrix}, \quad T^{23}_z = \begin{pmatrix} 0 & 0 \\ 0 & 1 \end{pmatrix}. \tag{2.15}$$

The operators $c^\dagger_{i2\sigma}$ and $c^\dagger_{i3\sigma}$ create states ψ_2 and ψ_3 on site i with spin σ, respectively.

The representation in basis (2.6) can easily be calculated using Eq. (2.7b). This yields

$$\hat{\mathbf{H}}_{\rm t} = t \sum_{\delta=x,y,z} \sum_{\substack{<ij>_\delta \\ \sigma}} \left(c^\dagger_{iX\sigma}\; c^\dagger_{iY\sigma} \right) T^{XY}_\delta \begin{pmatrix} c_{jX\sigma} \\ c_{jY\sigma} \end{pmatrix} + H.c.\,, \tag{2.16}$$

with

$$T^{XY}_x = \begin{pmatrix} \frac{2+\sqrt{3}}{4} & -\frac{1}{4} \\ -\frac{1}{4} & \frac{2-\sqrt{3}}{4} \end{pmatrix}, \quad T^{XY}_y = \begin{pmatrix} \frac{2-\sqrt{3}}{4} & -\frac{1}{4} \\ -\frac{1}{4} & \frac{2+\sqrt{3}}{4} \end{pmatrix}, \quad T^{XY}_z = \begin{pmatrix} \frac{1}{2} & \frac{1}{2} \\ \frac{1}{2} & \frac{1}{2} \end{pmatrix}. \tag{2.17}$$

$c^\dagger_{iX\sigma}$ and $c^\dagger_{iY\sigma}$ create states ψ_X and ψ_Y on site i with spin σ, respectively.

2.2.3 The Phononic Hamiltonian

The only lattice degree of freedom that we consider is the oxygen motion along the direction of the bonds to the nearest two Mn ions, with a harmonic restoring force $-K\,u_\alpha$, where u_α, $\alpha = x, y, z$, is the displacement of O from its ideal position. The other degrees of freedom of vibrations of the octahedron do not couple to the e_g-electrons [23]. The variables $Q_\alpha(i) := u_\alpha(i + 1/2\;\hat{\alpha}) - u_\alpha(i - 1/2\;\hat{\alpha})$ measure the local displacement of oxygen along the α-axis around the i-th Mn ion ($\hat{\alpha}$ is the unit vector in α direction). Again the over-complete basis Eq. (2.5) is the starting point for the motivation of the model Hamiltonian. As the orbitals are extended merely along one specific axes the contribution to the Hamiltonian is diagonal. The expansion lowers the energy ϵ_α of orbital ψ_α by $\partial\epsilon_\alpha/\partial Q_\beta = -4g/\sqrt{3}\,\delta_{\alpha\beta}$. Thus the Hamiltonian reads

$$\hat{\mathbf{H}}_{\rm ep} = -\frac{4g}{\sqrt{3}} \sum_{\substack{\delta=x,y,z \\ i,\sigma}} c^\dagger_{i\delta\sigma} c_{i\delta\sigma} Q_\delta(i)\,. \tag{2.18}$$

The elastic energy operator reads

$$\hat{\mathbf{H}}_{\rm L} = \frac{K}{2} \sum_i \left[u^2_x(i + 1/2\;\hat{x}) + u^2_y(i + 1/2\;\hat{y}) + u^2_z(i + 1/2\;\hat{z}) \right], \tag{2.19}$$

whereas the kinetic contribution is

$$\hat{\mathbf{H}}_{\mathrm{pk}} = \frac{1}{2M} \sum_i \left[p_x^2(i + 1/2\ \hat{x}) \ + \ p_y^2(i + 1/2\ \hat{y}) \ + \ p_z^2(i + 1/2\ \hat{z}) \right] , \tag{2.20}$$

where M is the mass of the oxygen ions and p_α are the momenta corresponding to the different directions $\alpha = x, y, z$. Note that we will treat Q_α, u_α, and p_α, with $\alpha = x, y, z$, classically.

It is convenient to express the operator $\hat{\mathbf{H}}_{\mathrm{ep}}$ in a basis that is not over-complete. Using Eq. (2.5) one can rewrite Eq. (2.18), yielding two different parts, $\hat{\mathbf{H}}_{\mathrm{ep}} = \hat{\mathbf{H}}_{\mathrm{JT}} + \hat{\mathbf{H}}_{\mathrm{br}}$:

$$\hat{\mathbf{H}}_{\mathrm{JT}} = \sqrt{2}\, g \sum_{i,\sigma} \begin{pmatrix} c^\dagger_{i2\sigma} & c^\dagger_{i3\sigma} \end{pmatrix} \begin{pmatrix} Q_3(i) & Q_2(i) \\ Q_2(i) & -Q_3(i) \end{pmatrix} \begin{pmatrix} c_{i2\sigma} \\ c_{i3\sigma} \end{pmatrix} , \tag{2.21}$$

$$\hat{\mathbf{H}}_{\mathrm{br}} = -2\,(1+\beta)\, g \sum_{i,\sigma} Q_1(i) \ \left[c^\dagger_{i2\sigma} c_{i2\sigma} \ + \ c^\dagger_{i3\sigma} c_{i3\sigma} \right] , \tag{2.22}$$

with

$$Q_1(i) := \frac{1}{\sqrt{3}} \left(Q_x(i) + Q_y(i) + Q_z(i) \right) \tag{2.23a}$$

$$Q_2(i) := \frac{1}{\sqrt{2}} \left(Q_x(i) - Q_y(i) \right) \tag{2.23b}$$

$$Q_3(i) := \frac{1}{\sqrt{6}} \left(2Q_z(i) - Q_x(i) - Q_y(i) \right) . \tag{2.23c}$$

$\hat{\mathbf{H}}_{\mathrm{br}}$ with Q_1 describe the so-called breathing mode and $\hat{\mathbf{H}}_{\mathrm{JT}}$ with Q_2 and Q_3 describe the Jahn-Teller modes (see Fig. 2.6). A non-zero β was introduced by

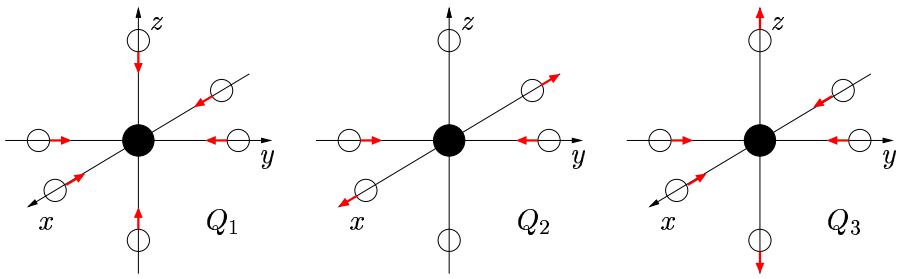

Figure 2.6: *Different local modes for a MnO_6 octahedron: (left) breathing mode, (middle) Jahn-Teller mode active in xy-planes, and (right) Jahn-Teller tetragonal distortion. Filled and empty circles show Mn and O ions, respectively.*

Millis, to represent additional charge coupling to the breathing mode.

Using Eq. (2.7d) one can re-write the Hamiltonians (2.21) and (2.22), yielding

$$\hat{\mathbf{H}}_{\mathrm{JT}} = -\sqrt{2}\, g \sum_{i,\sigma} \begin{pmatrix} c^\dagger_{iX\sigma} & c^\dagger_{iY\sigma} \end{pmatrix} \begin{pmatrix} Q_2(i) & Q_3(i) \\ Q_3(i) & -Q_2(i) \end{pmatrix} \begin{pmatrix} c_{iX\sigma} \\ c_{iY\sigma} \end{pmatrix} , \tag{2.24}$$

$$\hat{\mathbf{H}}_{\mathrm{br}} = -2\,(1+\beta)\, g \sum_{i,\sigma} Q_1(i) \ \left[c^\dagger_{iX\sigma} c_{iX\sigma} \ + \ c^\dagger_{iY\sigma} c_{iY\sigma} \right] . \tag{2.25}$$

2.2.4 The Hamiltonians Involving Spins

In section 2.2.1 we have seen that each of the three degenerate t_{2g}-orbital is occupied by one electron. Their spins are in parallel alignment at each site due to Hund's rule, forming the corespin of $S = 3/2$ on each manganese site. The spin of an e_g-electron again favors parallel alignment with respect to the local corespin because of the large Hund's rule coupling J_H. This situation has been modeled by the Hamiltonian Eq. (2.11)

$$\hat{\mathbf{H}}_{\mathrm{H}} = -J_H \sum_{\substack{i,\alpha \\ \sigma,\sigma'}} \mathbf{S}_i \cdot (c^\dagger_{i\alpha\sigma} \boldsymbol{\sigma}_{\sigma\sigma'} c_{i\alpha\sigma'}) \,. \tag{2.26}$$

Measurements reveal a tendency to anti-ferromagnetic (AF) order if the e_g-band filling is near $n \approx 0$ or near $n \approx 1$. This phenomenon can be attributed to a weak superexchange mechanism ([17]) involving the p-electrons of the interstitial oxygen ions. The respective Hamiltonian reads

$$\hat{\mathbf{H}}_{\mathrm{AF}} = J' \sum_{<ij>} \mathbf{S}_i \cdot \mathbf{S}_j \,, \tag{2.27}$$

where J' is the weak AF coupling constant. (From now on, J' denotes the AF coupling constant which must not be mixed up with the pair-hopping amplitude between different orbitals introduced in Sec. 2.2.1.)

These representations are valid for both quantizations $\alpha = 2, 3$ (Eq. (2.4)) and $\alpha = X, Y$ (Eq. (2.6)).

2.2.5 The Model Hamiltonians

Collecting all the terms of the previous subsections a rather complicated Hamiltonian comes into existence:

$$\hat{\mathbf{H}} = \hat{\mathbf{H}}_{\mathrm{t}} + \hat{\mathbf{H}}_{\mathrm{ep}} + \hat{\mathbf{H}}_{\mathrm{L}} + \hat{\mathbf{H}}_{\mathrm{pk}} + \hat{\mathbf{H}}_{\mathrm{JT}} + \hat{\mathbf{H}}_{\mathrm{br}} + \hat{\mathbf{H}}_{\mathrm{H}} + \hat{\mathbf{H}}_{\mathrm{AF}} + \hat{\mathbf{H}}_{\text{el-el}} \,.$$

Of course it is beyond todays analytic and numerical techniques to rigorously analyze such a Hamiltonian. Therefore, further simplifications must be carried out. Some possible model Hamiltonians are described in what follows.

Ferromagnetic Kondo Model

Neglecting phonon contributions and Coulomb correlations one ends up with

$$\hat{\mathbf{H}} = \hat{\mathbf{H}}_{\mathrm{t}} + \hat{\mathbf{H}}_{\mathrm{H}} + \hat{\mathbf{H}}_{\mathrm{AF}} \,.$$

A further simplification is to neglect the orbital degrees of freedom, leading to a model commonly referred to as *ferromagnetic Kondo model*

$$\hat{\mathbf{H}}_{\mathrm{Kondo}} = t \sum_{\delta=x,y,z} \sum_{\substack{<ij>_\delta \\ \sigma}} c^\dagger_{i\sigma} c_{j\sigma} \; - J_H \sum_{\substack{i \\ \sigma,\sigma'}} \mathbf{S}_i \cdot (c^\dagger_{i\sigma} \boldsymbol{\sigma}_{\sigma\sigma'} c_{i\sigma'}) \; + J' \sum_{<ij>} \mathbf{S}_i \cdot \mathbf{S}_j \,.$$

However, this name is used ambiguously in literature. Sometimes the multi-orbital case is called equally, sometimes it is called *multi-orbital ferromagnetic Kondo model*.

The advantage of this model is that given a fixed corespin configuration the remaining Hamiltonian represents a one-electron problem. This can clearly be exploited in both analytic and numeric approaches.

The $J_H \to \infty$ Limit and the Double Exchange Model

The Hund's rule coupling J_H is the dominant energy scale in manganites. Thus it is evident to take the $J_H \to \infty$ limit. In order to carry out this calculation it is favorable to rewrite the Hamiltonians containing e_g-electrons. These electrons are expressed in an alternative basis concerning their spin. Instead of using the same global quantization direction for all e_g-states a locally varying one is used. The quantization direction of our choice is the one given by the direction of the (classically treated) t_{2g} corespins. The detailed calculations are carried out in Sec. 5.2. As one expects the down-spin configurations are punished by the large Hund's rule coupling and in the $J_H \to \infty$ limit these configurations are forbidden. Thus only contributions of the up-spin channel remain and the Hund's coupling term $\hat{\mathbf{H}}_{\mathrm{H}}$ becomes a constant which can be omitted. The price to be paid is a kinetic energy term which is more complicated, particularly the hopping amplitudes depend on the orientations of the local corespins

$$\hat{\mathbf{H}}_{\mathrm{t}}^{\infty} = t \sum_{\delta=x,y,z} \sum_{<ij>_\delta} U_{ij} \left(c_{i2}^{\dagger} \; c_{i3}^{\dagger} \right) T_{\delta}^{23} \begin{pmatrix} c_{j2} \\ c_{j3} \end{pmatrix} + H.c.$$

or

$$\hat{\mathbf{H}}_{\mathrm{t}}^{\infty} = t \sum_{\delta=x,y,z} \sum_{<ij>_\delta} U_{ij} \left(c_{iX}^{\dagger} \; c_{iY}^{\dagger} \right) T_{\delta}^{XY} \begin{pmatrix} c_{jX} \\ c_{jY} \end{pmatrix} + H.c. \,,$$

with

$$\begin{aligned} U_{ij} &= \cos(\theta_i/2) \; \cos(\theta_j/2) + \sin(\theta_i/2) \; \sin(\theta_j/2) \; \mathrm{e}^{-i(\phi_i - \phi_j)} \\ &= \cos(\vartheta_{ij}/2) \; \mathrm{e}^{i\psi_{ij}} \,, \end{aligned}$$

where θ_i is the polar angle of the corespin on site i and ϕ_i is its azimuthal angle. ϑ_{ij} is the relative angle between the corespins at site i and j, and ψ_{ij} is some phase factor. Spin subscripts are omitted because only spin-up electrons contribute.

Using this approximation for the FM Kondo model yields the *double exchange* (DE) *model*. From the last equation one sees that perfect FM order of the corespins leads to a maximal hopping parameter, wheras perfect AF order makes the hopping of the e_g-electrons impossible.

Chapter 3

The Basic Physics of Manganites

In the last chapter we discussed both the lattice and the electronic structure of LSMO. Based on these observations we were able to introduce several contributions to a model Hamiltonian for this compound. We have seen that many different degrees of freedom contribute to the model Hamiltonian, such as spin, orbital, and phononic degrees. The interplay between these contributions gives rise to a great variety of physical effects and to a rich phase diagram. In this chapter some of the basic physical properties of manganites are discussed.

3.1 Magnetic Order

By means of the DE model the competing mechanisms concerning magnetic order can be shown. Additional large Coulomb interactions U and U' must be invoked to forbid double-occupancy of e_g-orbitals. The relevant doping range is from e_g-electron density $n = 0$ (corresponding to $x = 1$ in $La_{1-x}Sr_xMnO_3$) to a density $n = 1$ ($x = 0$, L e_g-electrons on L sites, half-filling). At both limits, $n \approx 0$ and $n \approx 1$, the charge carrier density is low due to the lacking double-occupancy. In the former case the carriers are e_g-electrons, in the latter case they are e_g-holes.

In order to minimize the kinetic energy the hopping parameter should be as large as possible. Thus in e_g-electron densities allowing for great carrier mobility, *i.e.* around quarter-filling ($L/2$ electrons on L sites, $n = 0.5$), the kinetic energy drives a strong FM force. In the case of small AF superexchange coupling J', which is true for manganites, FM order is thus established.

At the doping limits ($n \approx 0$ and $n \approx 1$) the carrier density is to small to overcome the AF coupling. Furthermore in the $n \approx 1$ region additional AF forces of the order $t^2/(2J_H)$ come into existence in the case of the FM Kondo model. They derive from virtual excitations (see Sec. 5.3) and are proportional to the electron density n in the simplest case.

Summarizing the above arguments one can qualitatively understand some of the aspects of the phase diagrams of manganites (see Fig. 1.1). Starting from $x = 0$ ($n = 1$) one observes AF order developing to FM order around quarter-filling. Often the transition between AF and FM order is not abrupt but mediated by spin-canted states or by so-called C-AF and A-AF order. C-AF order means antiferromagnetically ordered planes with feromagnetically ordered chains perpendicular to the planes, whereas A-AF means feromagnetically ordered planes with antiferromagnetically ordered chains. The totally ordered antiferromagnet is called G-AF in this nomenclature.

3.2 Jahn-Teller Effect

At the end of Sec. 2.1.1 we have argued that due to the crystal field splitting the degeneracy of the d-electrons is partly lifted. The t_{2g}-orbitals are occupied, additional electrons go into the energetically higher e_g-states. The remaining degeneracy of the e_g-states is lifted by phononic interactions. This mechanism is called *Jahn-Teller effect*. Considering a single octahedron with only static phononic interactions (adiabatic approximation) this effect can easily be demonstrated [24].

We restrict Eqs. (2.19, 2.21, 2.22) to one octahedron, yielding

$$\hat{\mathbf{H}} = \hat{\mathbf{H}}_{\mathrm{L}} + \hat{\mathbf{H}}_{\mathrm{JT}} + \hat{\mathbf{H}}_{\mathrm{br}}$$

with

$$\begin{aligned}
\hat{\mathbf{H}}_{\mathrm{L}} &= \frac{K}{2}\left[u_x^2(-1/2\,\hat{x}) + u_x^2(+1/2\,\hat{x}) + u_y^2(-1/2\,\hat{y})\right. \\
&\qquad \left. + u_y^2(+1/2\,\hat{y}) + u_z^2(-1/2\,\hat{z}) + u_z^2(+1/2\,\hat{z})\right], \\
\hat{\mathbf{H}}_{\mathrm{JT}} &= \sqrt{2}\,g \begin{pmatrix} c_2^\dagger & c_3^\dagger \end{pmatrix} \begin{pmatrix} Q_3 & Q_2 \\ Q_2 & -Q_3 \end{pmatrix} \begin{pmatrix} c_2 \\ c_3 \end{pmatrix}, \\
\hat{\mathbf{H}}_{\mathrm{br}} &= -2\,g\,Q_1 \left[c_2^\dagger c_2 + c_3^\dagger c_3\right].
\end{aligned}$$

Spin degrees of freedom have been omitted because the Hamiltonian does not distinguish between different spins and we only want to explore the difference between Mn^{4+} (no e_g-electron) and Mn^{3+} (one e_g-electron). Without an electron in the e_g-orbitals only the elastic energy $\hat{\mathbf{H}}_{\mathrm{L}}$ contributes. Minimization of the energy yields $E = 0$ for the groundstate (with $Q_1 = Q_2 = Q_3 = 0$). Note that we treat the phonons classically.

Adding one electron the Jahn-Teller interaction $\hat{\mathbf{H}}_{\mathrm{JT}}$ is the only term which is not diagonal. It can be diagonalized easily by introducing polar coordinates $(Q_2, Q_3) = Q\,(\sin\phi, \cos\phi)$:

$$\begin{aligned}
\hat{\mathbf{H}}_{\mathrm{JT}} &= \sqrt{2}\,g\,Q \begin{pmatrix} \alpha^\dagger & \beta^\dagger \end{pmatrix} \begin{pmatrix} -1 & 0 \\ 0 & 1 \end{pmatrix} \begin{pmatrix} \alpha \\ \beta \end{pmatrix} \\
&= \sqrt{2}\,g\,Q\,(\hat{\mathbf{n}}_\beta - \hat{\mathbf{n}}_\alpha),
\end{aligned}$$

where

$$\begin{pmatrix}\alpha\\ \beta\end{pmatrix} = \begin{pmatrix}-\sin\frac{\phi}{2} & \cos\frac{\phi}{2}\\ \cos\frac{\phi}{2} & \sin\frac{\phi}{2}\end{pmatrix}\begin{pmatrix}c_2\\ c_3\end{pmatrix}. \tag{3.1}$$

The breathing mode couples to the total particle number. Thus it is not affected by the above transformation.

Next the elastic energy has to be expressed through the normal modes Q_1, Q_2, Q_3. From Eq. (2.23) one can calculate

$$\begin{pmatrix}Q_x\\ Q_y\\ Q_z\end{pmatrix} = \begin{pmatrix}\frac{1}{\sqrt{3}} & \frac{1}{\sqrt{2}} & -\frac{1}{\sqrt{6}}\\ \frac{1}{\sqrt{3}} & -\frac{1}{\sqrt{2}} & -\frac{1}{\sqrt{6}}\\ \frac{1}{\sqrt{3}} & 0 & \sqrt{\frac{2}{3}}\end{pmatrix}\begin{pmatrix}Q_1\\ Q_2\\ Q_3\end{pmatrix} \quad \text{and}$$

$$\begin{aligned} Q_x^2+Q_y^2+Q_z^2 &= \begin{pmatrix}Q_x & Q_y & Q_z\end{pmatrix}\begin{pmatrix}Q_x\\ Q_y\\ Q_z\end{pmatrix}\\ &= Q_1^2+Q_2^2+Q_3^2\,. \end{aligned}$$

Remember that $Q_\alpha := u_\alpha(+1/2\ \hat{\alpha}) - u_\alpha(-1/2\ \hat{\alpha})$ with $\alpha = x, y, z$. The elastic energy is quadratic in each u_α. Therefore the symmetric decomposition, $u_\alpha(+1/2\ \hat{\alpha}) = -u_\alpha(-1/2\ \hat{\alpha})$ has the lowest energy yielding $Q_\alpha = 2\,u_\alpha(+1/2\ \hat{\alpha})$. The elastic energy then reads

$$\begin{aligned} \hat{\mathbf{H}}_{\mathrm{L}} &= \frac{K}{4}\left[Q_1^2+Q_2^2+Q_3^2\right]\\ &= \frac{K}{4}\left[Q_1^2+Q^2\right]. \end{aligned}$$

All contributions to the Hamiltonian are now diagonal and the change in energy when adding one electron is $\Delta E = -2\,g\,Q_1 \pm \sqrt{2}\,g\,Q + K(Q_1^2+Q^2)/4$. Minimizing the energy with respect to the distortions Q_1 and Q yields a lowering of the groundstate by $\Delta E = -6\,g^2/K$ and optimal distortions $\tilde{Q}_1 = 4\,g/k$ and $\tilde{Q} = 2\sqrt{2}\,g/K$.

The energy lowering ΔE has been obtained without taking into account the vibrations of the oxygen ions. If the kinetic energy due to the vibrations is so large that its amplitude exceeds $\tilde{Q}$, then the problem has to be treated dynamically including the kinetic energy Eq. (2.20) of the anions.

The angle ϕ does not enter ΔE. This degeneracy is lifted either by adding kinetic energy and quantization of lattice degrees of freedom (dynamic Jahn-Teller effect), or else by introducing higher order anharmonic terms in the electron-phonon coupling [23].

When considering a whole lattice the distortions of the various octahedra must be mutually compatible giving rise to the so-called *cooperative Jahn-Teller effect*. In the case of $LaMnO_3$ (one e_g-electron per octahedron) the Q_2-modes are energetically favored below a transition temperature $T_{\mathrm{JT}} \simeq 750$ K [25]. This

leads to a angle $\phi = \pi/2$ in the above calculation. Inserting ϕ into Eq. (3.1) yields the corresponding eigenstates

$$|\psi_a\rangle = a^\dagger|0\rangle = 1/\sqrt{2}\,(-c_2^\dagger + c_3^\dagger)|0\rangle = -|\psi_X\rangle \text{ and}$$
$$|\psi_b\rangle = b^\dagger|0\rangle = 1/\sqrt{2}\,(c_2^\dagger + c_3^\dagger)|0\rangle \quad = -|\psi_Y\rangle\ ,$$

which have been introduced in Eq. (2.6). Figure 3.1 shows the orbital ordering

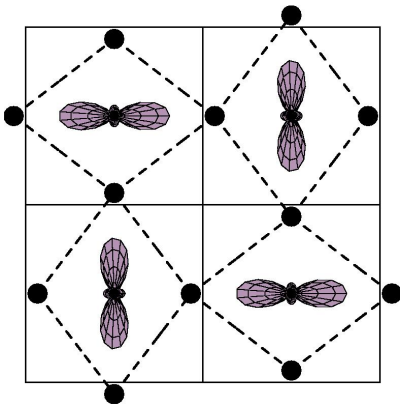

Figure 3.1: *Jahn-Teller distorted $LaMnO_3$ (x-y plane). Only the main distortions of Q_2-type are considered. Black disks symbolize the oxygen anions, the orbitals are ψ_X and ψ_Y as introduced in Sec. 2.1.1.*

of $LaMnO_3$.

When a hole is added, the distortions Q_l, $l = 1, 2, 3$, are locally readjusted and a bound state is formed [12]. The Q_2 distortion is locally softened. Therefore Allen called this state *anti-Jahn-Teller polaron*.

The Jahn-Teller distortion in $LaMnO_3$ is quite large. The octahedral aspect ratio is about 1.12 (see [16] and references therein). In a doped system like $La_{0.7}Sr_{0.3}MnO_3$ the crystal structure is much more nearly cubic. The slight distortion seems to be predominantly due to octahedral rotation. The impact of rotations and tilting of the octahedra is discussed in the next section.

The results of the calculations above show the importance of phononic effects in the multi-orbital case.

3.3 Influence of the Bandwidth

An important parameter in manganites is the Mn-O-Mn bond angle [16, 1]. Due to distortions of the octahedra, especially tilting and rotation, this angle is less than 180°. At 180° the hybridization between the d-orbitals and the oxygen p-orbitals is maximal, whereas an angle of 90° prohibits hopping of electrons via oxygen. Thus the hopping parameter of e_g-electrons and the bandwidth is

a function of the Mn-O-Mn bond angle. The bandwidth, in turn, determines or at least influences the Curie temperature (see Sec. 6.5 particularly Fig. 6.9).

In a $A_{1-x}A'_xMnO_3$ system with a fixed number of electrons $n = 1 - x$ in the e_g conduction band, the bond angle can either be altered by varying the average ionic radius of A or A′ ions, *i.e.* by internal pressure, or by applying external pressure (see Figure 3.2).

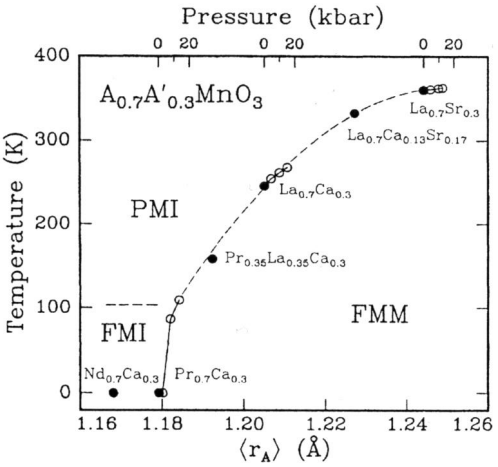

Figure 3.2: *Phase diagram of $A_{0.7}A'_{0.3}MnO_3$ as a function of the hopping parameter, which has been varied both by internal and external pressure. Full circles represent variations due to internal pressure (variations of the average A-site ionic radius $\langle r_A \rangle$), and open circles indicate variations due to externally applied pressure. From [26].*

The effect of the bandwidth on the transport properties is even more striking. In LSMO with $x \approx 0.3$ the resistivity above T_C (≈ 370 K) continues to rise, whereas in $La_{1-x}Ca_xMnO_3$ (LCMO) with $x \approx 0.3$ the resistivity peaks at T_C (≈ 260 K) and decreases as the temperature is raised above T_C. Furthermore the resistivity of LCMO is an order of magnitude higher than the resistivity of LSMO.

Additionally, the variance σ^2 of the ionic radius r_A plays an important role. Rodrigues-Martinez and Attfield [27] found that T_C can be reduced by a large factor if σ^2 is modified, keeping $\langle r_A \rangle$ constant. They observed that maximum MR effects are found in materials not only with a low value of $\langle r_A \rangle$ but also a small value of σ^2. A good example is $Pr_{1-x}Ca_xMnO_3$ since Pr^{3+} and Ca^{2+} ions are similar of size.

3.4 Explanation of the Colossal MR

MR effects are largest at carrier densities separating the metallic from the insulating phase (cp. with Chp. 1). Experimental data reveal tendencies to (nano-

scale) phase separation (PS) in this region. Dagotto and coworkers [1] report PS regimes in theoretical work, too. This interpretation of the theoretical data is criticized, however, *e.g.* by [16] and by us (Chp. 7, [10]).

Besides this electronically driven phase separation Moreo *et. al.* [28] proposed a different mechanism leading to PS. In the last paragraph of the previous section, the influence of the variance of the ionic radius has been discussed. Moreo modeled this situation by varying the hopping parameter t and the AF superexchange coupling J' randomly. The mean values of t and J' and the values of the remaining parameters were set to the border of the AF and FM regime. Monte Carlo simulations revealed a building up of FM and AF domains. The larger the variance of the randomly chosen parameters is, the smaller the individual clusters are. If the magnitude of MR effects are directly related to the size of the clusters, the behavior described by Rodrigues-Martinez and Attfield can be understood at least qualitatively.

Based on a PS scenario the MR effect can be modeled phenomenologically [29]. The randomly distributed domains are either metallic or insulating. Percolation occurs depending on the relative fraction p of metallic clusters. The phenomenological approach maps the real system onto a network of resistors giving rise to a so-called *random-resistor network*. Each unit (resistor) in the network corresponds either to a metallic or an insulating domain. The dependence of the resistivity on the temperature is given by $R_M(T)$ ($R_I(T)$) in the metallic (insulating) domain. In [29], these functions have been extracted from experiments.

The main features of this approach can be easily understood. If a metallic cluster percolates, the situation can be schematically visualized as in Fig. 3.3a. A crude model for this situation is a system of two resistors, which are connected in parallel (Fig. 3.3b) and where a peak in the effective resistance at intermediate T is natural.

The results of simulations of full random-resistor networks are shown in Fig. 3.3c. One observes a peak in the temperature dependence near the percolative transition. Small variations of p in this region ($p \in [0.4, 0.55]$) dramatically influences the behavior of the effective resistance, which is in qualitative agreement with some experiments (*e.g.* [30]).

The metallic (FM) regions grow when applying a magnetic field. In the same region $p \in [0.4, 0.55]$ this has a big influence on the effective resistivity, which in turn is the colossal MR effect.

Further improvements of this phenomenological models have been carried out in order to achieve quantitative agreement (*e.g.* [31, 32]).

Other Explanations of CMR

Some other mechanisms are discussed in literature to explain the colossal MR effect.

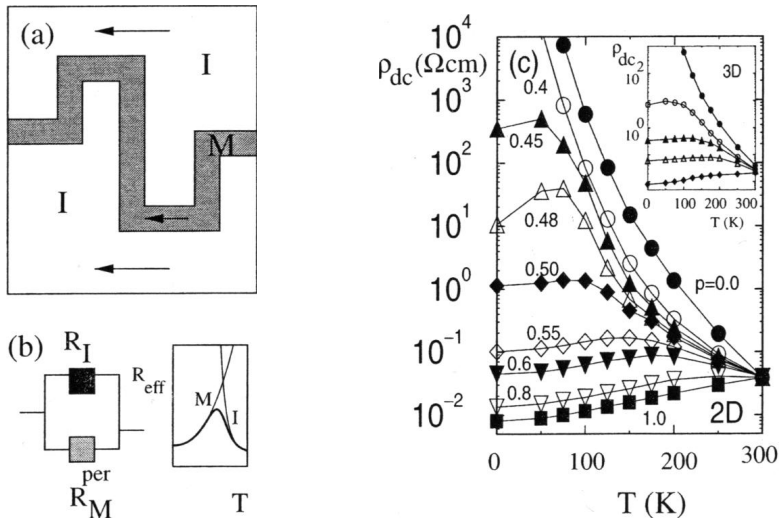

Figure 3.3: *(a) Mixed-phase state near percolation. Arrows indicate conduction through insulating or metallic regions depending on T. (b) Two-resistance model. Effective resistance R_{eff} vs T arising from the parallel connection of metallic R_M and insulating R_I resistances. (c) Net resistivity ρ_{dc} of a 100×100 cluster vs T, at the indicated metallic fractions p. Inset: Results from a 20^3 cluster with (from top) $p = 0.0$, 0.25, 0.30, 0.40, and 0.50. From [29].*

Sboychakov *et al.* [33] proposed a derivation of CMR starting from the following assumptions. PS corresponds to the emergence of small ferromagnetic metallic droplets (ferrons) in an insulating AF or paramagnetic medium, with the metallic phase fraction being far from the percolation threshold. In the limit of strong Coulomb interaction, each ferron contains one charge carrier located in the potential well of ferromagnetically ordered local spins (FM polaron). The charge transfer is accomplished by way of electron jumps between this droplets.

Edwards [16] and coworkers, however, neglect the percolative nature of CMR. He states that CMR can be reproduced within the *Holstein-DE model*, *i.e.* the DE model with additional quantum phonons (*Holstein model*). The crucial parameter is the ratio g/W between the electron-phonon coupling g and the bandwidth W. They showed that small variations of this parameter have tremendous impact on the resistivity as a function of temperature. This explains the differences of the resistivity behavior of *e.g.* LSMO and LCMO. Also the influence of the magnetic field can be described qualitatively.

Chapter 4

Autocorrelations in Markov Chain Monte Carlo

In our work we use Markov Chain Monte Carlo (MCMC) extensively to investigate the Kondo model. Integrals over the classical spins are carried out stochastically [1]. The random walk through the configuration space is thereby generated by a Markov process, *i.e.* based on the current configuration a new configuration is generated at random. Thus the sample of configurations is correlated. These correlations must be analyzed carefully in order to correctly estimate statistical errors. In the following, some key features of MCMC shall be discussed.

For simplicity we consider a discrete space $\mathbf{\Omega}$ of states $Z_i \in \mathbf{\Omega}$ with a probability distribution $\boldsymbol{\rho} : \mathbf{\Omega} \to [0,1]$, which we want to sample. A Markov Chain (MC) can be characterized by a Markov matrix $\mathbf{M}$. The value of the matrix element M_{ij} is the probability to move to state Z_i given state Z_j. Probability distributions $\mathbf{p} : \mathbf{\Omega} \to [0,1]$ can be written as vectors with elements p_i. A pure state Z_i corresponds to the distribution $\mathbf{p}^{(i)}$ and has elements $p_j^{(i)} = \delta_{ij}$.

Because the matrix elements are transition probabilities the matrix fulfills

$$M_{ij} \in [0,1] \qquad \text{for all } i,j \tag{4.1}$$

$$\sum_i M_{ij} = 1 \qquad \text{for all } j \tag{4.2}$$

and is called a *stochastic matrix*.

The matrix $\mathbf{M}$ is constructed such that $\boldsymbol{\rho}$ is the invariant distribution, *i.e.*

$$\mathbf{M}\,\boldsymbol{\rho} = \boldsymbol{\rho}\,, \tag{4.3}$$

which means that $\boldsymbol{\rho}$ is an eigenvector of $\mathbf{M}$ with eigenvalue $\lambda = 1$.

Some of the properties which are implied by these conditions are shown in the following section.

4.1 Properties of the Stochastic Matrix

A probability distribution $\mathbf{p}$ contains only nonnegative numbers and is normalized

$$\sum_i p_i = 1 \; .$$

Applying $\mathbf{M}$ on a probability distribution $\mathbf{p}$ yields another probability distribution $\mathbf{p}'$ because

$$\begin{aligned} p'_i &= \sum_j \underbrace{M_{ij}}_{\geq 0} \underbrace{p_j}_{\geq 0} \\ &\geq 0 \end{aligned}$$

and

$$\begin{aligned} \sum_i p'_i &= \sum_{i,j} M_{ij}\, p_j \\ &= \sum_j p_j \underbrace{\sum_i M_{ij}}_{=1} \\ &= \sum_j p_j \\ &= 1 \; . \end{aligned}$$

All eigenvalues λ_ν of $\mathbf{M}$ are elements of the unit circle in the complex plane

$$|\lambda_\nu| \leq 1 \; .$$

This can be shown using **Geršgorin's theorem** [34] and Eqs. (4.1,4.2):

Geršgorin's theorem. *Let* $\mathbf{A}$ *be a* $n \times n$*-matrix of complex numbers. Define the quantities*

$$R_j(A) := \sum_{\substack{i=1 \\ i \neq j}}^{n} |A_{ij}| \; .$$

Then all eigenvalues of $\mathbf{A}$ *are contained in the set*

$$\bigcup_{j=1}^{n} \{ z \in \mathbb{C} : |z - A_{jj}| \leq R_j(A) \} \; .$$

An additional condition, *ergodicity*, ensures that only one eigenvector with eigenvalue $|\lambda| = 1$ exists, namely $\boldsymbol{\rho}$. All other eigenvalues obey $|\lambda| < 1$.

Eigenvectors $\mathbf{x}_\nu$ and eigenvalues λ_ν are given by the equations

$$\mathbf{M}\, \mathbf{x}^{(\nu)} = \lambda_\nu\, \mathbf{x}^{(\nu)} \; . \tag{4.4}$$

We assume the geometric multiplicity to be equal to the algebraic multiplicity, *i.e.* if an eigenvalue λ is r-times degenerated, then r linearly independent eigenvectors with eigenvalue λ exist. The above equation can then be written in matrix form

$$\mathbf{M}\,\mathbf{V} = \mathbf{V}\,\mathbf{D}\,, \tag{4.5}$$

where the columns of $\mathbf{V}$ contain the eigenvectors and $\mathbf{D}$ is a diagonal matrix with the eigenvalues λ_ν on the diagonal. Furthermore the matrix $\mathbf{V}$ is nonsingular and can thus be inverted yielding

$$\mathbf{M} = \mathbf{V}\,\mathbf{D}\,\mathbf{V}^{-1} \tag{4.6}$$

$$\mathbf{D} = \mathbf{V}^{-1}\,\mathbf{M}\,\mathbf{V} \tag{4.7}$$

$$\mathbf{V}^{-1}\,\mathbf{M} = \mathbf{D}\,\mathbf{V}^{-1}\,. \tag{4.8}$$

The last equation means that the rows of $\mathbf{V}^{-1}$ are the left eigenvalues of $\mathbf{M}$. Equation (4.2) can be written in vector form using a vector $\mathbf{1}$ with elements $1_i = 1$

$$\mathbf{1}^{\mathrm{T}}\,\mathbf{M} = \mathbf{1}^{\mathrm{T}}\,,$$

i.e. $\mathbf{1}^{\mathrm{T}}$ is a left eigenvector with eigenvalue 1. We remember that $\boldsymbol{\rho}$ is a right eigenvector to the same eigenvalue (see Eq. (4.3)). In the following we identify λ_1 with 1, *i.e.* the first column V_{i1} of $\mathbf{V}$ contains $\boldsymbol{\rho}$ and the first row $(V^{-1})_{1i}$ of $\mathbf{V}^{-1}$ contains $\mathbf{1}^{\mathrm{T}}$. In order to be correct, we have to check if the normalization of the both eigenvectors is consistent. Therefore we consider the equation belonging to D_{11} of Eq. (4.7):

$$\begin{aligned} D_{11} &= \sum_{i,j} (V^{-1})_{1i}\, M_{ij}\, V_{j1} \\ 1 &= \sum_j \underbrace{\Big(\sum_i 1_i\, M_{ij}\Big)}_{=1}\, \rho_j \\ 1 &= 1 \end{aligned} \tag{4.9}$$

Another property follows from the eigenvalue equation (4.4) of stochastic matrices. Summing over the components of the vectors yields

$$\begin{aligned} \sum_{i,j} M_{ij}\, x_j^{(\nu)} &= \lambda_\nu \sum_i x_i^{(\nu)} \\ \sum_j x_j^{(\nu)} \underbrace{\sum_i M_{ij}}_{=1} &= \lambda_\nu \sum_i x_i^{(\nu)} \\ (1-\lambda_\nu) \sum_i x_i^{(\nu)} &= 0\,, \end{aligned}$$

from which follows that except $\boldsymbol{\rho}$ all other eigenvectors have the property

$$\sum_i x_i^{(\nu)} = 0 \qquad \text{for all } \nu > 1\,.$$

Using Eq. (4.6) powers of $\mathbf{M}$ can easily be evaluated

$$\begin{aligned}\mathbf{M}^n &= (\mathbf{V}\,\mathbf{D}\,\mathbf{V}^{-1})^n \\ &= \mathbf{V}\,\mathbf{D}^n\,\mathbf{V}^{-1}\,. \end{aligned} \tag{4.10}$$

The limit $\lim_{n\to\infty}(D^n)_{ij} = \delta_{i1}\,\delta_{1j}$ implies

$$\begin{aligned}\lim_{n\to\infty}(M^n)_{ij} &= \sum_{l,m} V_{il}\,\delta_{l1}\,\delta_{1m}\,(V^{-1})_{mj} \\ &= V_{i1}\,(V^{-1})_{1j} \\ &= \rho_i\end{aligned}$$

and

$$\begin{aligned}\lim_{n\to\infty}\sum_j (M^n)_{ij}p_j &= \sum_j \rho_i\,p_j \\ &= \rho_i\end{aligned} \tag{4.11}$$

for all probability distributions $\mathbf{p}$.

4.2 Measurements in Markov Chain Monte Carlo

Observables are functions $\mathbf{A} : \mathbf{\Omega} \to \mathbb{R}$ and can be written as vectors with elements A_i. Given an observable $\mathbf{A}$ and a probability density $\mathbf{p}$ the mean value of $\mathbf{A}$ is

$$\langle\mathbf{A}\rangle_{\mathbf{p}} = \sum_i A_i\,p_i\,. \tag{4.12}$$

In a Monte Carlo procedure, however, at each time the system is definitely in a pure state Z_i corresponding to a distribution $\mathbf{p}^{(i)}$. General distributions build up like a histogram: at each "time step" the actual state, *e.g.* Z_i, is noted by increasing a counter $\tilde{p}_i$ by one. After normalizing, the vector $\tilde{\mathbf{p}}$ thus represents a distribution, which can be used to measure mean values of observables like in Eq. (4.12). If we made infinitely many time steps, $\tilde{\mathbf{p}}$ would reach $\boldsymbol{\rho}$ (see Eq. (4.11)). In practice, the procedure is stopped after a finite number of steps. That is the reason why $\langle\mathbf{A}\rangle_{\tilde{\mathbf{p}}} \neq \langle\mathbf{A}\rangle_{\boldsymbol{\rho}}$. Nonetheless $\langle\mathbf{A}\rangle_{\tilde{\mathbf{p}}}$ is an estimator of $\langle\mathbf{A}\rangle_{\boldsymbol{\rho}}$. The quality of this estimator can be assessed by the variance of $\langle\mathbf{A}\rangle_{\tilde{\mathbf{p}}}$. We will show how to calculate the variance later and we will see that the so-called autocorrelation is an important quantity.

The autocorrelation function is defined as

$$\begin{aligned}c_{\mathbf{A}}(t) :&= \Big\langle(\mathbf{A}(t) - \langle\mathbf{A}\rangle_{\boldsymbol{\rho}})(\mathbf{A}(0) - \langle\mathbf{A}\rangle_{\boldsymbol{\rho}})\Big\rangle \\ &= \langle\mathbf{A}(t)\mathbf{A}(0)\rangle - \langle\mathbf{A}(t)\rangle\langle\mathbf{A}\rangle_{\boldsymbol{\rho}} - \langle\mathbf{A}\rangle_{\boldsymbol{\rho}}\langle\mathbf{A}(0)\rangle + \langle\mathbf{A}\rangle^2_{\boldsymbol{\rho}}\,.\end{aligned} \tag{4.13}$$

How to interpret the time dependent mean values will be shown in several steps. At MC time $t = 0$ the system is in a definite state Z_i. Measurements in a MC

procedure generally start after a so-called thermalization, *i.e.* a (huge) number of steps, after which the system is assumed to be in a typical state from the distribution $\boldsymbol{\rho}$. Assuming a perfect thermalization the probability to start with Z_i is ρ_i, yielding

$$\begin{aligned}\langle \mathbf{A}(0)\rangle &= \sum_i \rho_i \sum_l A_l \, p_l^{(i)} \\ &= \sum_i A_i \rho_i \\ &= \langle A\rangle_{\boldsymbol{\rho}} \, . \end{aligned} \tag{4.14}$$

Thus this is a mean value over a whole ensemble of MC chains. Of course an actual measurement leads to deviations from this value, but the calculation shows that $\langle \mathbf{A}\rangle_{\tilde{\mathbf{p}}}$ is an unbiased estimator of $\langle \mathbf{A}\rangle_{\boldsymbol{\rho}}$.

The meaning of $\langle \mathbf{A}(t)\rangle$ can be defined analogously. At $t = 0$ the system is in state Z_i with probability ρ_i. To calculate the system at time t one has to apply $\mathbf{M}^t$ on $\mathbf{p}^{(i)}$. Afterwards the measurement is to be carried out:

$$\begin{aligned}\langle \mathbf{A}(t)\rangle &= \sum_i \rho_i \sum_l A_l \sum_m (M^t)_{lm} \, p_m^{(i)} \\ &= \sum_l A_l \underbrace{\sum_i (M^t)_{li} \, \rho_i}_{=\rho_l} \\ &= \langle A\rangle_{\boldsymbol{\rho}} \, . \end{aligned} \tag{4.15}$$

Inserting Eqs. (4.14,4.15) in Eq. (4.13) yields

$$c_{\mathbf{A}}(t) = \langle \mathbf{A}(t)\mathbf{A}(0)\rangle - \langle \mathbf{A}\rangle_{\boldsymbol{\rho}}^2 \, . \tag{4.16}$$

The last term we have to consider is $\langle \mathbf{A}(t)\mathbf{A}(0)\rangle$. Again the system is in state Z_i at time $t = 0$, where the first measurement is carried out. Then the state Z_i propagates t times by means of the Markov matrix $\mathbf{M}$ and an additional measurement of observable $\mathbf{A}$ is made. Since thermalization is assumed Z_i is weighted with ρ_i:

$$\begin{aligned}\langle \mathbf{A}(t)\mathbf{A}(0)\rangle &= \sum_i \rho_i \sum_l A_l \sum_m (M^t)_{lm} \, p_m^{(i)} \sum_n A_n \, p_n^{(i)} \\ &= \sum_{i,l} A_l \, (M^t)_{li} \, A_i \, \rho_i \, . \end{aligned} \tag{4.17}$$

The time dependence can be further manipulated using Eq. (4.10):

$$\begin{aligned}(M^t)_{li} &= \sum_{n,m} V_{ln} \, \lambda_n^t \, \delta_{nm} \, (V^{-1})_{mi} \\ &= \underbrace{V_{l1}}_{=\rho_l} \underbrace{\lambda_1^t}_{=1} \underbrace{(V^{-1})_{1i}}_{=1} + \sum_{n>1} V_{ln} \, \lambda_n^t \, (V^{-1})_{ni} \\ &= \rho_l + \sum_{n>1} V_{ln} \, (V^{-1})_{ni} \, \mathrm{e}^{i\varphi_n t} \, \mathrm{e}^{-t/\tau_n} \, , \end{aligned} \tag{4.18}$$

with $\tau_n := -\frac{1}{\log|\lambda_n|} > 0$ and $\varphi_n := \arg(\lambda_n)$.

Inserting Eqs. (4.17,4.18) into Eq. (4.16) one ends up with

$$\begin{aligned} c_{\mathbf{A}}(t) &= \sum_{n>1} \sum_{i,l} A_l \, V_{ln} \, (V^{-1})_{ni} \, A_i \, \mathrm{e}^{i\varphi_n t} \, \mathrm{e}^{-t/\tau_n} \\ &= \sum_{n>1} \tilde{c}_n \, \mathrm{e}^{i\varphi_n t} \, \mathrm{e}^{-t/\tau_n} \ . \end{aligned}$$

If the real $\mathbf{M}$ has complex eigenvalues, they appear in pairs of conjugate numbers. Since $c_{\mathbf{A}}(t)$ has to be a real function, the coefficients have to be such that complex phases disappear, *i.e.*

$$c_{\mathbf{A}}(t) = \sum_{n>1} c_n \, \cos(\alpha_n + \varphi_n t) \, \mathrm{e}^{-t/\tau_n} \ ,$$

where $c_n > 0$ and α_n are real coefficients. Note that $\alpha_n = 0$ and $\varphi_n \in \{0, \pi\}$ if $\lambda_n \in \mathbb{R}$.

However, practice shows that oscillating correlation functions are rather rare. Thus in most cases

$$c_{\mathbf{A}}(t) = \sum_{n>1} c_n \, \mathrm{e}^{-t/\tau_n} \tag{4.19}$$

applies. This function can be normalized via

$$\begin{aligned} \tilde{c}_{\mathbf{A}}(t) : &= \frac{c_{\mathbf{A}}(t)}{c_{\mathbf{A}}(0)} \\ &= \sum_{n>1} d_n \, \mathrm{e}^{-t/\tau_n} \ , \end{aligned} \tag{4.20}$$

with $d_n = c_n / (\sum_{l>1} c_l)$.

4.3 Role of Autocorrelations for Error Estimates

In this section we want to illuminate the role of the autocorrelation function in MC simulations.

Assume our procedure has produced a series of states $\{Z_1, Z_2, \ldots, Z_N\}$ via a Markov process. The probability to get this specific sample is denoted with $p(Z_1, Z_2, \ldots, Z_N)$. Before the sample was drawn a thermalization phase has been applied in order to reach the distribution $\boldsymbol{\rho}$. Thus all marginal distributions are given by

$$\begin{aligned} p(Z_i) &= \sum_{\substack{Z_j \\ j \neq i}} p(Z_1, Z_2, \ldots, Z_N) \\ &= \boldsymbol{\rho}(Z_i) \\ &= \rho_i \ . \end{aligned}$$

The probability to end up with a value A for the sample mean of $\mathbf{A}$ is given by

$$p(A) = \sum_{Z_1,Z_2,\ldots} \underbrace{p(A|Z_1,Z_2,\ldots)}_{=\delta\left(A-\frac{1}{N}\sum_{i=1}^{N} A(Z_i)\right)} \; p(Z_1,Z_2,\ldots) \; .$$

The expectation value of the sample mean is thus

$$\begin{aligned}
\overline{A} &= \int dA \, A \, p(A) \\
&= \frac{1}{N} \sum_{i=1}^{N} \sum_{Z_1,Z_2,\ldots} A(Z_i) \, p(Z_1,Z_2,\ldots) \\
&= \frac{1}{N} \sum_{i=1}^{N} \sum_{Z_i} A(Z_i) \, \boldsymbol{\rho}(Z_i) \\
&= \langle \mathbf{A} \rangle_{\boldsymbol{\rho}} \; .
\end{aligned}$$

Therefore the square of this value can be written as

$$\overline{A}^2 = \frac{1}{N^2} \sum_{i,j=1}^{N} \langle \mathbf{A} \rangle_{\boldsymbol{\rho}}^2 \; ,$$

which we will need later.

In order to calculate the variance of the sample mean we need

$$\begin{aligned}
\overline{A^2} &= \int dA \, A^2 \, p(A) \\
&= \frac{1}{N^2} \sum_{i,j=1}^{N} \sum_{Z_1,Z_2,\ldots} A(Z_i) \, A(Z_j) \, p(Z_1,Z_2,\ldots) \\
&= \frac{1}{N^2} \sum_{i,j=1}^{N} \sum_{Z_1,Z_2} A(Z_1) \, A(Z_2) \, p_{j-i}(Z_1,Z_2) \; ,
\end{aligned}$$

where $p_{j-i}(Z_1,Z_2)$ is the probability that at $t=i$ the system is in state Z_1 and at $t=j$ at state Z_2. Thus the last sum is exactly the mean value $\langle A(j)A(i) \rangle$ and the variance can be written as

$$\begin{aligned}
\mathrm{var}(A) &= \overline{A^2} - \overline{A}^2 \\
&= \frac{1}{N^2} \sum_{i,j=1}^{N} \underbrace{\left(\langle A(j)A(i) \rangle - \langle \mathbf{A} \rangle_{\boldsymbol{\rho}}^2 \right)}_{=c_{\mathbf{A}}(j-i)} \\
&= \frac{1}{N^2} \sum_{i=1}^{N} \sum_{t=1-i}^{N-i} c_{\mathbf{A}}(t) \\
&= \frac{c_{\mathbf{A}}(0)}{N^2} \sum_{i=1}^{N} \sum_{t=1-i}^{N-i} \tilde{c}_{\mathbf{A}}(t) \; .
\end{aligned}$$

Equation (4.20) states that the autocorrelation function decreases exponentially. We therefore approximate the last sum by $\sum_{t=-\infty}^{\infty}$, which is possible since it can be shown that $\tilde{c}_{\mathbf{A}}(t) = \tilde{c}_{\mathbf{A}}(|t|)$ (in the derivation of $\tilde{c}_{\mathbf{A}}(t)$ we have only considered the case $t \geq 0$). This yields

$$\begin{aligned}
\mathrm{var}(A) &= \overline{A^2} - \overline{A}^2 \\
&\lesssim \frac{c_{\mathbf{A}}(0)}{N^2} \sum_{i=1}^{N} \sum_{t=-\infty}^{\infty} \tilde{c}_{\mathbf{A}}(t) \\
&= \frac{c_{\mathbf{A}}(0)}{N} 2 \Big(\sum_{t=0}^{\infty} \tilde{c}_{\mathbf{A}}(t) - \frac{1}{2} \Big) \\
&= \frac{c_{\mathbf{A}}(0)}{N} 2\, \tau_{\mathrm{int}} \,, \qquad (4.21)
\end{aligned}$$

with

$$\tau_{\mathrm{int}} := \sum_{t=0}^{\infty} \tilde{c}_{\mathbf{A}}(t) - \frac{1}{2} \,. \qquad (4.22)$$

τ_{int} is called the *integrated autocorrelation time*. Because $c_{\mathbf{A}}(0)$ is the naive estimator of the variance of the observable $\mathbf{A}$ in the MC procedure, there is an additional factor $2\,\tau_{\mathrm{int}}$ in comparison with uncorrelated sample means. This result can be interpreted as a reduction of the number of uncorrelated data $N_{\mathrm{eff}} = \frac{N}{2\,\tau_{\mathrm{int}}}$.

The integrated autocorrelation time can be estimated by the largest autocorrelation time

$$\tau_{\mathrm{exp}} := \max_{l>1} \{\tau_l\} \,,$$

which is called *exponential autocorrelation time*. It corresponds to the largest eigenvalue of $\mathbf{M}$ beside $\lambda_1 = 1$. A rough estimate is

$$\begin{aligned}
\tau_{\mathrm{int}} &= \sum_{t=0}^{\infty} \tilde{c}_{\mathbf{A}}(t) - \frac{1}{2} \\
&= \sum_{t=0}^{\infty} \sum_{l} d_l\, \mathrm{e}^{-t/\tau_l} - \frac{1}{2} \\
&\leq \sum_{t=0}^{\infty} \mathrm{e}^{-t/\tau_{\mathrm{exp}}} - \frac{1}{2} \\
&= \frac{1}{1 - \mathrm{e}^{-1/\tau_{\mathrm{exp}}}} - \frac{1}{2} \,,
\end{aligned}$$

from which follows that

$$\mathrm{var}(A) \begin{cases} \approx \frac{c_{\mathbf{A}}(0)}{N} & \text{if } \tau_{\mathrm{exp}} \ll 1 \\ \lesssim \frac{c_{\mathbf{A}}(0)}{N} 2\,\tau_{\mathrm{exp}} & \text{if } \tau_{\mathrm{exp}} \gg 1 \end{cases} .$$

4.4 Avoiding Autocorrelations in Our Approach

In the last sections we have seen how autocorrelations can delay MC calculations. In order to decrease autocorrelations, it is common practice to skip several MC steps between succeeding measurements. Furthermore, there exist several methods to estimate the autocorrelation time, such as *binning* or *Jack knife* [35].

However, in our calculations we monitor the time series of some observables and choose a skip large enough to loose visible impact of autocorrelations on the time series. Additionally we make an exponential fit to the autocorrelation function to determine the remaining exponential autocorrelation time. This value is used to correct our error estimates.

Another way to get rid of large autocorrelations is to find update mechanisms which allows for great jumps in the configuration space. In our case the configuration space consists of unit vectors $\mathbf{S}_i$ sited on a chain. We decided to rotate spins in domains of random lengths. The borders i_0 and i_1 of the domain are drawn at random. Each spin from site i_0 to i_1 is rotated according the rotation matrix

$$\mathbf{R} = \mathbf{R}_0\, \mathbf{R}_z(\psi)\, \mathbf{R}_y(\chi)\, \mathbf{R}_z(-\psi)\, \mathbf{R}_0^{\mathrm{T}}$$

with

$$\mathbf{R}_0 := \mathbf{R}_z(\varphi)\, \mathbf{R}_y(\vartheta)\ ,$$

where $\mathbf{R}_l(\alpha)$ denotes the rotation matrix about the l-axis with a rotation angle α. The angles ϑ and φ correspond to the spin at site i_0, *i.e.* $\mathbf{S}_{i_0} = (\sin\vartheta\,\cos\varphi,\ \sin\vartheta\,\sin\varphi,\ \cos\vartheta)^{\mathrm{T}}$. Thus the operation of the first part $\mathbf{R}_0^{\mathrm{T}}$ on $\mathbf{S}_{i_0}$ yields the vector $(0,\ 0,\ 1)^{\mathrm{T}}$, *i.e.* we use $\mathbf{S}_{i_0}$ as a reference direction. The next rotation $\mathbf{R}_z(-\psi)$ does not alter this vector, but it is important for other sites than i_0. $\mathbf{R}_z(\psi)\, \mathbf{R}_y(\chi)\ (0,\ 0,\ 1)^{\mathrm{T}}$ gives $(\sin\chi\,\cos\psi,\ \sin\chi\,\sin\psi,\ \cos\chi)^{\mathrm{T}}$. This direction should be chosen such that the new vector has a large overlap with the old one $(0,\ 0,\ 1)^{\mathrm{T}}$. This can be achieved by drawing an angle $\psi \in [0, 2\pi]$ and a distance $\delta u \in [0, \delta u_{\max}]$ at random, where $\cos\chi = 1 - \delta u$. Finally the system is rotated back to the global coordinate system by applying $\mathbf{R}_0$.

If this procedure is applied to another spin $\mathbf{S}_i$ at a site $i \neq i_0$, the additional $\mathbf{R}_z(-\psi)$ plays an important role. In the reference coordinate system (according to spin $\mathbf{S}_{i_0}$) the spin $\mathbf{S}_i$ might lie near the xy-plane. Then the application of $\mathbf{R}_z(\psi)\, \mathbf{R}_y(\chi)$ could even invert the spin direction, since the angle ψ is arbitrarily large. But if an additional $\mathbf{R}_z(-\psi)$ is applied before, the resulting vector does not deviate much from the original one, because the angle χ is small.

Thus we have found an update procedure which changes a whole domain of spins without altering the relative angles between the spins within this domain. Only the relative angles at spin pairs $(\mathbf{S}_{i_0-1}, \mathbf{S}_{i_0})$ and $(\mathbf{S}_{i_0}, \mathbf{S}_{i_0+1})$ are changed, allowing for relatively large jumps in the configuration space, nevertheless having a

good acceptance. The amount $\delta u_{\max}$ is determined such that the acceptance in the MC procedure is about 60%.

The autocorrelations are worst in parameter regions where polarons (see Chp. 7) appear. An observable which is worth monitoring there is the electron density. Several densities are energetically accessible, but in order to add an additional electron, a FM domain has to be build in an AF background. Certainly this takes a lot of steps in the MC procedure. Thus we raise the skip in this parameter region such that no remaining autocorrelations are to be seen in this observable (*e.g.* for a $L = 50$, $J_H = 6$, $J' = 0.02$, $U = U' = V' = 0$, $\beta = 50$ system several hundred steps).

Chapter 5

Effective Spinless Fermions in the Strong Coupling Kondo Model

Starting[1] from the two-orbital Kondo-lattice model with classical t_{2g} spins, an effective spinless fermion model is derived for strong Hund coupling J_H with a projection technique. The model is studied by Monte Carlo simulations and analytically using a uniform hopping approximation. The results for the spinless fermion model are in remarkable agreement with those of the original Kondo-lattice model, independent of the carrier concentration, and even for moderate Hund coupling J_H. Phase separation, the phase diagram in uniform hopping approximation, as well as spectral properties including the formation of a pseudo-gap are discussed for both the Kondo-lattice and the effective spinless fermion model in one and three dimensions.

5.1 Introduction

The study of manganese oxides such as $La_{1-x}Sr_xMnO_3$ (LSMO) and $La_{1-x}Ca_xMnO_3$ (LCMO) has attracted considerable attention since the discovery of colossal magnetoresistance in these compounds [1, 11]. These materials crystallize in the perovskite-type lattice structure where the crystal field partially lifts the degeneracy of the manganese d-states. The energetically favorable three-fold degenerate t_{2g} levels are populated with localized electrons, which according to Hund's rule form localized $S = 3/2$ spins. The electronic configuration of the Mn^{3+} ions is $t_{2g}^3 e_g^1$ with one electron in the e_g orbital, which is missing in the Mn^{4+} ions. The e_g electrons can move between neighboring Mn ions mediated by bridging O^{2-} $2p$ orbitals. The interplay of electronic, spin, and orbital degrees of freedom along with the mutual interactions, such as the strong Hund coupling J_H of the itinerant electron to localized t_{2g} spins,

[1] This chapter is published in Phys. Rev. B as Ref. [8].

Coulomb correlations, and electron-phonon coupling leads to a rich phase diagram including antiferromagnetic insulating, ferromagnetic metallic, and charge ordered domains [36]. Charge carriers moving in the spin and orbital background show interesting dynamical features [37, 38]. The electronic degrees of freedom are generally treated by a Kondo-lattice model, which in the strong Hund coupling limit is commonly referred to as double-exchange (DE) model, a term first coined by Zener [39].

Monte Carlo (MC) simulations have contributed significantly to our understanding of the manganites. Intense MC simulations for the DE model have been performed by Dagotto *et al* [22] and Furukawa [40] in the space of the classically treated t_{2g} spins. Static and dynamical observables of the Kondo model have been determined [41]. These MC simulations gave first theoretical indications of phase separation (PS) [42] in manganite models. Preliminary studies have been performed to analyze the importance of nearest neighbor Coulomb repulsion in the two-orbital DE model [43] as well as the importance of classical phonons [44].

Many publications are based on the $J_H = \infty$ limit. Here we propose an effective spinless fermion model for the strong coupling limit of the Kondo-lattice hamiltonian, which is equally simple as the $J_H = \infty$ limit but which still contains the crucial physical ingredients of finite J_H. The dynamic variables are e_g electrons with spins parallel to the t_{2g} spins at the respective sites. The influence of antiparallel spins is accounted for by the effective hamiltonian. The derivation of the model is based on a projection technique, analogous to the derivation of the tJ model from the Hubbard model. The role of the Hubbard U is played by J_H which couples to the classical t_{2g} spins. In contrast to the tJ model, the high-energy subspace is thus controlled by classical variables and consequently the resulting model is much simpler than the tJ model. For a given t_{2g} spin configuration, the resulting hamiltonian is a *one-particle* operator. Its electronic trace can be evaluated analytically, once the one-particle energies are known, leading to an effective action for the t_{2g} spins, which can be simulated by Monte Carlo techniques.

The obvious advantage of this approach is the reduction of the dimension of the Hilbert space. This can be exploited in MC simulations by going to larger systems and/or additional degrees of freedom.

For a large range of parameters, the effective spinless fermion model is found to yield very satisfactory results and to perform much better than the rough $J_H \to \infty$ approximation. We compare spin- and charge-correlations as well as quasi-particle spectra of the projection approach with the full two-spin model and with the $J_H \to \infty$ limit.

The effective model is treated without approximations by Monte Carlo simulations as well as by a uniform hopping approximation (UHA) capturing the essential influence of the t_{2g} spins on the e_g electrons. The UHA computation can be performed analytically, particularly in the thermodynamic limit. Most of the UHA results are found to be in striking agreement with MC results. We

find two phase transitions as a function of the chemical potential, one close to the empty band and the second close to a completely filled band. At each phase transition we observe PS, as reported for the upper transition in [42]. For a 1D-chain we derive an analytical expression for the two critical chemical potentials at which (PS) occurs.

For the 3D Kondo-lattice model canonical UHA results yield a phase diagram which displays various types of antiferromagnetic (AF) order including spin-canting, as well as ferromagnetism (FM). Our finite J_H results for 3D are in close agreement with those derived in the limit of infinite Hund coupling [45]. In the grand canonical ensemble we find, however, that only the 3D antiferromagnetic and the 3D ferromagnetic order prevail. The transition is again accompanied by PS.

The paper is organized as follows. In Sec. 5.2 the Kondo-lattice model is introduced. By applying a projection technique in Sec. 5.3 this model is mapped onto the effective spinless fermion model. In Sec. 5.4 we present the phase diagrams and phase separation boundaries in one and three dimensions within a uniform hopping approximation. Results of Monte Carlo simulations for the original and the projected model are discussed in Sec. 5.5. Finally, in Sec. 5.6 we summarize the key conclusions.

5.2 Model hamiltonian

In this paper, we will concentrate on purely electronic (t_{2g}, e_g) properties, leaving phonon degrees of freedom for further studies. As proposed by Dagotto *et al.* [22] and Furukawa [40], the t_{2g} spins $\mathbf{S}_i$ are treated classically, which is equivalent to the limit $S \to \infty$. The spin degrees of freedom are therefore replaced by unit vectors $\mathbf{S}_i$, parameterized by polar and azimuthal angles θ_i and ϕ_i, respectively, that represent the direction of the t_{2g} spin at lattice site $\mathbf{x}_i$. The magnitude of the spin is absorbed into the exchange couplings. It is expedient to use the individual t_{2g} spin directions as local quantization axes for the spin of the itinerant e_g electrons at the respective sites. This representation is particularly useful for the $J_H \to \infty$ limit, but also for the projection technique, which takes spin-flip processes for finite Hund coupling into account.

It is commonly believed that the electronic degrees of freedom are well described by a multi-orbital Kondo-lattice model

$$\hat{H} = -\sum_{i,j,\alpha,\beta,\sigma,\sigma'} t_{i\alpha,j\beta}^{\sigma,\sigma'}\, c_{i\alpha\sigma}^{\dagger}\, c_{j\beta\sigma'} + 2J_H \sum_{i\alpha} \hat{n}_{i\alpha\downarrow} + J' \sum_{<ij>} \mathbf{S}_i \cdot \mathbf{S}_j \ . \qquad (5.1)$$

It consists of a kinetic term with modified transfer integrals $t_{i\alpha,j\beta}^{\sigma,\sigma'}$, where $i(j)$ are site-, $\alpha(\beta)$ orbital-, and $\sigma(\sigma')$ spin indices. The number of lattice sites will be denoted by L and the number of orbitals per site by M. The operators $c_{i\alpha\sigma}^{\dagger}(c_{i\alpha\sigma})$ create (annihilate) e_g-electrons at site x_i in the orbital α with spin parallel ($\sigma =\uparrow$) or anti-parallel ($\sigma =\downarrow$) to the local t_{2g} spin orientation $\mathbf{S}_i$. The

next term describes the Hund coupling with exchange integral J_H. As usual, $\hat{n}_{i\alpha\sigma}$ is the spin-resolved occupation number operator. Usually, the Kondo-lattice hamiltonian contains an additional term proportional to the electron number $\hat{N}_e$, $\hat{H}_c = -J_H \hat{N}_e$, which has been omitted in Eq. (5.1), as it merely results in a trivial shift of the chemical potential $\mu \to \mu - J_H$.

The modified hopping integrals $t_{i\alpha,j\beta}^{\sigma,\sigma'}$ depend upon the geometry of the e_g-orbitals and the relative orientation of the t_{2g} spins:

$$t_{i\alpha,j\beta}^{\sigma,\sigma'} \;=\; t_{i\alpha,j\beta}\, u_{ij}^{\sigma,\sigma'} \;.$$

The first factor on the RHS is given by the hopping amplitudes $t_{i\alpha,j\beta}$ which read

$$t_{i,i+\hat{z}} \;=\; t \begin{pmatrix} 0 & 0 \\ 0 & 1 \end{pmatrix},\; t_{i,i+\hat{x}/\hat{y}} = t \begin{pmatrix} \frac{3}{4} & \mp\frac{\sqrt{3}}{4} \\ \mp\frac{\sqrt{3}}{4} & \frac{1}{4} \end{pmatrix} \tag{5.2}$$

as matrices in the orbital indices $\alpha, \beta = 1(2)$, corresponding to the $x^2 - y^2$ $(3z^2 - r^2)$ orbitals (see e.g. [1]). The overall hopping strength is t, which will be used as unit of energy, by setting $t = 1$. The relative orientation of the t_{2g} spins at site i and j enters via

$$\begin{aligned} u_{i,j}^{\sigma,\sigma} &= c_i c_j + s_i s_j \; e^{i\sigma(\phi_j - \phi_i)} \\ u_{i,j}^{\sigma,-\sigma} &= \sigma(c_i s_j \; e^{-i\sigma\phi_j} - c_j s_i \; e^{-i\sigma\phi_i}) \end{aligned} \;, \tag{5.3}$$

with the abbreviations $c_j = \cos(\theta_j/2)$ and $s_j = \sin(\theta_j/2)$ and the restriction $0 \le \theta_j \le \pi$. The modified hopping part of the hamiltonian is still hermitian, since $u_{i,j}^{\sigma,\sigma'} = \left(u_{j,i}^{\sigma',\sigma}\right)^*$.

Finally, Eq. (5.1) contains a super-exchange term. The value of the exchange coupling is $J' \approx 0.02$ [1], accounting for the weak antiferromagnetic coupling of the t_{2g} electrons. Here we will approximate the local t_{2g} spins classically. For strong Hund coupling $J_H \gg 1$ the electronic density of states (dos) consists essentially of two sub-bands, a lower and an upper 'Kondo-band', split by approximately $2J_H$. In the lower band the itinerant e_g electrons move such that their spins are predominantly parallel to the t_{2g} spins, while the opposite is true for the upper band [46]. Throughout this paper, the electronic density n (number of electrons per site) will be restricted to $0 \le n \le 1$, i.e. predominantly the lower Kondo-band is involved.

5.3 Projection Technique

The separation of energy scales [47] is a well known strategy to simplify quantum-mechanical many-body systems. In the case of manganites, the Hund coupling J_H is known to be much greater than the other parameters t and J'. Consequently, the hopping to antiparallel $e_g - t_{2g}$ configurations can be treated in second order perturbation theory [48, 49] by a projection approach. On the low energy scale, the dynamical variables are e_g electrons with spin parallel

to the local t_{2g} spins. The virtual excitations $(i\alpha\uparrow) \rightarrow (j\beta\downarrow) \rightarrow (i'\alpha'\uparrow)$, which are mediated by the hopping matrix, lead to an effective spinless fermion hamiltonian

$$\begin{aligned}\hat{H}_p = &- \sum_{i,j,\alpha,\beta} t^{\uparrow\uparrow}_{i\alpha,j\beta}\, c^\dagger_{i\alpha}\, c_{j\beta} - \sum_{i,\alpha,\alpha'} \left(\sum_{j,\beta} \frac{t^{\uparrow\downarrow}_{i\alpha',j\beta}\, t^{\downarrow\uparrow}_{j\beta,i\alpha}}{2J_H} \right) c^\dagger_{i\alpha'} c_{i\alpha} \\ &- \sum_{[i\neq i'],\alpha,\alpha'} \left(\sum_{j,\beta} \frac{t^{\uparrow\downarrow}_{i'\alpha',j\beta}\, t^{\downarrow\uparrow}_{j\beta,i\alpha}}{2J_H} \right) c^\dagger_{i'\alpha'} c_{i\alpha} + J' \sum_{<ij>} \mathbf{S}_i \cdot \mathbf{S}_j \ .\end{aligned} \tag{5.4}$$

The effective hamiltonian contains the kinetic energy of e_g electrons with spin parallel to the t_{2g} spins (first term). The kinetic energy is optimized by aligning all t_{2g} spins which is the usual ferromagnetic double exchange effect. The second term describes an additional hybridization and favors antiferromagnetic t_{2g} spins leading to an effective antiferromagnetic interaction $J_{\rm eff}$ which is generally stronger than J'. The "three-site" hopping processes of the third term are of minor influence. We will see that this term is in general negligible. On the other hand, its inclusion does not really increase the numerical effort. Eq. (5.4) is valid for arbitrary hopping matrices $t_{i\alpha,j\beta}$. In subsequent sections, however, the discussion will be restricted to nearest-neighbor hopping only.

The hamiltonian Eq. (5.4) constitutes a spinless fermion model, similar to the one obtained in the $J_H \rightarrow \infty$-limit, which can be treated numerically along the lines proposed by Dagotto and coworkers [22] and Furukawa [40]. Finite J_H values can thus be treated with the same numerical effort as the case $J_H = \infty$. In the MC simulations the weight for a t_{2g} spin configuration is determined by the grand canonical trace over the fermionic degrees of freedom in the one-electron potential created by the t_{2g} spins.

The obvious advantage of Eq. (5.4) as compared to Eq. (5.1) is the reduced Hilbert space.

5.4 Uniform Hopping approximation

Before discussing approximation-free MC results for the effective spinless fermion model, we will investigate the main features of the hamiltonian (5.4) by a uniform hopping approximation proposed by van-den-Brink and Khomskii [45]. To this end, we introduce two different mean angles between neighboring t_{2g} spins, one in z-direction (θ_z) and one in the xy-plane (θ_{xy}). It should be stressed that θ_z and θ_{xy} are relative angles between adjacent spins, with values between 0 and π, and are not to be confused with the polar angles θ_i. We assume that these angles are the same between all neighbor spins, *i.e.* $\mathbf{S}_i \cdot \mathbf{S}_{i\pm\hat{z}} = \cos\theta_z$ for all lattice sites i and $\mathbf{S}_i \cdot \mathbf{S}_{i\pm\hat{x}} = \mathbf{S}_i \cdot \mathbf{S}_{i\pm\hat{y}} = \cos\theta_{xy}$. The allowed spin configurations include, among others, ferro- and antiferromagnetism as well as spin canted states. The impact of the t_{2g} spins on the hopping amplitudes simplifies to

$$u_z^{\sigma,\sigma} = \cos(\frac{\theta_z}{2}) \quad , \qquad u_z^{\sigma,-\sigma} = \sin(\frac{\theta_z}{2}) \ .$$

for hopping processes along the z-direction and similarly for $u_{xy}^{\sigma,\sigma'}$ for electron motion in the xy-plane. The hopping matrix is now translationally invariant. The inner product of the t_{2g} spins entering the super-exchange reads

$$\mathbf{S}_i \cdot \mathbf{S}_{i+\hat{z}} = \cos\theta_z = 2u_z^2 - 1$$

and similarly for neighboring pairs in the xy-plane.

5.4.1 Phase Separation in 1D systems

First we consider the simplest case, namely a 1D chain in z-direction and we ignore the additional three-site hopping (third term in Eq. (5.4)). At the end of this section we will show that it can indeed be neglected. Due to the symmetry of the hopping elements the $x^2 - y^2$-orbitals form an irrelevant dispersionless band, which will be ignored in the sequel. The influence of the average spin orientation is captured in the uniform hopping amplitude u. Assuming periodic boundary conditions, the hamiltonian simplifies to

$$\hat{H} = -u \sum_{\langle ij \rangle} c_i^\dagger c_j - \frac{1-u^2}{J_H} \sum_i c_i^\dagger c_i + J'L\big(2u^2 - 1\big) \,, \tag{5.5}$$

where we have dropped orbital indices. The virtual hopping processes couple merely to the density and the dispersion of the spinless fermions is given by the shifted tight-binding band structure

$$\epsilon_k = -2u\cos(k) - (1-u^2)/J_H \,. \tag{5.6}$$

The band width is $4u$. It vanishes accordingly for AF order and reaches a maximum for FM order. In Fig. 5.1 the resulting band-filling is schematically depicted for zero temperature as function of chemical potential and hopping amplitude. The condition for an empty/ filled band depends on the 'effective chemical potential'

$$\tilde{\mu} := \big(\mu + \tfrac{1}{J_H}(1-u^2)\big)/u \,. \tag{5.7}$$

According to $\mu < \min_k(\epsilon_k)$, the band is empty if $\tilde{\mu} < -2$. For the completely filled band the condition reads $\tilde{\mu} > 2$. Partial filling is possible for intermediate values of the chemical potential ($-2 < \mu < 2$) if the hopping amplitude exceeds a threshold $u^*(\mu)$. The logarithm of the grand canonical partition function reads

$$\ln Y = \sum_k \ln\left(1 + e^{-\beta(\epsilon_k - \mu)}\right) - \beta J'L\big(2u^2 - 1\big) \,.$$

In the thermodynamic limit ($L \to \infty$) and for $T = 0$ the free energy per lattice site is

$$f = uE(\tilde{\mu}) - u\,\tilde{\mu}\,N(\tilde{\mu}) + J'(2u^2 - 1) \,, \tag{5.8}$$

with $E(x)$ being the mean kinetic energy and $N(x)$ the mean particle number of a tight-binding band with dispersion $-2\cos(k)$. For $|x| \leq 2$ these quantities are

$$E(x) = -\frac{\sqrt{4-x^2}}{\pi} \,, \quad N(x) = \frac{1}{2} + \frac{\arcsin(x/2)}{\pi} \,.$$

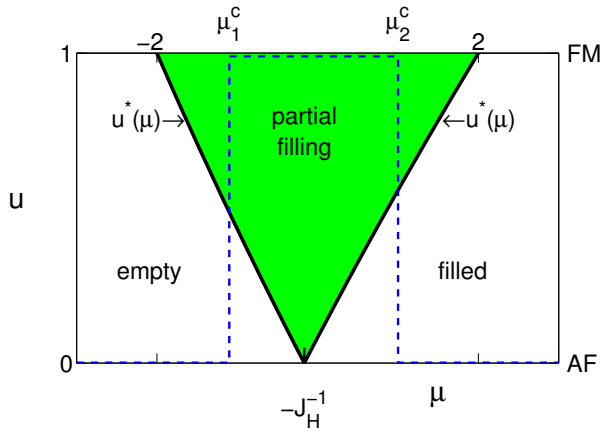

Figure 5.1: Filling of the tight-binding band depending upon chemical potential and hopping amplitude. Condition for partial filling: $u > u^*(\mu)$. The minimum free energy solution in UHA (dashed line) exhibits a jump (phase separation) from AF to FM order at μ_1^c and back to AF order at μ_2^c.

The kinetic energy $E(x)$ is zero for the empty band ($x < -2$), as well as for the completely filled band ($x > 2$). The mean particle number $N(x)$ is zero if the band is empty and unity if it is full. Fig. 5.2 shows the free energy as a function of chemical potential and hopping amplitude u. We find local minima at $u = 0$ (AF order) and $u = 1$ (FM order). The kinetic terms decrease with increasing u, favoring FM order, while the t_{2g} spin energies increase with increasing u, favoring AF order. The global minimum switches from AF to FM at the critical chemical potential $\mu = \mu_1^c$ and back to AF at $\mu = \mu_2^c$. The values for the critical chemical potential follow from the condition $f|_{u=0} = f|_{u=1}$, yielding

$$(\mu^c + 1/J_H)\, N_0(\mu^c) + 2J' = \mu^c\, N(\mu^c) - E(\mu^c)\ , \tag{5.9}$$

where $N_0(\mu^c)$ denotes the mean particle number for $u = 0$, i.e. for perfect AF order. In this case, the tight-binding band is dispersionless and $N_0(\mu^c)$ is either zero or one, depending upon the actual value of the chemical potential.

For the standard parameter set $J_H = 6$ and $J' = 0.02$ the numerical values for μ^c are $\mu_1^c = -1.6730$ and $\mu_2^c = 1.03431$.

The UHA solution corresponds to the global minimum of the free energy. Its location is depicted in Fig. 5.1 and the corresponding densities are shown as lines in Fig. 5.3. For large negative chemical potential the system is antiferromagnetic and the e_g band is empty. At μ_1^c, AFM domains with zero electron density coexist with FM domains with finite density n_1. Increasing μ leads to ferromagnetism, and the filling increases gradually with μ, following the tight binding formula $n = \arccos(-\mu/2)/\pi$.

At μ_2^c, FM domains with density $n_2 > n_1$ coexist with AFM domains of density one. Finally, for $\mu > \mu_2^c$, the system jumps back to antiferromagnetism, now at

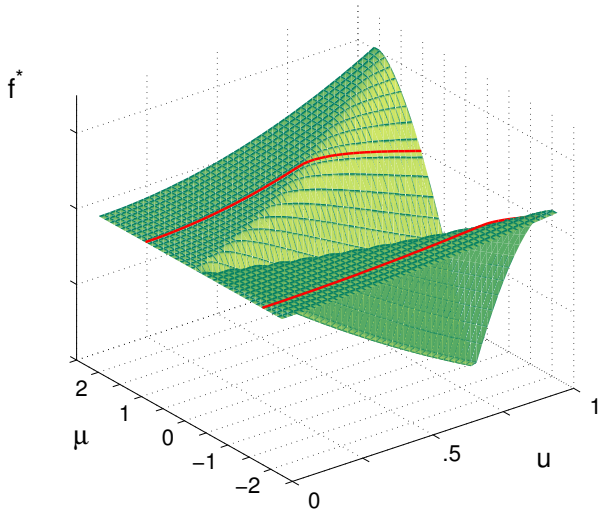

Figure 5.2: Free energy as a function of chemical potential and hopping amplitude u for $T = 0$, $J_H = 6$ and $J' = 0.02$. The solid lines are for μ_1^c and μ_2^c, respectively. For the sake of clarity, $f(u = 0, \mu)$ has been subtracted.

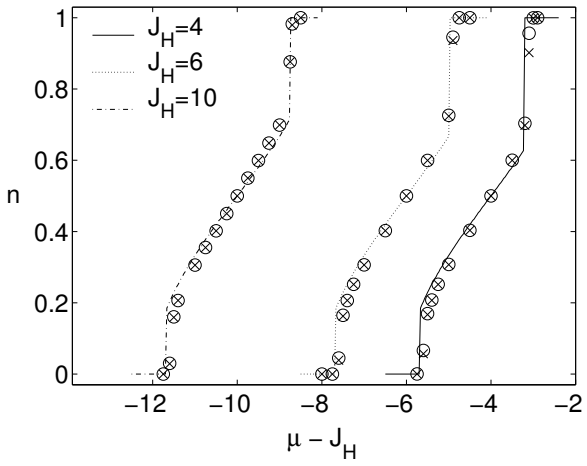

Figure 5.3: Electron density versus chemical potential for $J_H = 4, 6$, and 10 (right to left), and $J' = 0.02$. The lines correspond to UHA. MC results at $\beta = 50$, $L = 20$ for the spinless fermion model H_p (circles) are compared with those for the DE model H (crosses). Error bars of the MC data are smaller than the symbols.

density one. We thus see that the system exhibits phase separation. It should be pointed out that PS is suppressed if nearest-neighbor Coulomb repulsion among e_g electrons is included into the model [50].

Let us now discuss the values of $\mu_{1,2}^c$ and the size of the discontinuity in n. According to Eq. (5.9), the first critical chemical potential $\mu_1^c = \mu^c(J')$, cor-

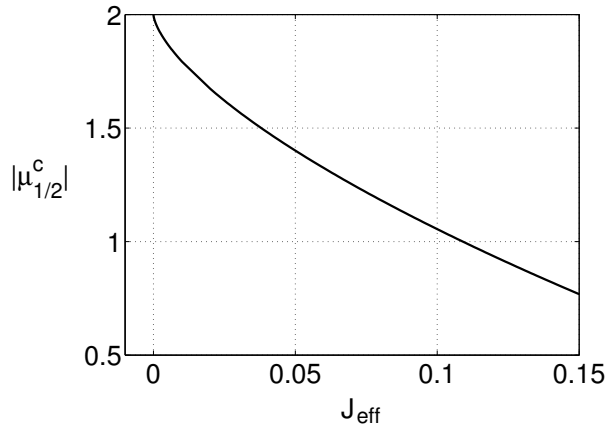

Figure 5.4: Dependence of the critical chemical potential $|\mu^c_{1,2}|$ on the effective exchange coupling J_{eff}.

responding to $N_0(\mu) = 0$, is independent of the actual value of J_H. Here the effective antiferromagnetic interaction J_{eff} purely stems from the superexchange coupling of the t_{2g} spins, $J_{\text{eff}} = J'$. This does, however, not mean that the Hund coupling is irrelevant for this phase transition. On the contrary, the phase transition is driven by the FM tendency introduced by the Hund coupling. The independence of J_H in our results means that there are no second order corrections to the $J_H = \infty$ limit. The dependence of μ^c on J' is depicted in Fig. 5.4.

Now we turn to the second phase transition corresponding to $N_0(\mu^c) = 1$. This transition is controlled by the stronger effective exchange coupling

$$J_{\text{eff}} = J' + \tfrac{1}{2J_H} \,, \tag{5.10}$$

as can be seen from Eq. (5.9), or directly from Eq. (5.5) at $N = 1$. Due to the particle-hole relation $N(-\mu) + N(\mu) = 1$ the second critical chemical potential is given by $\mu^c_2 = -\mu^c(J_{\text{eff}})$, depicted in Fig. 5.4. In the limit $J_H \to \infty$ we have $\mu^c_1 = -\mu^c_2$. The density discontinuity is $\Delta n := N(\mu^c_1) = \Delta n(J')$ at μ^c_1 and $\Delta n := 1 - N(\mu^c_2) = \Delta n(J_{\text{eff}})$ at μ^c_2. It is depicted in Fig. 5.5. Series expansion of Eq. (5.9) with respect to μ^c about $\mu^c = -2$ yields $\Delta n = (3J'/\pi^2)^{1/3}$. At $J_{\text{eff}} = 0$ the slope of the curve diverges, implying that already an infinitesimal J_{eff} leads to phase separation in this regime.

For realistic parameter values ($J_H = 6$ and $J' = 0.02$) we find $\Delta n_1 \approx 0.18$ and $\Delta n_2 \approx 0.3$, respectively. The second value is mainly driven by the virtual hopping, which increases the tendency towards PS.

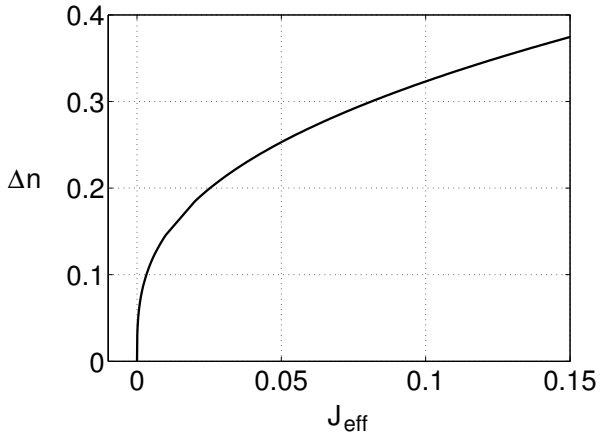

Figure 5.5: Discontinuity in n as a function of the effective exchange coupling J_{eff}.

5.4.2 Impact of "three-site-terms"

Here we consider the impact of the additional hopping in Eq. (5.4), which in the 1D case with one orbital results in a next-nearest neighbor hopping

$$\hat{H}^* = -\frac{1-u^2}{2J_H} \sum_i c_{i+2}^\dagger \, c_i + h.c. \qquad .$$

Combined with the terms of Eq. (5.5), the resulting single-particle dispersion reads

$$\epsilon_k = -2u \cos k \; - \; \frac{1-u^2}{J_H} \; - \; \frac{1-u^2}{J_H} \cos(2k) \; .$$

In the limit $u \to 1$ we recover the original tight-binding band. The density of states has additional van Hove singularities. Contrary to the dispersion of Eq. (5.5), the band width remains finite in the limit $u \to 0$, due to $\hat{H}^*$.

Next we derive the conditions for phase separation. In the limit $T \to 0$, the free energy is given by

$$f = \int_{-\infty}^{\mu} d\epsilon \; \rho_u(\epsilon)(\epsilon - \mu) \; - \; J'(2u^2 - 1) \; ,$$

where $\rho_u(\epsilon)$ denotes the density of states corresponding to ϵ_k. Numerical evaluation shows that the minima of f are still at $u = 0$ and $u = 1$. The condition for phase separation is therefore still $f|_{u=0} = f|_{u=1}$. In principle, due to the finite width of the band at $u = 0$ intermediate particle numbers $N_0(\mu^c)$ are possible. A detailed calculation shows, however, that for realistic parameters, only $N_0(\mu^c) = 0$ or $N_0(\mu^c) = 1$ can meet the phase separation criterion. For $N_0(\mu^c) = 0$ and $N_0(\mu^c) = 1$, however, no hopping is possible and consequently the additional hopping term vanishes. Therefore, the criterion for PS is the

same as in Eq. (5.9) and the three-site hopping has no influence on the critical chemical potentials μ_c at which phase separation occurs.

In general, the modification of the bandwidth due to next-nearest neighbor hopping is small. It has almost negligible impact on the results. On the other hand it poses little extra-effort to include it in MC simulation.

5.4.3 Phase Diagram in 3D systems

We now turn to the 3D case. In uniform hopping approximation, the super-exchange reads

$$\hat{H}_{se} = J' L^3 \big(2(2u_{xy}^2 - 1) + (2u_z^2 - 1)\big)$$

where L denotes the linear dimensions of the system. Upon substituting uniform hopping amplitudes into Eq. (5.4), the fermionic part of the hamiltonian can easily be diagonalized. The one-particle energies are given by the eigenvalues of a 2×2 matrix with matrix elements

$$\begin{aligned}
\epsilon_{11}(k) =& \frac{3}{2}\Big(- u_{xy}(\cos k_x + \cos k_y) - (1 - u_{xy}^2))/J_H \Big) \\
\epsilon_{12}(k) =& \frac{\sqrt{3}}{2}\, u_{xy}\big(\cos k_x - \cos k_y \big) = \epsilon_{21}(k) \\
\epsilon_{22}(k) =& - 2u_z \cos k_z - u_{xy}\big(\cos k_x + \cos k_y \big)/2 \\
& - \big(1 - u_z^2 + (1 - u_{xy}^2)/4\big)/J_H
\end{aligned} \tag{5.11}$$

where the subscript 1 (2) refers to $x^2 - y^2$ ($3z^2 - r^2$) orbitals. The symmetry of the e_g-wavefunction has been exploited in the above expressions. As a consequence of the UHA with two different angles θ_z and θ_{xy}, virtual hopping processes cannot induce transitions between different orbitals, and J_H appears only in the diagonal elements of the matrix.

We determine the phase diagram in the *canonical ensemble* at $T = 0$ with respect to electron density n and exchange coupling J' for fixed Hund coupling $J_H = 8$, with Eq. (5.11) evaluated on a 20^3 momentum lattice. For each parameter set, the free energy is minimized with respect to the hopping amplitudes. The resulting phase diagram is depicted in Fig. 5.6. At very low doping, 3D antiferromagnetic (G) order dominates, irrespective of the value of J', as long as $J' > 0$. Increasing the electron concentration for $J' > 0.02$, the system favors first a C-phase, then an A-phase, and finally ferromagnetism (F). Similar results have been found for the $J_H = \infty$ limit [45]. Finite values for J_H have almost negligible influence on the phase diagram for densities $n < 0.5$. The G-phase has not been reported in [45] since it has not been taken into consideration. For small super-exchange of the t_{2g} spins ($J' < 0.018$) the transition from G to A phase evolves via spin canting. By increasing the electron doping, the F-phase is reached without canting. The situation is more complex for larger values of J'. Fig. 5.7 shows the optimal angles θ_z and θ_{xy} as a function of the electron density n for $J' = 0.025$ and $J_H = 8$. For $n < 0.039$, there is 3D AF order

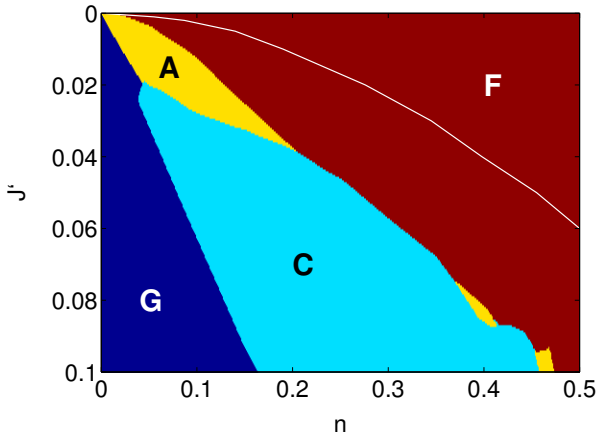

Figure 5.6: Canonical $T = 0$ UHA phase diagram of the spinless two-orbital Kondo-lattice model with classical t_{2g} spins for $J_H = 8$. Depending upon the electron concentration of the canonical ensemble and the super-exchange, G-type, A-type, C-type antiferromagnetic phases or the ferromagnetic phase (F) are observed. Meaning of phases: G=(AF,AF); A=(FM,AF); C=(AF,FM); F=(FM,FM), where the first entry denotes the order in the xy-plane and the second in z-direction. The solid line represents the phase-boundary between G- and F-order, respectively, obtained in a grand canonical ensemble.

(G-type) with an increasing tendency towards canting between t_{2g} spins in the xy plane. At $n \simeq 0.04$ this tendency is strongly reduced while at the same time $\cos(\theta_z)$ discontinuously jumps to zero and we gradually enter the C-phase by aligning the spins along the chains in z-direction. The ferromagnetic chains are not perfectly antiferromagnetically stacked. At about 8% electron density we observe a phase transition to the A-phase. At $n \approx 0.15$ an abrupt transition to 3D ferromagnetic order occurs.

Besides the analysis for the canonical ensemble, computations have been performed for the *grand canonical ensemble* as well. The results are significantly different. In the grand canonical ensemble only the G and the F phase remain. The white solid line in Fig. 5.6 represents the phase boundary between the two phases. For fixed J', the behavior is similar to that of the 1D system, depicted in Fig. 5.3. Below a critical chemical potential μ_1^c the electron density is zero and the t_{2g} spins have AF order. At $\mu = \mu_1^c$, zero density and a finite density n_1, given by the solid line in Fig. 5.6, coexist. Concurrently with phase separation, AF- and FM order coexist. Above μ_1^c the density increases monotonically. The second transition at μ_2^c is not shown in Fig. 5.6 as it occurs close to $n = 1$. Therefore, the grand canonical UHA result does not exhibit the additional magnetic phases (A and C), which are observed in experiment. The relevant densities are never stabilized.

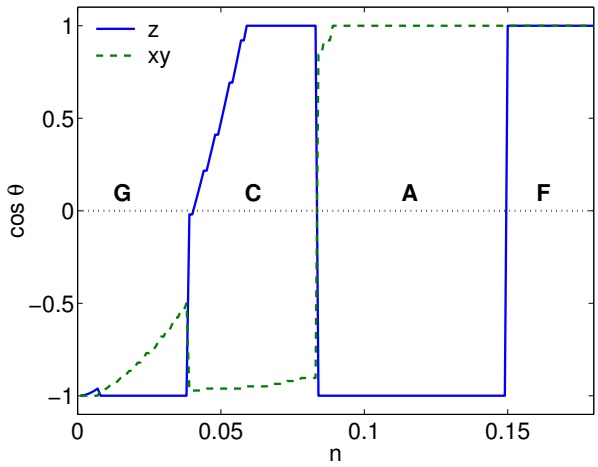

Figure 5.7: Evolution of the optimal angles θ_z and θ_{xy} as function of the electron density n at $J' = 0.025$, $J_H = 8$. Further details like in Fig. 5.6.

5.5 MC simulations for 1D systems

In this section we compare MC results, obtained for the original double exchange (DE) model (5.1), with those for the effective spinless fermion model (Eq. (5.4)), where the additional ("three-site") hopping term has been neglected. We use the grand canonical Monte Carlo method introduced in [42] with open boundary conditions (obc).

We restrict the discussion to 1D systems. There is no reason to believe that the performance of the approximation of effective spinless fermions is different in higher dimensions. Furthermore, the approximation has little influence on the orbital degrees of freedom and we restrict the analysis to the one-orbital model. In all simulations, the super-exchange coupling of the t_{2g} spins is $J' = 0.02$.

Fig. 5.3 shows the dependence of the electron density on the chemical potential. The system parameters are $L = 20$, $\beta = 50$, and J_H is varied between $J_H = 4$ and $J_H = 10$. All results for the two models are in almost perfect agreement. The 'largest' difference can be observed at μ_2^c for $J_H = 4$. The lines in Fig. 5.3 represent the results of the uniform hopping approximation, which are strikingly close to the MC data points. The discontinuities are more pronounced in UHA than in the MC data, which can partially be attributed to the fact that the UHA results are for $L = \infty$ and $T = 0$. The treatment of finite temperatures in the UHA requires the determination of the number of t_{2g} configurations at a given u and is the subject of current investigations [50].

The structure factor of the t_{2g} spins has been calculated for various densities n in the grand canonical ensemble by adjusting the chemical potential. The results are illustrated in Fig. 5.8. Again the data for the two models, Kondo- and effective spinless fermion model, are in perfect agreement within the error bars. Corroborating the UHA results of the previous section, the filled band

$(n = 1)$ has a peak at $k = \pi$, corresponding to AF order. For decreasing density the ferromagnetic peak increases up to $n = 1/2$ and then it decreases again. The inset shows the nearest neighbor and next nearest neighbor spin correlation function versus density. We observe that both models yield the same magnetic behavior: AF order at low and high density and a ferromagnetic phase at intermediate fillings. The pronounced peak at $k = \pi$ for $n = 1$ results from (virtual) spin-flip processes, driven by the relatively strong exchange coupling $J_{\text{eff}} = 0.103$, Eq. (5.10). Contrariwise, the AF structure near $n = 0$ is much less pronounced as it is merely driven by the weak super-exchange coupling $J' = 0.02$. Fig. 5.9 shows the structure factor for the t_{2g} spins at $n = 1$

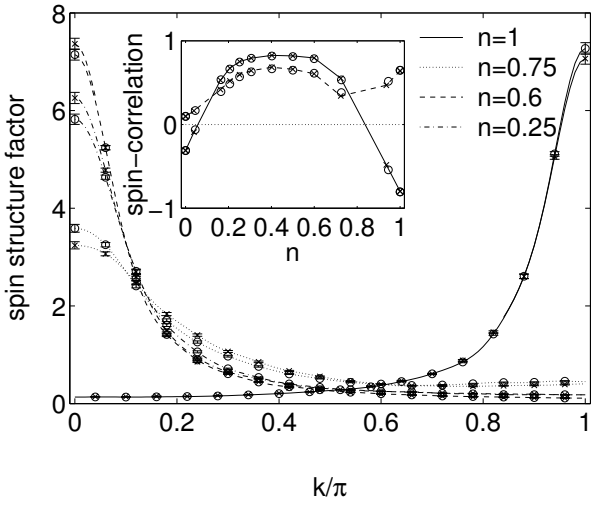

Figure 5.8: Structure factor for the t_{2g} spins at various electron densities with $J_H = 6$, $\beta = 50$, and $L = 20$, for the spinless fermion model H_p (circles), and for the DE model H (crosses). When not shown, error bars are smaller than the symbols. The inset shows the nearest neighbor (solid line) and next nearest neighbor (dashed line) t_{2g} spin correlation.

for different values of J_H. The AF peak decreases with increasing J_H and degenerates to a broad structure in the limit $J_H \to \infty$. Obviously, the inclusion of the second order term to the effective spinless fermion model, which is missing in the commonly used $J_H = \infty$ limit, and which provides the strong exchange coupling J_{eff}, is crucial for the correct description of the AF order at high electron density. The inset shows the spin structure for $n \approx 3/4$, at which the system exhibits ferromagnetic order. In this case, the FM correlations increase with increasing J_H.

As a further test for the spinless fermion model, the electronic contribution to the total energy is shown in Fig. 5.10. The energy for the Kondo-lattice model (first two terms in Eq. (5.1)) is compared with the corresponding contributions in the effective spinless fermion model (Eq. (5.4)) in Fig. 5.10. For all fillings the results are in very good agreement.

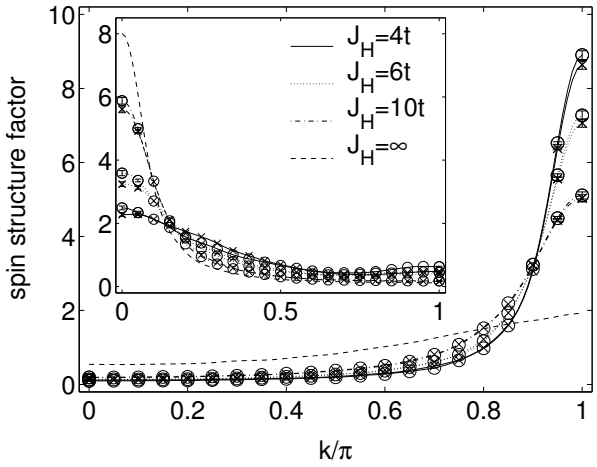

Figure 5.9: Spin structure factor at $n = 1$ (inset: $n \approx 0.75$) for different values of J_H. Same symbols and parameters as in Fig. 5.8. In the limit $J_H \to \infty$ (dashed line) the intensity of the AF peak is considerably reduced.

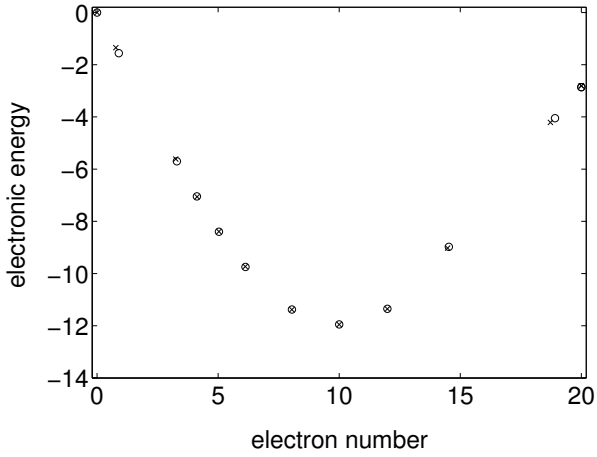

Figure 5.10: Electronic contribution to the total energy versus electron number for $\beta = 50$, $L = 20$, and $J_H = 6$. Results for the DE model $\hat{H}$ (crosses) are compared with those for the spinless fermion model $\hat{H}_p$ (circles).

Quantitatively, the largest differences are found for $n = 1$. For this density the dependence of the energy on J_H is studied in Fig. 5.11. A detailed comparison reveals that the effective model describes the electronic energy extremely well, even in the moderate coupling regime. The ubiquitous $J_H = \infty$ approximation, on the other hand, yields zero electronic energy. For the parameters underlying Fig. 5.11, the t_{2g} spins are antiferromagnetically ordered and the lower Kondo-band, or rather the single band of the spinless fermion model, is completely filled. Nevertheless, the kinetic electronic energy is finite due to (virtual) spin-flip processes. It should be pointed out that the additional (three-site) hopping

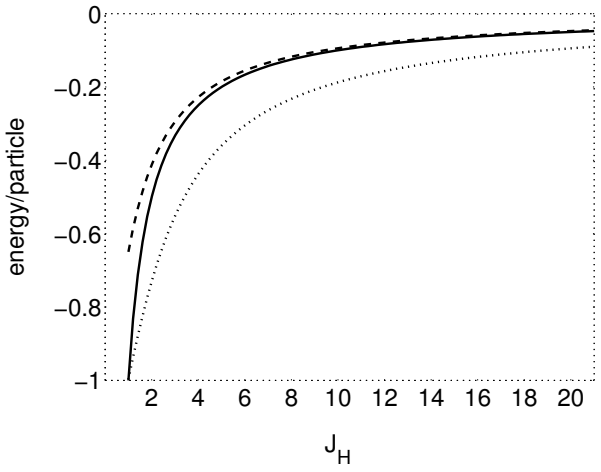

Figure 5.11: Electronic energies versus Hund coupling J_H for a completely filled 20-site chain at $T = 0$. Kinetic energy (dotted line) and total electronic energy (dashed lines) for the Kondo-lattice model. The solid line represents the total electronic energy for the effective spinless fermion model.

term in Eq. (5.4) has no influence on this result as the band is entirely filled.

Next we study the spectral function $A_k(\omega)$ in the grand canonical ensemble for various mean electron densities covering the regimes for AF and FM order, as well as phase separation. In all cases the system geometry is a 20-site chain with open boundary conditions at inverse temperature $\beta = 50$, and exchange couplings $J' = 0.02$, and $J_H = 6$. We start out with the spectra in Fig. 5.12 for strong FM order at a mean particle density of $n = 1/2$. According to the inset of Fig. 5.8 the spin-correlations are 0.82 and 0.67 for nearest and next-nearest neighbors, respectively. The spectral function, depicted in Fig. 5.12, resembles closely that of a tight-binding model, valid for perfect FM order. The bandwidth is slightly reduced, and for k-values close to the fermi momentum, $A_k(\omega)$ exhibits some minor shoulders. The width (HWHM) of the peaks agrees with γ, the value by which the finite-size delta peaks have been broadened. The inset displays the density of states (dos), which agrees with the tight-binding density of states for open boundary conditions. Next we increase the mean density to $n = 0.75$, corresponding to a chemical potential close to μ_2^c. The spin order is still predominantly ferromagnetic. The results in Fig. 5.13 show that both models yield very similar results, namely a tight-binding type of quasiparticle band. The spectral peaks are, however, significantly broader than the mock width γ and upon approaching the fermi momentum the width increases asymmetrically towards the fermi level. The origin of the broad structures are the random deviations of the t_{2g} spins from perfect FM order. The resulting density of states has piled up spectral weight in the center and reveals a precursor of a pseudo-gap at the fermi energy. Interestingly, the dos is almost center-symmetric and a mirror image of the 'pseudo-gap' occurs also at the lower band edge.

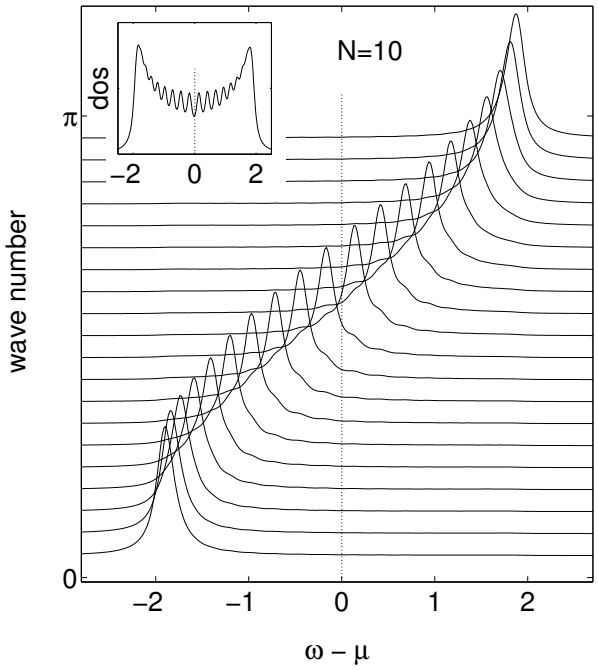

Figure 5.12: Spectral function obtained by a grand canonical simulation for $n = 1/2$ with $J_H = 6$, $L = 20$ and $\beta = 50$. An intrinsic linewidth $\gamma = 0.1$ has been added. The results for the Kondo model and the effective spinless fermion model are indistinguishable.

The next panel depicts results for $n = 0.95$, correspond to a chemical potential slightly above μ_{c2}, where the spin order is predominantly antiferromagnetic. Now the pseudo-gap, as discussed by Moreo *et al.* [51], is clearly visible. Again we observe a 'mirror pseudo-gap' at the lower band edge. There is still good qualitative agreement between the results of the two models. Quantitatively, however, there are deviations in the structures below the pseudo-gap. The density of states is still remarkably well described by the spinless fermion model.

In the opposite limit of low carrier concentration ($n = 0.05$), the chemical potential is close to μ_{c1}, where we find similar features. Again, together with the coexistence of FM and AFM order a pseudo-gap shows up at the chemical potential as well as at the upper band edge. The pseudo-gap is less pronounced in this case, where the antiferromagnetic exchange coupling J' is much smaller than J_{eff} at μ_2^c.

In both models a considerable amount of spectral weight is transferred from the band edges to the center. Interestingly, the density of states is again almost center-symmetric. The pseudo-gap is present in the spectral function irrespective of the wave vector k. Moreo et al. argued that the pseudo-gap is formed due to the presence of mixed phases with irregular formations of FM domains. In contrast to this interpretation, we find the pseudo-gap also in the perfect AF regime with a single electron (hole).

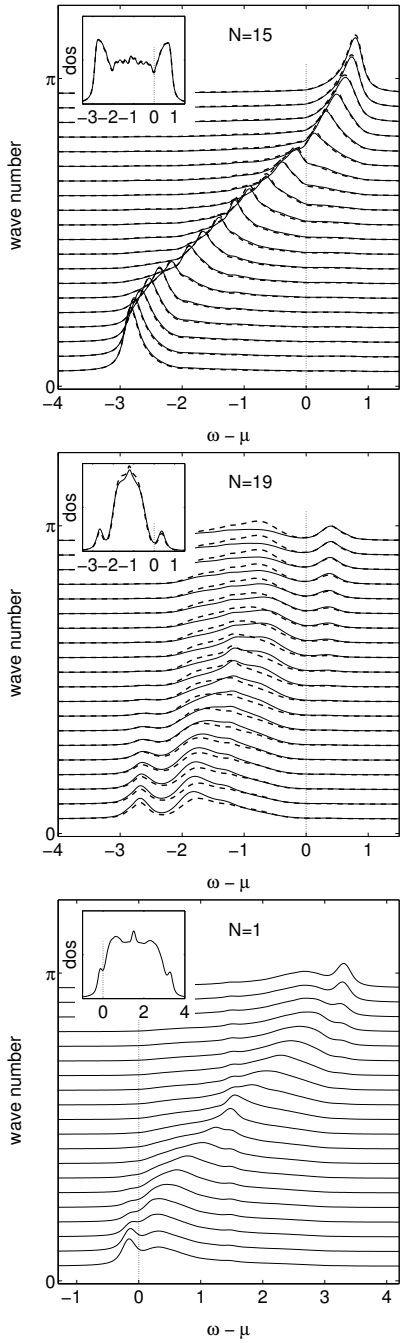

Figure 5.13: Same as Fig. 5.12. The indicated particle numbers correspond to $n = 0.75$ $n = 0.95$, and $n = 0.05$. Results for the Kondo model are represented by solid lines and those for the effective spinless fermion model by dashed lines.

Generally we observe, in agreement with ARPES experiments [52], that the width of peaks increases towards the fermi energy and the spectral intensity decreases since spectral weight is transferred to the unoccupied part of the spectrum, which is not visible in ARPES. Furthermore, the peaks are generally much broader than the experimental resolution.

5.6 Conclusions

We have developed an effective spinless fermion model for the strong coupling multi-orbital Kondo-lattice model. The effective model has a reduced Hilbert space and is particularly suitable for MC simulations. The numerical complexity is the same as that of the $J_H = \infty$ model. The reduced Hilbert space allows one to study higher spatial dimensions and/or additional degrees of freedom, such as phonons.

Based on the evaluation of various observables the effective spinless fermion model performs strikingly well, even for moderate Hund coupling.

It appears that virtual spin-flip processes included in our approach, which are missing in the $J_H = \infty$ model, are crucial for the antiferromagnetic phase close to half-filling ($n = 1$), where they provide a strong effective exchange coupling $J_{\text{eff}} = J' + \frac{1}{2J_H}$.

Two phase transitions from AF- to FM-order and vice versa are observed, accompanied by phase separation. Analytic expressions for the chemical potential at which phase separation occurs in a 1D chain have been derived in uniform hopping approximation (UHA). It has been shown, however, that they are in extremely good agreement with approximation-free MC results.

The UHA phase diagram of the 3D spinless fermion model has been determined. In canonical ensembles, the magnetic phase diagram is in qualitative agreement with that obtained in previous studies for the $J_H = \infty$ limit. Experimentally observed phases, like G-, A-, C-, and F-order are found. On the other hand, grand canonical ensemble calculations show that only 3D AF and 3D FM order prevail. The transition between the two phases is accompanied by phase separation. Densities, required for other phases, are not stable in UHA.

The spectral functions show a remarkable center-symmetry. In the AF phase, at low and high electron density, a pseudo-gap structure is observed at the chemical potential and a mirror image at the opposite edge of the spectrum.

In passing, it should be noted that nearest-neighbor Coulomb repulsion of the e_g-electrons in a two-orbital model can be detrimental for phase separation. Detailed results will be discussed elsewhere [50].

5.7 Acknowledgments

This work was partially supported by the Austrian Science Fund (FWF), project P15834-PHY.

Chapter 6

Uniform Hopping Approach to the FM Kondo Model at Finite temperature

We[1] study the ferromagnetic Kondo model with classical corespins via unbiased Monte-Carlo simulations and derive a simplified model for the treatment of the corespins at any temperature. Our simplified model captures the main aspects of the Kondo model and can easily be evaluated both numerically and analytically. It provides a better qualitative understanding of the physical features of the Kondo model and rationalizes the Monte-Carlo results including the spectral density $A_k(\omega)$ of a 1D chain with nearest neighbor Coulomb repulsion. By calculating the specific heat and the susceptibility of systems up to size 16^3, we determine the Curie temperature of the 3D one-orbital double-exchange model, which agrees with experimental values.

6.1 Introduction

Since full many-body calculations for a realistic model, including all degrees of freedom, are not possible yet, several approximate studies of simplified models have been performed in order to unravel individual pieces of the rich phase diagram of the manganites. The electronic degrees of freedom are generally treated by a Kondo lattice model, which in the strong Hund coupling limit is commonly referred to as the double-exchange (DE) model, a term introduced by Zener [39]. In addition, the correlation of the itinerant e_g electrons is well described by a nearest neighbor (n.n.) Coulomb interaction. The on-site Hubbard term merely renormalizes the already strong Hund coupling. For the Kondo model with quantum spins, it is still impossible to derive rigorous numerical and analytical results. If the S=3/2 corespins are treated classically, however, the model can be treated by unbiased Monte Carlo techniques. The impact of

[1] This chapter has been accepted for publication in Phys. Rev. B as Ref. [9].

quantum spins on the electronic properties has been studied in Ref. [16, 53, 54]. It appears that quantum effects are important for S=1/2 corespins or at $T = 0$. For finite temperature and S=3/2, classical spins present a reasonable approximation.

Elaborate Monte Carlo (MC) simulations for the FM Kondo model with classical t_{2g} corespins have been performed by Dagotto *et al.* [22, 41, 42], Yi *et al.* [55], and by Furukawa *et al.* [40, 56]. Static and dynamical properties of the model have been determined. These studies revealed features which have been interpreted as signatures of phase-separation (PS). PS has also been reported [57] from computations based on a dynamical mean field treatment of the DE model at $T = 0$. A phase diagram and critical exponents of the DE model have been determined with a Hybrid MC algorithm [58, 59].

In the manganites, the Hund coupling J_H is much stronger than the kinetic energy. Consequently, configurations are very unlikely in which the electronic spin is antiparallel to the local corespin. It is therefore common practise to use $J_H = \infty$ and to ignore antiparallel spin arrangements altogether. This approximation yields reasonable results in the ferromagnetic regime. Close to half-filling, however, a finite ferromagnetic Hund coupling even enhances the antiferromagnetic ordering of the corespins. In a previous paper [8], we have proposed an effective spinless fermion (ESF) model that takes effects of antiparallel $t_{2g} - e_g$ spin configurations into account via virtual excitations. It has been demonstrated that the results of the ESF model are in excellent agreement with those of the original Kondo model even for moderate values of J_H.

In Ref. [8] we also introduced the uniform hopping approach (UHA), which replaces the influence of the random corespins on the e_g electron dynamics by an effective uniform hopping process. In that work, the hopping parameter was determined by minimization of the ground-state energy. Essential physical features of the original model could be described even quantitatively by UHA, while the configuration space, and hence the numerical effort, was reduced by several orders of magnitude. Besides the numerical advantage, UHA also allows the derivation of analytical results in some limiting cases.

In the present paper we extend the UHA to finite temperature. Thermal fluctuations of the corespins are mapped to fluctuations of the uniform hopping parameter. In order to include entropy effects correctly, we have to determine the density $\Gamma(u)$ of corespin states for a given hopping parameter u. The reliability of the finite-temperature UHA is scrutinized by a detailed comparison of the results for various properties of the one-orbital DE model with unbiased MC data.

So far, in most MC simulations the Coulomb interaction of the e_g electrons has been neglected due to its additional computational burden. It should, however, have an important impact, particularly on phase separation. Moreover, at quarter filling the n.n. repulsion leads to the charge ordering (CO) phase. We have performed MC simulations for the Kondo model including a Hubbard-like

Coulomb interaction. In these simulations, for each classical corespin configuration, the electronic degrees of freedom are treated by Lanczos exact diagonalization. We find that also in this case UHA yields reliable results while reducing the computational complexity by orders of magnitude. An excerpt of the results is given here, while a thorough discussion will be provided elsewhere.

Also starting from an UHA-type of Hamiltonian, Millis *et al.* [60] claim that the bare DE model cannot even explain the right order of magnitude of the Curie temperatures of the manganites. This claim is, however, based on uncontrolled additional approximations. We find that a more rigorous evaluation of UHA for a one-orbital DE model and large 3D systems yields a Curie temperature which is indeed close to the experimental values. Our results for the DE model are in accord with the Hybrid MC result [59] and with other estimates [40, 42, 61].

This paper is organized as follows. In Sec. 6.2 the model Hamiltonian is presented and particularities of the MC simulation are outlined. The uniform hopping approach is discussed in Sec. 6.3. One-dimensional applications are given in Sec. 6.4 and compared with MC data. The impact of Coulomb correlations on the spectral density is discussed. In Sec. 6.5 the UHA is used to calculate the phase diagram of the DE model in 3D. The key results of the paper are summarized in Sec. 6.6.

6.2 Model Hamiltonian and unbiased Monte Carlo

In this paper, we will concentrate on properties of the itinerant e_g electrons interacting with the local t_{2g} corespins. It is commonly believed that the electronic degrees of freedom are well described by a multi-orbital Kondo lattice model

$$\hat{H} = - \sum_{\substack{ij\alpha\beta \\ \sigma}} t_{i\alpha,j\beta}\, a^{\dagger}_{i\alpha\sigma}\, a_{j\beta\sigma} - J_H \sum_{i\alpha} \vec{\sigma}_{i\alpha} \vec{S}_i + \sum_{ij\alpha\beta} V_{i\alpha,j\beta}\, \hat{n}_{i\alpha} \hat{n}_{j\beta} + J' \sum_{<ij>} \mathbf{S}_i \cdot \mathbf{S}_j \ . \tag{6.1}$$

As proposed by de Gennes [62], Dagotto *et al.* [22, 1] and Furukawa [40], the t_{2g} spins $\mathbf{S}_i$ are treated classically, which is equivalent to the limit $S \to \infty$. The spin degrees of freedom are thus replaced by unit vectors $\mathbf{S}_i$, parameterized by polar and azimuthal angles θ_i and ϕ_i, respectively. The magnitude of both corespins and e_g-spins is absorbed into the exchange couplings.

Equation (6.1) consists of a kinetic term for the itinerant e_g electrons with transfer integrals $t_{i\alpha,j\beta}$, where $i(j)$ are site indices, $\alpha(\beta)$ orbital indices, and $\sigma(\sigma')$ spin indices. The transfer integrals, which are restricted to n.n. sites, are given as matrices in the orbital indices $\alpha, \beta = 1(2)$ for x^2-y^2 ($3z^2-r^2$) orbitals (see e.g. Ref. [1])

$$t_{i,i+\hat{z}} \ = \ t \begin{pmatrix} 0 & 0 \\ 0 & 1 \end{pmatrix}, \ t_{i,i+\hat{x}/\hat{y}} = t \begin{pmatrix} \frac{3}{4} & \mp\frac{\sqrt{3}}{4} \\ \mp\frac{\sqrt{3}}{4} & \frac{1}{4} \end{pmatrix} . \tag{6.2}$$

The overall hopping strength is t, which will be used as unit of energy, by setting $t = 1$. The operators $a^\dagger_{i\alpha\sigma}(a_{i\alpha\sigma})$ create (annihilate) e_g electrons at site x_i in orbital α with spin σ. The second term of the Hamiltonian describes the Hund coupling with exchange integral J_H, where $\vec{\sigma}_{i\alpha}$ stands for the spin of the electron at site i in orbital α. The spin-resolved occupation number operator is denoted by $\hat{n}_{i\alpha\sigma}$. The third term describes a Coulomb repulsion, with $\hat{n}_{i\alpha}$ being the spin-integrated density operator. The local Hubbard interaction is excluded from the sum, i.e. $V_{i\alpha,i\alpha} = 0$, as it effectively merely modifies the Hund coupling J_H. Finally, Eq. (6.1) contains a superexchange term. The value of the exchange coupling is $J' \approx 0.02$ [1], accounting for the weak antiferromagnetic coupling of the t_{2g} electrons.

For strong Hund coupling $J_H \gg t$, the electronic density of states (DOS) essentially consists of two sub-bands, a lower- and an upper 'Kondo band', split by approximately $2J_H$. In the lower band the itinerant e_g electrons move such that their spins are predominantly parallel to the t_{2g} corespins, while the opposite is true for the upper band [46]. Throughout this paper, the electronic density n (number of electrons per orbital) will be restricted to $0 \leq n \leq 1$, i.e. only the lower Kondo band is involved.

6.2.1 Effective Spinless Fermions

It is expedient to use the individual t_{2g} spin directions $\vec{S}_i$ as the local quantization axes for the spin of the itinerant e_g electrons at the respective sites. This representation is particularly useful for the $J_H \to \infty$ limit, but also for the projection technique, which takes into account virtual processes for finite Hund coupling. The transformation in the electronic spin is described by a local unitary 2×2 matrix $U(S_i)$ with

$$\vec{a}_{i\alpha} = U(S_i)\, \vec{c}_{i\alpha} \qquad \vec{c}_{i\alpha} = U^\dagger(S_i)\, \vec{a}_{i\alpha}\ , \tag{6.3}$$

where $\vec{a}_{i\alpha}$ is a column vector with entries $a_{i\alpha\uparrow}$ and $a_{i\alpha\downarrow}$, respectively. The transformed annihilation operators in local quantization are represented by $\vec{c}_{i\alpha}$. For the creation operators we have

$$\vec{a}^\dagger_{i\alpha} = \vec{c}^\dagger_{i\alpha} U^\dagger(S_i)\ , \qquad \vec{c}^\dagger_{i\alpha} = \vec{a}^\dagger_{i\alpha} U(S_i)\ . \tag{6.4}$$

The unitary matrix $U(S_i)$ depends upon S_i and is chosen such that it diagonalizes the individual contributions to the Kondo exchange

$$\vec{\sigma}_{i\alpha}\vec{S}_i \equiv \vec{a}^\dagger_{i\alpha}\ (\vec{\Sigma}\vec{S}_i)\ \vec{a}_{i\alpha}\ = \vec{c}^\dagger_{i\alpha}\Big(U^\dagger(S_i)\ (\vec{\Sigma}\vec{S}_i)\ U(S_i)\Big)\vec{c}_{i\alpha}\ , \tag{6.5}$$

with $\vec{\Sigma}$ being the vector of Pauli matrices. The eigenvalues of of $(\vec{\Sigma}\vec{S}_i)$ are ± 1 and the matrix of eigenvectors is given by

$$U(S_i) = \begin{pmatrix} c_i & s_i\ \mathrm{e}^{-i\phi_i} \\ s_i\ \mathrm{e}^{i\phi_i} & -c_i \end{pmatrix}\ , \tag{6.6}$$

with the abbreviations $c_j = \cos(\theta_j/2)$ and $s_j = \sin(\theta_j/2)$ and the restriction $0 \le \theta_j \le \pi$. The Kondo exchange term in Eq. (6.5) in the new representation reads

$$\vec{\sigma}_{i\alpha}\vec{S}_i = \hat{n}_{i\alpha\uparrow} - \hat{n}_{i\alpha\downarrow} \; . \tag{6.7}$$

The spin-integrated density operators $\hat{n}_{i\alpha}$ are unaffected by the unitary transformation. The entire Kondo Hamiltonian becomes

$$\hat{H} = -\sum_{\substack{ij\alpha\beta \\ \sigma\sigma'}} t_{i\alpha,j\beta}^{\sigma,\sigma'} \, c_{i\alpha\sigma}^{\dagger} \, c_{j\beta\sigma'} + 2J_H \sum_{i\alpha} \hat{n}_{i\alpha\downarrow} + \sum_{ij\alpha\beta} V_{i\alpha,j\beta} \, \hat{n}_{i\alpha}\hat{n}_{j\beta} + J' \sum_{<ij>} \mathbf{S}_i \cdot \mathbf{S}_j \; . \tag{6.8}$$

We have added an additional term $\hat{H}_c = J_H\hat{N}$ proportional to the e_g-electron number N, equivalent to a trivial shift of the chemical potential.

The prize to be paid for the simple structure of the Hund term is that the modified hopping integrals $t_{i\alpha,j\beta}^{\sigma,\sigma'}$ now depend upon the t_{2g} corespins:

$$t_{i\alpha,j\beta}^{\sigma,\sigma'} \; = \; t_{i\alpha,j\beta} \left(U^{\dagger}(S_i) U(S_j) \right)_{\sigma,\sigma'} \; = \; t_{i\alpha,j\beta} \, u_{ij}^{\sigma,\sigma'} \; . \tag{6.9}$$

The relative orientation of the t_{2g} corespins at site i and j enters via

$$\begin{aligned} u_{i,j}^{\sigma,\sigma}(\mathcal{S}) &= c_i c_j + s_i s_j \, \mathrm{e}^{i\sigma(\phi_j - \phi_i)} \qquad\quad = \cos(\vartheta_{ij}/2) \, \mathrm{e}^{i\psi_{ij}} \\ u_{i,j}^{\sigma,-\sigma}(\mathcal{S}) &= \sigma(c_i s_j \, \mathrm{e}^{-i\sigma\phi_j} - c_j s_i \, \mathrm{e}^{-i\sigma\phi_i}) = \sin(\vartheta_{ij}/2) \, \mathrm{e}^{i\chi_{ij}} \end{aligned} \; . \tag{6.10}$$

These factors depend on the relative angle ϑ_{ij} of corespins $\mathbf{S}_i$ and $\mathbf{S}_j$ and on some complex phases ψ_{ij} and χ_{ij}. It should be noticed that the modified hopping part of the Hamiltonian is still Hermitian, because $u_{i,j}^{\sigma,\sigma'} = \left(u_{j,i}^{\sigma',\sigma}\right)^*$.

The advantage of the local quantization is, as described in Ref. [8], that the energetically unfavorable states with e_g electrons antiparallel to the local t_{2g} corespins can be integrated out. This leads to the effective spinless fermion model

$$\begin{aligned} \hat{H}_p = &- \sum_{i,j,\alpha,\beta} t_{i\alpha,j\beta}^{\uparrow\uparrow} \, c_{i\alpha}^{\dagger} \, c_{j\beta} - \sum_{i,j,\alpha,\beta,\alpha'} \frac{t_{i\alpha',j\beta}^{\uparrow\downarrow} \, t_{j\beta,i\alpha}^{\downarrow\uparrow}}{2J_H} \, c_{i\alpha'}^{\dagger} c_{i\alpha} \\ &+ \sum_{ij\alpha\beta} V_{i\alpha,j\beta} \, \hat{n}_{i\alpha}\hat{n}_{j\beta} + J' \sum_{<ij>} \mathbf{S}_i \cdot \mathbf{S}_j \; . \end{aligned} \tag{6.11}$$

The spinless fermion operators correspond to spin-up electrons (relative to the *local* corespin-orientation) only. The spin index has therefore been omitted. With respect to a *global* spin-quantization axis, the ESF model (6.11) still contains contributions from both spin-up and spin-down electrons. The V-dependent contributions in the energy denominator have been ignored, since $|V_{i\alpha,j\beta}| \ll |J_H|$. In principle, the effective Hamiltonian also contains "three-site" hopping processes. It has been shown [8] that the three-site term has negligible impact, and it has been ignored here.

Since each eigenvector can have an arbitrary phase, the unitary matrix in Eq. (6.6) is not unique. This implies that

$$U(S_i) = \begin{pmatrix} c_i & s_i \, \mathrm{e}^{-i\phi_i} \\ s_i \, \mathrm{e}^{i\phi_i} & -c_i \end{pmatrix} \begin{pmatrix} \mathrm{e}^{i\alpha(i)} & 0 \\ 0 & \mathrm{e}^{i\beta(j)} \end{pmatrix}$$

also diagonalizes the Kondo term. The additional phase factors modify the hopping integrals of the spin-up channel as

$$\begin{aligned} u_{i,j}^{\uparrow\uparrow}(\mathcal{S}) &= \left(c_i c_j + s_i s_j \; e^{i(\phi_j - \phi_i)} \right) \mathrm{e}^{i(\alpha(j)-\alpha(i))} \\ &= \cos(\vartheta_{ij}/2) \; \mathrm{e}^{i(\psi_{ij}+\alpha(j)-\alpha(i))} \; . \end{aligned} \tag{6.12}$$

Consequently, in the one-dimensional case and with open boundaries, we can choose the local phase factors such that the n.n. hopping integrals are simply given by the real numbers $\cos(\vartheta_{ij}/2)$.

6.2.2 Grand Canonical Treatment

Our model contains classical (corespins) and quantum mechanical (e_g-electrons) degrees of freedom. The appropriate way to cope with this situation in statistical mechanics is to define the grand canonical partition function as

$$\begin{aligned} \mathcal{Z} &= \int \mathcal{D}[\mathcal{S}] \quad \mathrm{tr}_c \, \mathrm{e}^{-\beta(\hat{H}(\theta,\phi)-\mu\hat{N})} \\ \int \mathcal{D}[\mathcal{S}] \; &= \prod_{i=1}^{L} \left(\int_0^{\pi} d\theta_i \sin\theta_i \int_0^{2\pi} d\phi_i \right) , \end{aligned} \tag{6.13}$$

where tr_c indicates the trace over fermionic degrees of freedom at inverse temperature β, $\hat{N}$ is the operator for the total number of e_g electrons, L is the number of lattice sites, and μ stands for the chemical potential. Upon integrating out the fermionic degrees of freedom, we obtain the statistical weight of a corespin configuration $\mathcal{S}$

$$w(\mathcal{S}) = \frac{\mathrm{tr}_c \, \mathrm{e}^{-\beta(\hat{H}(\mathcal{S})-\mu\hat{N})}}{\mathcal{Z}} \; . \tag{6.14}$$

Equation (6.13) is the starting point of Monte Carlo simulations for the Kondo model [22] where the sum over the classical spins is performed via importance sampling. The spin configurations $\mathcal{S}$ enter the Markov chain according to the weight factor $w(\mathcal{S})$ that is computed via exact diagonalization of the corresponding Hamiltonian in Eq. (6.8). In the 1D case we have performed MC simulations in which spins in domains of random lengths were rotated. We have performed MC runs with 1000 measurements. The skip between subsequent measurements was chosen to be some hundreds of lattice sweeps reducing autocorrelations to a negligible level.

Apart from quantities that can be derived directly from the partition function $\mathcal{Z}$, we will also be interested in dynamical observables, notably in the one-particle retarded Green's function $\ll a_{i\alpha\sigma}; a^{\dagger}_{j\beta\sigma} \gg_{\omega}$ in global spin-quantization. This function follows from

$$\ll a_{i\alpha\sigma}; a^{\dagger}_{j\beta\sigma} \gg_{\omega} = \int \mathcal{D}[\mathcal{S}] \; w(\mathcal{S}) \; \ll a_{i\alpha\sigma}; a^{\dagger}_{j\beta\sigma} \gg^{\mathcal{S}}_{\omega} \; . \tag{6.15}$$

The one-particle Green's function $\ll a_{i\alpha\sigma}; a^{\dagger}_{j\beta\sigma} \gg^{\mathcal{S}}_{\omega}$, corresponding to a particular corespin configuration $\mathcal{S}$, is determined from the Green's function in local spin-quantization by employing Eq. (6.3) and Eq. (6.4)

$$\ll a_{i\alpha\sigma}; a^{\dagger}_{j\beta\sigma} \gg^{\mathcal{S}}_{\omega} = U(S_i)_{\sigma\uparrow} U^{*}(S_j)_{\sigma\uparrow} \ll c_{i\alpha}; c^{\dagger}_{j\beta} \gg^{\mathcal{S}}_{\omega} \ . \tag{6.16}$$

To arrive at Eq. (6.16), we used the fact that in *local* quantization only the spin-up channel contributes to $\ll c_{i\alpha\sigma}; c^{\dagger}_{j\beta\sigma'} \gg^{\mathcal{S}}_{\omega}$, *i.e.* $\sigma = \sigma' = \uparrow$. The spin-down channel has structures corresponding to the upper Kondo band in which we are not interested here. In *global* quantization, both spin directions contribute. The spin-integrated Green's function reads

$$\sum_{\sigma} \ll a_{i\alpha\sigma}; a^{\dagger}_{j\beta\sigma} \gg^{\mathcal{S}}_{\omega} = u^{\uparrow\uparrow}_{ji}(\mathcal{S}) \ll c_{i\alpha}; c^{\dagger}_{j\beta} \gg^{\mathcal{S}}_{\omega} \ . \tag{6.17}$$

The unbiased Monte-Carlo result for the spin-integrated one-particle Green's function is therefore determined from

$$\sum_{\sigma} \ll a_{i\alpha\sigma}; a^{\dagger}_{j\beta\sigma} \gg_{\omega} = \int \mathcal{D}[\mathcal{S}] \; w(\mathcal{S}) u^{\uparrow\uparrow}_{ji}(\mathcal{S}) \ll c_{i\alpha}; c^{\dagger}_{j\beta} \gg^{\mathcal{S}}_{\omega} \ . \tag{6.18}$$

We note that the one-particle density of states (DOS) is independent of the choice of the spin-quantization, because it can be determined from diagonal Green's functions in real space.

6.3 Uniform Hopping Approach

The impact of the DE mechanism on the electronic kinetic energy can be mimicked by an *average* hopping amplitude [62]. In a previous paper [8] we introduced what we called the "uniform hopping approach" (UHA). It gave strikingly good results for ground state properties. The idea behind UHA is to replace the terms $u^{\uparrow\uparrow}_{ij}$ in the hopping amplitude, Eq. (6.9), which correspond to $\cos(\vartheta_{ij}/2)$ as discussed before, by a uniform value u. In Ref. [8] the optimal UHA parameter u was determined by minimizing the ground state energy. Here we will extend this approach to finite temperatures by taking entropic effects into account.

In order to introduce the finite-temperature UHA, we proceed as follows: For a given corespin configuration characterized by the set of angles $\{\theta_i, \phi_i\}$, we define the average u-value

$$u(\mathcal{S}) = \frac{1}{N_p} \sum_{\langle ij \rangle} u^{\uparrow\uparrow}_{ij}(\mathcal{S}) \ .$$

Here N_p is the number of n.n. pairs $\langle ij \rangle$. We now replace the individual factors $u^{\uparrow\uparrow}_{ij}$ in Eq. (6.13) by $u(\mathcal{S})$. Besides $u^{\uparrow\uparrow}_{ij}$ the Hamiltonian depends on $|u^{\sigma,-\sigma}_{ij}|^2$ and on $\mathbf{S}_i \cdot \mathbf{S}_j$, which correspond to $\sin^2(\vartheta_{ij}/2)$ and $\cos\vartheta_{ij}$, respectively. As

a further approximation (see below), these terms are respectively replaced by $1-u^2(\mathcal{S})$ and $2\,u^2(\mathcal{S})-1$.

The introduction of UHA leads to the partition function

$$\begin{aligned}\mathcal{Z} &= \int \mathcal{D}[\mathcal{S}] \int_0^1 du\,\delta(u-u(\mathcal{S}))\ \mathrm{tr}_c\, e^{-\beta(\hat{H}(u)-\mu\hat{N})} \\ &=: \int_0^1 du\,\Gamma_{N_p}(u)\,\mathrm{e}^{-\beta\,\Omega(u)}\ .\end{aligned} \tag{6.19}$$

The integrand can be interpreted as the (non-normalized) thermal probability density for the uniform hopping parameter u,

$$p(u\,|\,\beta) = \Gamma_{N_p}(u)\,\mathrm{e}^{-\beta\,\Omega(u)}\ . \tag{6.20}$$

It consists of the density of corespin states $\Gamma_{N_p}(u)$ and the Boltzmann factor. The former corresponds to a density of states and is given by

$$\Gamma_{N_p}(u) = \int \mathcal{D}[\mathcal{S}]\ \delta(u-u(\mathcal{S}))\ . \tag{6.21}$$

It accounts for the number of different corespin configurations (multiplicity) that give rise to the same uniform hopping amplitude u. We note that since angles $\vartheta_{ij}/2$ enter into Eq. (6.10), this is different from the density of states of the classical Heisenberg model. The grand potential $\Omega(u)$

$$-\beta\,\Omega(u) = \log\ \mathrm{tr}_c\,\mathrm{e}^{-\beta(\hat{H}(u)-\mu\hat{N})} \tag{6.22}$$

is obtained from the fermionic trace of the homogeneous version of the Hamiltonian of Eq. (6.11), which reads

$$\begin{aligned}\hat{H}_p(u) = &-u\sum_{\substack{<i,j>\\ \alpha,\beta}} t_{i\alpha,j\beta}\,c^\dagger_{i\alpha}\,c_{j\beta} - (1-u^2)\sum_{\substack{<i,j>\\ \alpha,\beta,\alpha'}} \frac{t_{i\alpha',j\beta}\,t_{j\beta,i\alpha}}{2J_H}\,c^\dagger_{i\alpha'}c_{i\alpha} \\ &+ \sum_{i,j,\alpha,\beta} V_{i\alpha,j\beta}\,\hat{n}_{i\alpha}\hat{n}_{j\beta} + J' N_p\,(2u^2-1)\ .\end{aligned} \tag{6.23}$$

The uniform hopping approach presents an enormous simplification of the original problem. Firstly, the evaluation of the fermionic trace simplifies considerably; for non-interacting electrons ($V=0$) it can even be computed analytically. Secondly, the high dimensional configuration space of the corespins shrinks to a unit interval. Once the density of corespin states $\Gamma_{N_p}(u)$ has been determined, the integration over the corespin states can be carried out.

The thermal probability density $p(u\,|\,\beta)$ in Eq. (6.20) contains two competing factors. The density of corespin states $\Gamma_{N_p}(u)$ peaks near $u=2/3$ and decreases algebraically to zero as u approaches the bounds of the unit interval. A tendency towards ferromagnetic (antiferromagnetic) order is reflected by an exponential increase of the Boltzmann factor towards $u=1$ ($u=0$). This

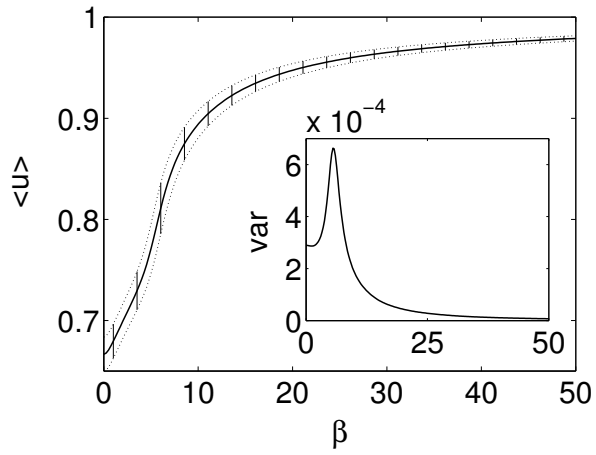

Figure 6.1: Mean $\langle u \rangle$ (solid line) and standard deviation (dashed line) of $p(u|\beta)$ versus inverse temperature for a 4^3 cluster at quarter filling. The β-dependence of the variance is depicted in the inset.

factor becomes increasingly important with decreasing temperature. In the ferromagnetic case, the combined distribution peaks, depending on the value of β, somewhere between 2/3 and 1 (see Fig. 6.1 for an illustration in 3D). With increasing β the peak shifts towards $u = 1$.

In summary, the configuration space of the corespins is reduced to the one-parametric space of the UHA parameter u. This simplification is based on the assumption that, as far as the Boltzmann factor is concerned, the effect of the corespins on the electrons can be replaced by a mean effective hopping. Fluctuations of the corespins are allowed for by the density $\Gamma_{N_p}(u)$ and by fluctuations of the UHA parameter, resulting in a finite lifetime of the quasiparticles even in the FM phase, and in a finite bandwidth even in the AFM phase. The density $\Gamma_{N_p}(u)$ takes care of the correct inclusion of the corespin entropy, which will become crucial in the ensuing discussion.

Validity of the additional approximation

In order to assess the additional approximation introduced by the substitution of the terms $\langle \sin^2(\vartheta/2) \rangle \approx 1 - \langle \cos \vartheta/2 \rangle^2 \equiv 1 - u^2$ and $\langle \cos \vartheta \rangle \approx 2 \langle \cos \vartheta/2 \rangle^2 - 1 \equiv 2u^2 - 1$, a Monte Carlo simulation with random spins on a 16^3 simple cubic (sc) lattice has been performed. For each spin configuration, the mean values of the functions $\cos(\vartheta/2)$, $\cos(\vartheta)$, and $\sin^2(\vartheta/2)$ have been computed. The resulting scatter plot is depicted in Fig. 6.2. Astonishingly, the data follow a unique curve and moreover they are fairly well described by the approximation employed.

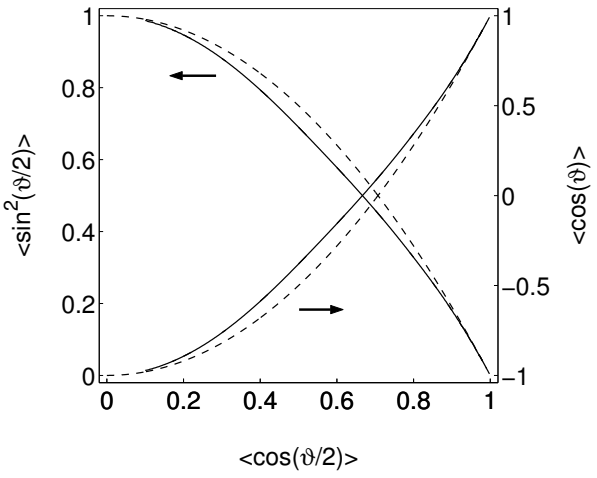

Figure 6.2: Average $\langle \sin^2(\vartheta/2) \rangle$ and average $\langle \cos\vartheta \rangle$ as a function of the average hopping $u = \langle \cos\vartheta/2 \rangle$ for a 16^3 cluster. The dashed lines show the results of the 'naive' approximation explained in the text.

6.4 UHA vs Monte Carlo in 1D

In this section we scrutinize the uniform hopping approach by a detailed comparison of its results with MC data obtained for the original Hamiltonian Eq. (6.11). Since the UHA affects only the treatment of the corespins, we will restrict our attention to a one-orbital model and neglect the degeneracy of the e_g orbitals. In this case, the Hamiltonian (6.23) simplifies to

$$\begin{aligned} \hat{H}_p(u) = &- u \sum_{<ij>} c_i^\dagger c_j - \frac{1-u^2}{2J_H} \sum_i z_i \, n_i + V \sum_{<ij>} n_i \, n_j \\ &+ J' N_p \, (2u^2 - 1) \, , \end{aligned} \tag{6.24}$$

where z_i denotes the number of nearest neighbors of site i.

For a one-dimensional chain with open boundary condition, $\Gamma_{N_p}(u)$ can be calculated exactly. For a two-site lattice we find $\Gamma_1(u) = 2u \, \chi_{[0,1]}(u)$, where $\chi_B(u)$ denotes the characteristic function of the set B. Since the relative angles of the $N_p = L-1$ nearest-neighbor pairs of a chain of length L are independent, $\Gamma_{N_p}(u)$ reduces to a (N_p-1)-fold convolution of $\Gamma_1(u)$. Therefore, $\Gamma_{N_p}(u)$ is piecewise polynomial and can be evaluated numerically. It can be approximated by a Gaussian, which is not surprising because the central limit theorem applies. In combination with the Boltzmann factor, however, a Gaussian approximation is not good enough because the Boltzmann factor amplifies the tails of the distribution.

6.4.1 Energy distribution

In this subsection we will compare UHA with MC results for the DE model with $V = J' = 0,\ J_H = \infty$ for a one dimensional system with one e_g orbital per site. The Hamiltonian of Eq. (6.24) reduces to a one-particle tight-binding Hamiltonian

$$\hat{H}_p(u) = -u \sum_{<i,j>} c_i^\dagger c_j \ , \tag{6.25}$$

with only kinetic energy. The hopping integral u is the only remnant of the interaction with the t_{2g} corespins. The grand potential reads

$$\begin{aligned} -\beta\Omega(u) &= \sum_k \log(1 + \mathrm{e}^{-\beta(\epsilon_k - \mu)}) \\ &= \int dE\, \rho_L(E)\ \log(1 + \mathrm{e}^{-\beta(E-\mu)}) \ . \end{aligned} \tag{6.26}$$

where the one-particle eigenvalues $\epsilon_k = -2u\cos k$ depend on u and $\rho_L(E)$ denotes the tight-binding DOS of the L-site lattice. $\Omega(u)$ can now be computed easily, and along with exact results for $\Gamma_{N_p}(u)$ we have access to the partition function and thermal quantities such as the kinetic energy. In Fig. 6.3, the results for the kinetic energy are compared with those of unbiased MC simulations. One finds an impressive agreement between the two results. The energies are reproduced within the error bars for all values of β. At higher temperatures this agreement is not obvious at all, because the corespins are strongly fluctuating. The impact of the fluctuations seems to be well described by the UHA.

For a canonical ensemble at sufficiently low temperatures (canonical low-T approximation) one can derive an analytical result for UHA. To do so, the function $\Omega(u)$ is replaced by the ground state energy of the tight-binding Hamiltonian which we write as

$$\Omega(u) = u\ E_k \ , \tag{6.27}$$

with a factor E_k (total energy of a tight-binding system with unit hopping amplitude) independent of u. The canonical partition function then reads

$$Z = \int \mathcal{D}[\mathcal{S}]\ \ \mathrm{e}^{-\beta u\, E_k} \ .$$

Since u can be expressed as the average $u = \frac{1}{N_p} \sum \cos(\vartheta_{ij}/2)$, the exponential function can be written as a product of factors containing only n.n. spins. In the case of a 1D chain with open boundary conditions or for a Bethe lattice, the relative angles of neighboring spins can thus be integrated independently. Consequently, the partition function factorizes and (up to some unimportant constant factors) can be transformed to

$$Z = \left(\int_0^1 du\ \Gamma_1(u)\ \mathrm{e}^{-u\zeta} \right)^{N_p} = \left(2\, \frac{1 - \mathrm{e}^{-\zeta}(1+\zeta)}{\zeta^2} \right)^{N_p},$$

with $\zeta = \beta\, E_k/N_p$. By differentiation with respect to β, we obtain the kinetic energy

$$E_{\rm kin} = E_k\, \frac{\zeta^2 + 2\,\zeta + 2 - 2\,{\rm e}^{\zeta}}{\zeta(\zeta + 1 - {\rm e}^{\zeta})}\ .$$

This result is shown as a dashed line in Fig. 6.3. The comparison with MC

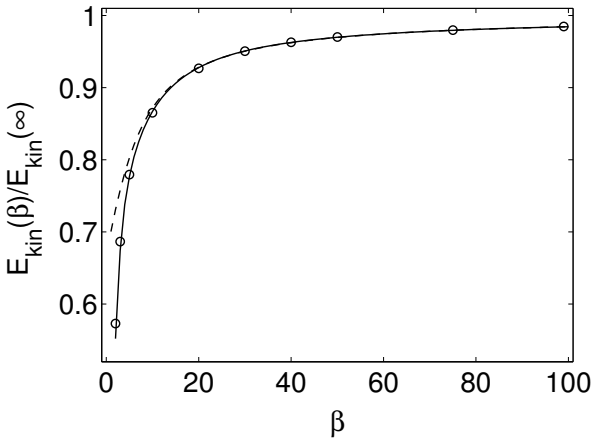

Figure 6.3: Kinetic energy versus β for a 20 site Kondo chain with $J_H = \infty$, $J' = V = 0$ and $N = 10$. The statistical errors of the Monte Carlo data (circles) are smaller than the marker size. The MC data are compared with results of UHA (solid line) and the canonical low-T approximations (dashed line).

results shows increasingly close agreement for $\beta \gtrsim 10$.

The above considerations show that UHA on average correctly describes the kinetic processes. In order to give a more critical assessment of UHA, we study the fluctuations of the kinetic energy. It should be kept in mind that the motivation of UHA is to describe the mean energy correctly. It is thus not a priori obvious whether UHA also properly reflects its fluctuations. In UHA the fluctuations of the kinetic energy are exclusively due to fluctuations of the uniform hopping parameter u, that in turn is related to the relative n.n. angles of corespins. In the full model, however, the relative n.n. angles fluctuate locally.

By sampling the contributions to the kinetic energy in a MC simulation including local fluctuations, we obtain histograms for the full model. They can be compared with the statistical distribution of the kinetic energy corresponding to the UHA density $\Gamma_{N_p}(u)\,{\rm e}^{-\beta\Omega(u)}$. The result of this comparison is depicted in Fig. 6.4. We find perfect agreement between MC and UHA results, revealing a non-trivial justification of UHA.

6.4.2 Spectral function and Coulomb Correlations

We will now comment on the influence of the n.n. Hubbard interaction on the spectral density and compare MC with UHA results. A thorough discussion

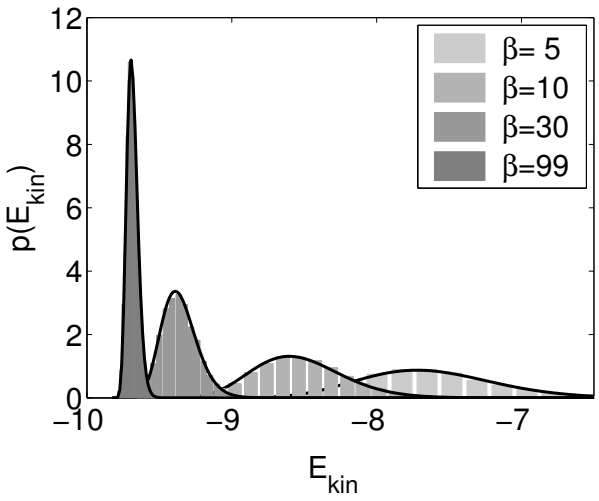

Figure 6.4: Probability density for the kinetic energy of a 16 site DE chain at half-filling for various values of β. The histograms are taken from unbiased Monte Carlo data. Solid lines represent UHA results.

of correlation effects in conjunction with the Kondo model will be given elsewhere [10]. We have studied a 12 site chain with open boundaries at half filling of the effective spinless model, i.e. quarter filling of the original Kondo model. In this case the implementation of the ESF model reduces the dimension of the Lanczos basis from $\binom{2L}{N} = 134\,596$ to $\binom{L}{N} = 924$. Additionally UHA replaces the sampling of spin configurations with a simple scan in the UHA parameter u (several 100 000 spin configurations in MC versus approx. 20 u-values in the relevant u-range $[0.8\,,\,1.0]$ in UHA).

Without Hubbard interaction, the system is ferromagnetic due to the DE mechanism. The spectral density, calculated by MC and depicted in Fig. 12 of Ref. [8], is that of a tight-binding model [41]. The peaks are slightly broadened due to spin fluctuations. In UHA, through the variation of the uniform hopping amplitude u, we obtain a superposition of tight-binding bands that combine to a broadened tight-binding band. For the parameters $L = 20$, $J_H = 6$ and $J' = 0.02$ and at $\beta = 50$, the average uniform hopping amplitude $\langle u \rangle$ is found to be $\langle u \rangle \simeq 0.953$. This yields a band width W of $W \simeq 3.8$ which agrees with what we have found in MC simulations.

We now include the n.n. Hubbard term with $V = 2$ in the ESF model Eq. (6.11), or alternatively in the UHA Hamiltonian in Eq. (6.23). The Monte Carlo data are obtained by resorting to a Lanczos exact diagonalization scheme for each corespin configuration. The fermionic trace is then evaluated by summing over enough lowest eigenstates, such that convergence is ensured. Details will be given elsewhere [10].

In UHA, a $t-V$ model has to be diagonalized. The Lanczos diagonalization for this model is not really faster than the diagonalization of the original model,

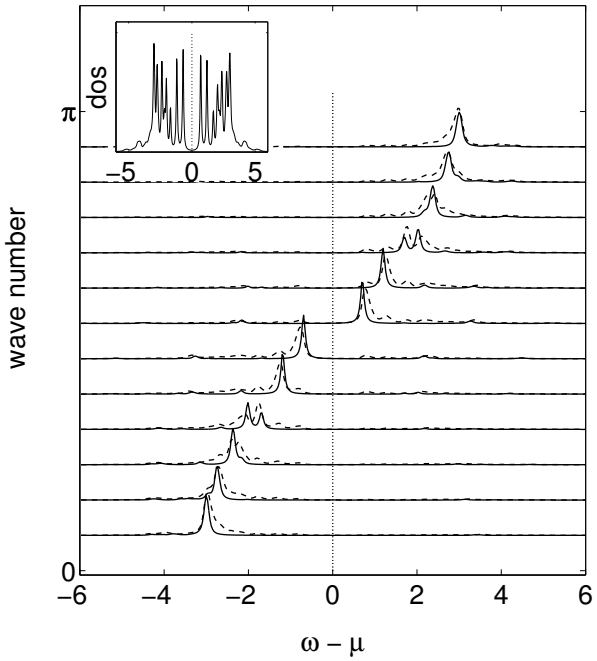

Figure 6.5: Spectral density of a 12-site Kondo chain at quarter filling ($N = 6$) with $V = 2$, $J' = 0.02$, $J_H = 6$, $\beta = 50$. Data of the Monte Carlo – Lanczos hybrid algorithm (dashed lines) are compared with UHA results (solid line). The inset displays the DOS obtained from MC simulations.

but the configuration space is drastically reduced, as only the parameter u has to be sampled within the unit interval $u \in [0, 1]$.

Figure 6.5 shows the spectral density derived by both approaches. The electronic correlation has important impact on the spectral density. A gap appears in the middle of the original Brillouin zone at $k = \pi/2$, indicating the doubling of the unit cell due to charge ordering. In addition, the spectra exhibit more structure than just a simple quasi particle peak.

This result is neither new nor surprising. The point we want to make here is that UHA works well also for correlated electrons, indicating that it can reliably be employed to study more sophisticated and more realistic models for the manganites, e.g. by including correlation effects, phononic degrees of freedom, and more orbital degrees of freedom.

6.5 FM phase transition in 3D

We now apply UHA to a sc crystal and determine the Curie temperature for the bare one-orbital DE model. The crucial difference between the 1D and the 3D geometry is that in the latter the relative angles of n.n. corespin-pairs are in general correlated. Therefore the correct density $\Gamma_{N_p}(u)$ is no longer a convolution of the density $\Gamma_1(u)$ of a single spin-pair.

6.5.1 Determination of $\Gamma_{N_p}(u)$

In order to determine $\Gamma_{N_p}(u)$ for a 3D geometry, we have to resort to numerical approaches. We have employed the Wang-Landau algorithm [63] with single spin flip updates, which was invented for the determination of the density of states of classical models. Figure 6.6 shows the resulting density $\Gamma_{N_p}(u)$ as a function of u for a sc lattice with linear dimensions $L_x = 4, 6, 10$ and 12. As in the one-dimensional case, $\ln(\Gamma_{N_p}(u))$ diverges as $u \to 0$ and $u \to 1$. In fact, one can show that

$$\ln(\Gamma_{N_p}(u)) \underset{u \to 1}{\longrightarrow} (L-1)\ \ln(1-u) \tag{6.28}$$

in any spatial dimension (see App. A). This divergence has important impact on the low-temperature thermodynamic behavior. The entropy diverges logarithmically and the specific heat has a finite value for $T \to 0$. The scale in Fig. 6.6 might appear exaggerated, but it is actually the tiny tail close to $u = 1$ which will become important for low temperatures.

The computational effort of finite-temperature UHA is now essentially reduced to the Wang-Landau determination of $\Gamma_{N_p}(u)$, while the integration over u to calculate various physical results takes only a small amount of computer time. Therefore, results can be obtained for much larger lattices than with the conventional MC approach and, indeed, for a whole range of temperatures at once.

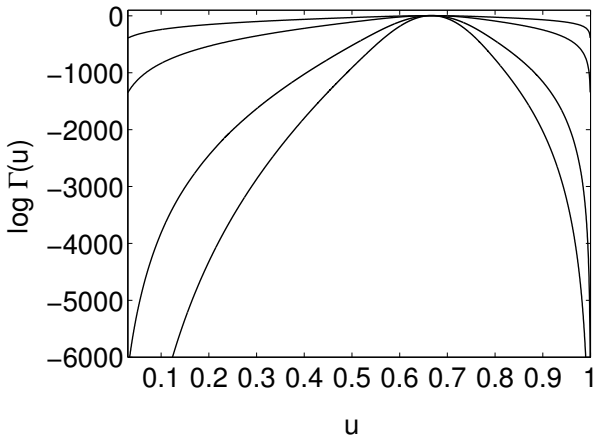

Figure 6.6: Density of corespin states $\Gamma_{N_p}(u)$ versus UHA parameter u for a sc lattice with linear size $L_x = 4$ (top), $L_x = 6, 10$ and $L_x = 12$ (bottom). All curves peak near $u = 2/3$, as in the 1D case.

6.5.2 FM to PM transition at $J_H = \infty, J' = 0$

We now study the 3D DE model in the UHA. Based on the tests of the previous section, we expect the UHA results to be reliable also in this case. We restrict the present discussion to the case $J_H = \infty, J' = 0$. For these parameters, only the FM and PM phases exist [8, 45].

The trend from PM to FM can already be seen in Fig. 6.1, where we show the expectation value $\langle u \rangle$ of the uniform hopping parameter and its standard deviation as a function of the inverse temperature β at $\mu = 0$. Already for a relatively small system, $p(u \,|\, \beta)$ is sharply peaked. Starting from $u = 2/3$ at high temperatures, the expectation value $\langle u \rangle$ tends towards unity, *i.e.* FM corespins, as $\beta \to \infty$. From Eq. (6.28) we find the asymptotic formula

$$u^* = 1 + \frac{1}{\beta \epsilon_k} \tag{6.29}$$

for the position u^* of the maximum of $p(u \,|\, \beta)$, where ϵ_k denotes the kinetic energy per lattice site of the tight-binding model with unit hopping parameter. It turns out that for $\beta \gtrsim 10$, the curves for u^* and $\langle u \rangle$ coincide. Well above this temperature, near $\beta \approx 5.5$, the variance of $p(u \,|\, \beta)$ shows a peak (see inset of Fig. 6.1), indicating important fluctuations near this temperature. For the determination of the Curie temperature of the DE model, we study the specific heat C_v as a function of temperature for various system sizes. The peaks of the specific heat at quarter filling ($n = 0.5$) are plotted in Fig. 6.7. They show signs of divergence as the lattice size increases. This indicates the presence of a second order phase transition from FM to PM. We identify the position $T^* \simeq 0.17$ of the peak as the phase transition temperature T_C at $n = 0.5$. This value is somewhat higher than that determinded with the Hybrid MC

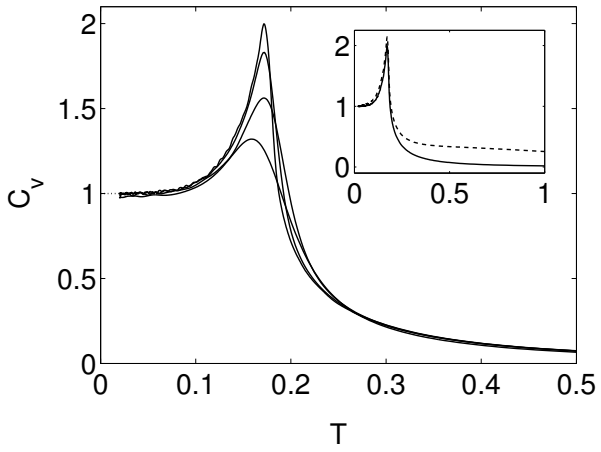

Figure 6.7: Specific heat per site of the sc DE model at $n = 0.5$ ($\mu = 0$) versus temperature for $L = 4^3$ (bottom), $L = 6^3, 10^3$ and $L = 16^3$ (top). Parameters are $J_H = \infty, J' = 0$. The results are obtained by the "canonical low-T approximation" (see text). In the inset, the approximate result for a 16^3 lattice is compared with that of an exact grand canonical calculation (dashed line).

algorithm [58] ($T_C \simeq 0.14$) for a 16^3 lattice but is better than the variational estimate [64] $T_C \simeq 0.19$.

In order to facilitate the calculation, particularly for electron fillings different from $n = 0.5$ ($\mu = 0$), we consider a canonical ensemble and replace the Boltzmann factor by $\mathrm{e}^{-\beta F}$. If the temperature is small on the electronic energy scale, we can replace the electronic free energy F by the ground state energy $F \simeq uE_k$. As introduced above, E_k denotes the kinetic energy at $T = 0$ of the tight-binding model with unit hopping amplitude (now in 3D) for a given electron filling. This approximation is justified because $T_C \lesssim 0.17$ is indeed small enough. The partition function now reads

$$Z = \int_0^1 du\, \Gamma_{N_p}(u)\, \mathrm{e}^{-\beta\, E_k\, u}\ . \tag{6.30}$$

The impact of this "canonical low-T approximation" is illustrated in the inset of Fig. 6.7. We find that the position of the peak is not affected at all. The only difference to the full grand canonical result is the longer tail at higher temperatures of the full result, which is due to additional fluctuations of the electrons.

The specific heat approaches a constant value $C_v = 1$ as $T \to 0$. This can be inferred from Eq. (6.29), since, for low temperatures, the internal energy per lattice site is given by $\epsilon_k\, u^*$ whose derivative with respect to temperature exactly yields unity. This explains the plateau of C_v for $T \lesssim 0.1$.

Signatures of the FM to PM phase transition should show up especially in the magnetic susceptibility [55] χ. For its calculation, the density $\Gamma_{N_p}(u)$ is not

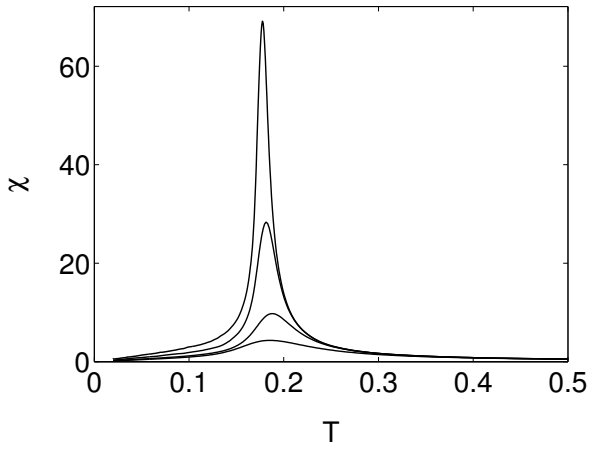

Figure 6.8: Magnetic susceptibility of the sc DE model at quarter filling ($n = 0.5$) versus temperature for lattice sizes 4^3 (bottom), $6^3, 10^3$ and 16^3 (top). Parameters are $J_H = \infty, J' = 0$. The results are obtained by the "canonical low-T approximation".

sufficient because a value u of the average hopping does not determine the magnetization m. Given the conditional probability $p(m \,|\, u)$ the moments of the magnetization are

$$\langle |m|^n \rangle \equiv \frac{1}{\mathcal{Z}} \int_0^1 du\, \Gamma_{N_p}(u)\, \mathrm{e}^{-\beta\Omega(u)}\, M^{(n)}(u)$$

with

$$M^{(n)}(u) = \int_0^1 dm\, |m|^n p(m \,|\, u)\ .$$

Estimates of the conditional moments $M^{(n)}(u)$ have been obtained in a second run of the Wang-Landau algorithm. A random walk in the space of all corespin configurations is performed whose acceptance is controlled by $1/\Gamma_{N_p}(u)$. An estimator of the susceptibility [65, 66] is then given by

$$\chi = \beta\, L \left(\langle m^2 \rangle - \langle |m| \rangle^2 \right) .$$

Figure 6.8 shows the susceptibility as a function of the temperature for various lattice sizes. We observe clear signs of a divergence near $T \simeq 0.18$ which corroborates the transition temperature obtained from the specific heat.

The filling dependence of T_C is easily determined from Eq. (6.30). Since the filling dependence only enters via E_k, which shows up in combination with β, we have the simple relation

$$\beta_c E_k = \text{const}$$

for the transition temperature. Thus the Curie temperature T_C is proportional to the kinetic energy E_k of the tight-binding model which, in turn, is a function of the electron filling. The proportionality of T_C to the bandwidth has already

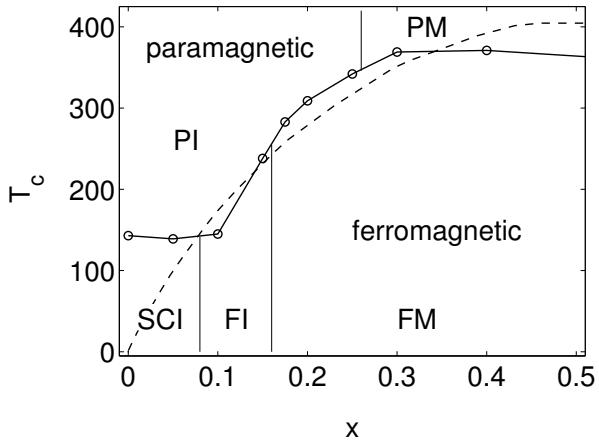

Figure 6.9: Curie temperature (dashed line) of the one-orbital DE model for a 16^3 cluster and $t = 0.2\,\mathrm{eV}$. Circles and phases PM, PI, FM, FI, and SCI are experimental results [6] for $La_{1-x}Sr_xMnO_3$.

been found based on different approximations [67, 68, 40]. In order to compare our calculations with experimental results, we fix the single free parameter in the DE model, i.e., the hopping amplitude. We choose $t = 0.2$ eV, a value reasonable for the material [1]. The dashed line of Fig. 6.9 shows the Curie temperature obtained from the DE model in UHA. We find astonishingly good agreement to the experimentally observed phase diagram of $La_{1-x}Sr_xMnO_3$ in the ferromagnetic regime. Our result is in sharp contrast to the claim made by Millis *et. al.* [60] that the DE model cannot even explain the right order of magnitude of T_C for the manganites. The reasoning of Ref. [60] starts from similar ideas as the UHA but is based on additional uncontrolled approximations. Our results for the DE model are in accord with other estimates [40, 42, 61].

The experimentally observed phase diagram shows additional phases for small concentrations: ferromagnetic insulating (FI), paramagnetic insulating (PI) and a spin-canting insulating (SCI) state. These states are not accounted for in our present approach. For a correct description, a finite value of J' is important, as well as generalizations of UHA, which will be discussed elsewhere [10].

6.6 Conclusions

In this paper we have presented the uniform hopping approach (UHA) for the FM Kondo model at finite temperature. We have used our method to calculate the ferromagnetic to paramagnetic phase transition temperature of the one-orbital DE model for large 3D systems. We find that the DE model yields a Curie temperature that is comparable to the experimental data.

The finite temperature UHA in the frame of the ESF model reduces the numerical effort of a simulation by several orders of magnitude, while retaining

all crucial physical features. In the example given in Sec. 6.4.2, the reduction factor is at least 10^6. The key idea is to map the physics of the high dimensional configuration space of the t_{2g} corespins onto an effective one-parametric model. The density of states entering our approach can be determined by the Wang-Landau algorithm. A full thermodynamic evaluation of the UHA model takes into account entropy and fluctuations of the corespins. Tests for 1D systems reveal that UHA results are in close agreement with unbiased MC data for static and dynamic observables.

This reduction in numerical effort will allow us to include phononic and/or orbital degrees of freedom in future numerical simulations in order to study more realistic models for the manganites.

6.7 Acknowledgements

This work has been supported by the Austrian Science Fund (FWF), project no. P15834-PHY. We are indebted to W. Nolting for stimulating discussions and to V. Martín-Mayor for drawing our attention to Refs. [59, 58, 64].

Chapter 7

Magnetic Polarons in the 1D FM Kondo Model

The[1] ferromagnetic Kondo model with classical corespins is studied via unbiased Monte-Carlo simulations. We show that with realistic parameters for the manganites and at low temperatures, the double-exchange mechanism does not lead to phase separation in one-dimensional chains but rather stabilizes individual ferromagnetic polarons. Within the ferromagnetic polaron picture, the pseudogap in the one-particle spectral function $A_k(\omega)$ can easily be explained. Ferromagnetic polarons also clear up a seeming failure of the double-exchange mechanism in explaining the comparable bandwidths in the ferromagnetic and paramagnetic phase. For our analysis, we extend a simplified model, the finite temperature uniform hopping approach (UHA), to include polarons. It can easily be evaluated numerically and provides a simple quantitative understanding of the physical features of the ferromagnetic Kondo model.

7.1 Introduction

Manganese oxides such as $La_{1-x}Sr_xMnO_3$ and $La_{1-x}Ca_xMnO_3$ have been attracting considerable attention since the discovery of colossal magnetoresistance (CMR) [36, 69]. These materials crystalize in the perovskite-type lattice structure where the crystal field breaks the symmetry of the atomic wave function of the manganese d-electrons. The energetically lower t_{2g} levels are occupied by three localized electrons. Due to a strong Hund coupling their spins are aligned, forming a localized corespin with $S = 3/2$. The electron configuration of the Mn^{3+} ions is $t_{2g}^3 e_g^1$, whereas for Mn^{4+} ions the e_g electron is missing. Due to a hybridization of the e_g wave function with the oxygen $2p$ orbitals, the e_g electrons are itinerant and can move from an Mn^{3+} ion to a neighboring Mn^{4+} via a bridging O^{2-}. The interplay of various physical ingredients such as the strong Hund coupling (J_H) of the itinerant electrons to localized corespins,

[1] This chapter has been submitted to Phys. Rev. B as Ref. [10].

Coulomb correlations, and electron-phonon coupling leads to a rich phase diagram including antiferromagnetic insulating, ferromagnetic metallic and charge ordered domains. The dynamics of the charge carriers moving in the spin and orbital background shows remarkable dynamical features [37, 38].

Since full many-body calculations for a realistic model, including all degrees of freedom, are not possible yet, several approximate studies of simplified models have been performed in order to unravel individual pieces of the rich phase diagram of the manganites. The electronic degrees of freedom are generally treated by a Kondo lattice model, which in the strong Hund coupling limit is commonly referred to as the double-exchange (DE) model, a term introduced by Zener [39]. In addition, the correlation of the itinerant e_g electrons is well described by a nearest neighbor (n.n.) Coulomb interaction. The on-site Hubbard term merely renormalizes the already strong Hund coupling. For the Kondo model with quantum spins it is still impossible to derive rigorous numerical or analytical results. If the S=3/2 corespins are treated classically, however, the model can be treated by unbiased Monte Carlo techniques. The impact of quantum spins on the electronic properties has been studied in Ref. [16, 53, 54]. It appears that quantum effects are important for (S=1/2) corespins or at $T = 0$. For finite temperature and S=3/2, classical spins present a reasonable approximation.

Elaborate Monte Carlo (MC) simulations for the FM Kondo model with classical t_{2g} corespins have been performed by Dagotto *et al.* [22, 41, 42], Yi *et al.* [55], and by Furukawa *et al.* [40, 56]. Static and dynamical properties of the model have been determined. These studies revealed features (discontinuity of the mean electron density as a function of the chemical potential, infinite compressibility) which have been interpreted as signatures of phase-separation (PS). PS has also been reported [57] from computations based on a dynamical mean field treatment of the DE model at $T = 0$. A phase diagram and critical exponents of the DE model have been determined with a Hybrid MC algorithm [58, 59].

In the manganites, the Hund coupling J_H is much stronger than the kinetic energy. Consequently, configurations are very unlikely in which the electronic spin is antiparallel to the local corespin. The present authors have proposed an effective spinless fermion (ESF) model [8] that takes effects of antiparallel spin configurations into account via virtual excitations. It has been demonstrated that the results of the ESF model are in excellent agreement with those of the original Kondo model even for moderate values of J_H. This applies also to features which have been previously interpreted as signatures of PS [42]. Taking Coulomb interactions into account, PS has been argued to lead to either small [33] or large [70] (nano-scale) clusters, which have been the basis for a possible though controversial [16] explanation of CMR [1, 71]. Moreover, lattice distortions [12, 44] are believed to play a crucial role for the CMR effect [16, 72] and should also be included in the model.

In this paper, we present a numerical and analytical study of the 1D ferromagnetic Kondo model with classical corespins. We find that the correct phys-

ical interpretation of the features which have been interpreted as PS in the one-dimensional model, is rather given by ferromagnetic polarons, i.e. small FM-regions with *one single* trapped charge-carrier, compatible with exact diagonalization results for small clusters [37]. This applies even without n.n. Coulomb repulsion invoked in Refs [70, 33]. Energetically, there is no significant difference between polarons, bi-polarons or even charge accumulations in the PS sense. It is rather the entropy, which even near zero temperature clearly favors polarons. The polaron picture allows also a straight forward and obvious explanation of the pseudogap, which has been previously observed in the spectral density [52, 73, 1, 8].

In a previous paper [8] we introduced the uniform hopping approximation (UHA), which replaces the influence of the random corespins on the e_g electron dynamics by an effective uniform hopping process. Essential physical features of the original model could be described even quantitatively by UHA, while the configuration space, and hence the numerical effort, was reduced by several orders of magnitude. Besides the numerical advantage, UHA also allows the derivation of analytical results in some limiting cases at $T = 0$.

In Ref. [9] we have extended UHA to finite temperatures by allowing for thermal fluctuations of the uniform hopping parameter. By taking into account the density of corespin states, it is possible to calculate thermodynamic quantities of one and three-dimensional systems in the UHA. The reliability of this finite-temperature UHA has been scrutinized by a detailed comparison of the results for various properties of the ferromagnetic Kondo model with unbiased MC data in 1D.

Here, we will generalize UHA to regimes, where a single hopping parameter is not sufficient to describe the physics of the FM Kondo model. Particularly near half filling, a typical corespin configuration shows small ferromagnetic domains (polarons) immerged in an antiferromagnetic background. Therefore, two different UHA-parameters are necessary to model the impact of the fluctuating corespins on the e_g electron dynamics.

This paper is organized as follows. In Sec. 7.2 the model Hamiltonian is presented and particularities of the MC simulation for the present model are outlined. The general discussion of ferromagnetic polarons near half filling is presented in Sec. 7.3. Section 7.4 develops a generalization of the uniform hopping approach in order to treat FM polarons. Polaronic features in the spectral density are analyzed. The key results of the paper are summarized in Sec. 6.6.

7.2 Model Hamiltonian and unbiased Monte Carlo

In this paper, we will concentrate solely on properties of the itinerant e_g electrons interacting with the *local* t_{2g} corespins. We also neglect the degeneracy of the e_g orbitals. The degrees of freedom of the e_g electrons are then described by a single-orbital Kondo lattice model [9]. As proposed by de Gennes [62],

Dagotto *et al.* [22, 1] and Furukawa [40], the t_{2g} spins $\mathbf{S}_i$ are treated classically, which is equivalent to the limit $S \to \infty$. The spin degrees of freedom ($\mathcal{S}$) are thus replaced by unit vectors $\mathbf{S}_i$, parameterized by polar and azimuthal angles θ_i and ϕ_i, respectively. The magnitude of both corespins and e_g-spins is absorbed into the exchange couplings.

7.2.1 Effective Spinless Fermions

It is expedient to use the individual t_{2g} spin direction $\mathbf{S}_i$ as the local quantization axis for the spin of the itinerant e_g electrons at the respective sites. This representation is particularly useful for the $J_H \to \infty$ limit, but also for the projection technique, which takes into account virtual processes for finite Hund coupling. As described in Ref. [8], the energetically unfavorable states with e_g electrons antiparallel to the local t_{2g} corespins can be integrated out. This yields the 1D effective spinless fermion model (ESF)

$$\hat{H} = -\sum_{<i,j>} t_{i,j}^{\uparrow\uparrow}\, c_i^\dagger\, c_j - \sum_{i,j} \frac{t_{i,j}^{\uparrow\downarrow}\, t_{j,i}^{\downarrow\uparrow}}{2J_H}\, c_i^\dagger c_i + J' \sum_{<i,j>} \mathbf{S}_i \cdot \mathbf{S}_j \;. \tag{7.1}$$

The spinless fermion operators c_j correspond to spin-up electrons (relative to the *local* corespin-orientation) only. The spin index has, therefore, been omitted. With respect to a *global* spin-quantization axis the ESF model (7.1) still contains contributions from both spin-up and spin-down electrons.

The first term in Eq. (7.1) corresponds to the kinetic energy in tight-binding approximation. The modified hopping integrals $t_{i,j}^{\sigma,\sigma'}$ depend upon the t_{2g} corespin orientation

$$t_{i,j}^{\sigma,\sigma'} \;=\; t_0\; u_{i,j}^{\sigma,\sigma'} \;, \tag{7.2}$$

where the relative orientation of the t_{2g} corespins at site i and j enters via

$$\begin{aligned} u_{i,j}^{\sigma,\sigma}(\mathcal{S}) &= \cos(\vartheta_{ij}/2)\; \mathrm{e}^{i\psi_{ij}} \\ u_{i,j}^{\sigma,-\sigma}(\mathcal{S}) &= \sin(\vartheta_{ij}/2)\; \mathrm{e}^{i\chi_{ij}} \end{aligned} \;. \tag{7.3}$$

These factors depend on the relative angle ϑ_{ij} of corespins $\mathbf{S}_i$ and $\mathbf{S}_j$ and on some complex phases ψ_{ij} and χ_{ij}.

The second term in Eq. (7.1) accounts for virtual hopping processes to antiparallel spin–corespin configurations and vanishes in the limit $J_H \to \infty$. The last term is a small antiferromagnetic exchange of the corespins.

It should be noted that the unitary transformation to the local spin quantization axis is not unique. This fact can be exploited to eliminate the phase factors ψ_{ij} in 1D. Then the n.n. hopping integrals are simply given by the real numbers $\cos(\vartheta_{ij}/2)$.

7.2.2 Grand Canonical Treatment

We define the grand canonical partition function as

$$\begin{aligned} \mathcal{Z} &= \int \mathcal{D}[\mathcal{S}] \quad \mathrm{tr}_c \, \mathrm{e}^{-\beta(\hat{H}(\mathcal{S})-\mu\hat{N})} \\ \int \mathcal{D}[\mathcal{S}] \; &= \prod_{i=1}^{L} \Big(\int_0^{\pi} d\theta_i \sin\theta_i \int_0^{2\pi} d\phi_i \Big) \, , \end{aligned} \tag{7.4}$$

where tr_c indicates the trace over fermionic degrees of freedom at inverse temperature β, $\hat{N}$ is the operator for the total number of e_g electrons and μ stands for the chemical potential. Upon integrating out the fermionic degrees of freedom, we obtain the statistical weight of a corespin configuration $\mathcal{S}$ that can be written as

$$w(\mathcal{S}) = \frac{\mathrm{tr}_c \, \mathrm{e}^{-\beta(\hat{H}(\mathcal{S})-\mu\hat{N})}}{\mathcal{Z}} \, . \tag{7.5}$$

Equation (7.4) is the starting point of Monte Carlo simulations of the Kondo model [22] where the sum over the classical spins is performed via importance sampling. The spin configurations $\mathcal{S}$ enter the Markov chain according to the weight factor $w(\mathcal{S})$ that is computed via exact diagonalization of the corresponding one-particle Hamiltonian in Eq. (7.1). In the 1D case we have performed MC simulations in which spins in domains of random lengths were rotated. We have performed MC runs with 2000 measurements. The skip between subsequent measurements was chosen to be some hundreds of lattice sweeps reducing autocorrelations to a negligible level.

As previously shown [9], the spin-integrated one-particle Green's function can be written as

$$\sum_{\sigma} \ll a_{i\sigma}; a_{j\sigma}^{\dagger} \gg_{\omega} = \int \mathcal{D}[\mathcal{S}] \; w(\mathcal{S}) u_{ji}^{\uparrow\uparrow}(\mathcal{S}) \ll c_i; c_j^{\dagger} \gg_{\omega}^{\mathcal{S}} \, , \tag{7.6}$$

where $\ll c_i; c_j^{\dagger} \gg_{\omega}^{\mathcal{S}}$ is the Green's function in local spin quantization. It can be expressed in terms of the one-particle eigenvalues $\epsilon^{(\lambda)}$ and the corresponding eigenvectors $|\psi^{(\lambda)}\rangle$ of the Hamiltonian $\hat{H}(\mathcal{S})$:

$$\ll c_i; c_j^{\dagger} \gg_{\omega}^{\mathcal{S}} = \sum_{\lambda} \frac{\psi^{(\lambda)}(i) \; \psi^{*(\lambda)}(j)}{\omega - (\epsilon^{(\lambda)} - \mu) + i0^{+}}$$

It should be pointed out that the one-particle density of states (DOS) is independent of the choice of the spin-quantization.

7.2.3 Uniform Hopping Approach

The integral over the corespin states in the partition function (7.4) can be evaluated approximatively by resorting to a uniform hopping approach (UHA) [9].

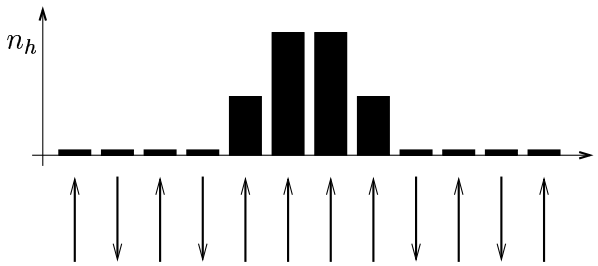

Figure 7.1: Idealized spin and hole-density configuration in a 1D Kondo chain at the critical chemical potential μ^*. A FM domain of $L_f = 4$ lattice sites is embedded in an AFM background. A single hole is localized in the FM domain giving rise to the depicted hole density (different from the schematic shape in Fig 4 of Ref. [51]).

The key idea is to replace the impact of the locally fluctuating corespins on the hopping amplitudes by some global average quantity u. Then the Hamiltonian merely depends on one parameter, namely u, and the partition function can be written as the one-dimensional integral

$$\mathcal{Z} = \int_0^1 du\, \Gamma(u)\ \mathrm{tr}_c\, \mathrm{e}^{-\beta(\hat{H}(u)-\mu\hat{N})}\ .$$

The density of corespin states $\Gamma(u)$ can be obtained numerically for 3D systems and analytically for 1D systems.

Obviously, this simplification assumes a uniform medium. In order to cope with magnetic polarons, the UHA has to be generalized and $\Gamma(u)$ should be replaced by a two-parameter density $\Gamma(u_f, u_a)$, where $u_f(u_a)$ denotes the average hopping within the (anti)ferromagnetic domains. The details and results of such a generalization are the contents of Sec. 7.4 of this paper.

7.3 Ferromagnetic Polarons

Near half filling of a single e_g band, a tendency towards phase separation has been observed in various studies. It has been claimed that the system separates into FM domains of high carrier concentration and AFM domains of low carrier concentration. In the following we show that a different picture rationalizes the 1D Monte Carlo results in the range $n \approx 0.7 - 1.0$.

We show that ferromagnetic polarons, i.e. *single* charge carriers surrounded by small ferromagnetic spin-clouds, are formed when holes are doped into the half filled e_g band. In order to model such a polaron in a one-dimensional system, we take L_f adjacent lattices sites to be in ferromagnetic order and use $\Gamma_{L-L_f}(u)$ to account for the degeneracy of the remaining spins.

First, we estimate the size L_f of the FM polaron [24] using a simple polaron picture. In this view the hole is confined in a perfectly FM domain consisting

of L_f lattice sites and outside the domain the system is in perfect AFM order (see Fig. 7.1). The tight-binding energies in a potential well (FM domain) with infinite barrier height are

$$\epsilon_\nu = -2\,\cos\big(\frac{\nu\,\pi}{L_f+1}\big)\,, \qquad \nu = 1,\ldots,L_f\,. \tag{7.7}$$

The energy difference between a) a one-polaron state with perfect FM spins within the polaron and perfect AFM order outside and b) perfectly antiferromagnetically ordered t_{2g} spins is given by

$$\Delta\epsilon_p = -2\cos\Big(\frac{\pi}{L_f+1}\Big) + 2J_{\rm eff}\,(L_f-1)\,,$$

where the first term accounts for the kinetic (delocalization) energy of the hole in the potential well and the second term describes the energy deficiency due to (L_f-1) ferromagnetic bonds. We have introduced the effective antiferromagnetic coupling $J_{\rm eff}$, given by

$$J_{\rm eff} = J' + 1/(2J_H)$$

near $n \approx 1$ (see Ref. [8]). For typical values $J_H = 6$ and $J' = 0.02$ we have $J_{\rm eff} \approx 0.1$. Upon minimizing $\Delta\epsilon_p$ with respect to L_f, we obtain the optimal size of the polaron, which in the present case lies between $L_f = 3$ and $L_f = 4$. If the FM domain contains $N > 1$ charge carriers, the energy difference is simply

$$\Delta\epsilon_p(N) = -2\sum_{\nu=1}^{N}\,\cos\Big(\frac{\nu\,\pi}{L_f+1}\Big) + 2J_{\rm eff}\,(L_f-1)\,.$$

For $N = 2$, the optimum bi-polaron size is $L_f \simeq 7$ and it increases to $L_f \simeq 10$ for $N = 3$ charge carriers.

Next we estimate the chemical potential μ^*, at which holes start to populate the polaron states. Apart from the energy of the antiferromagnetic t_{2g} spins, the total energy (at $T = 0$) of the filled e_g band is given in the grand canonical ensemble by $-\mu^*\,L$. By equating this energy to the total energy of the polaron we have

$$-\mu^*\,L = -\mu^*\,(L-1) + \Delta\epsilon_p(1)$$

which yields the desired chemical potential

$$\mu^* = -\Delta\epsilon_p(1) = 2\cos\big(\frac{\pi}{L_f+1}\big) - 2J_{\rm eff}\,(L_f-1)\,.$$

The critical chemical potential is depicted in Fig. 7.2. Similar considerations yield that μ^* also approximately presents the limiting chemical potential between the filled antiferromagnetic band and a state with several single FM polarons, provided the polaron density is low, i.e. as long as we have an antiferromagnetic background. Consequently, at the chemical potential μ^* the electron density is not fixed. The energy gain $\Delta\epsilon_p$ exactly balances the loss of the chemical potenital $-\mu^*$. This implies that the electron density has a

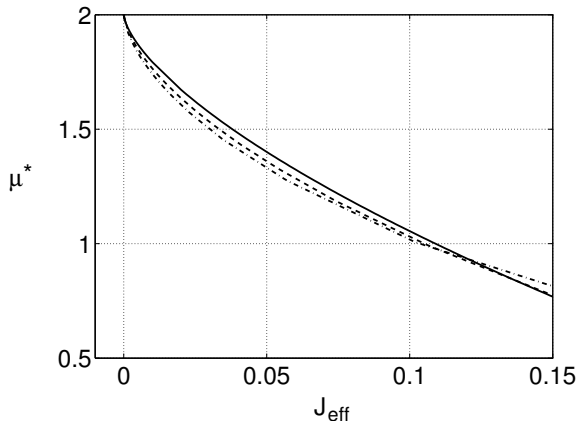

Figure 7.2: Critical chemical potential $|\mu^c|$ of the homogeneous model (solid line) from Ref. [8] as compared to the chemical potential μ^* at which polarons (dash dotted) and bipolarons (dashed) start to enter the Kondo chain.

discontinuity at μ^*, *i.e.* the compressibility of the electrons diverges which has been previously interpreted as a consequence of PS tendencies (see Fig. 3a in Ref. [70] and Ref. [40]). If we repeat the considerations for bi-polarons with the respective optimized size ($L_f \simeq 7$ for the standard parameter set), we find a critical chemical potential, also depicted in Fig. 7.2, which is very close to that of polarons. If we proceed to tri-polarons we find again a similar μ^*. As can be seen in Fig. 7.2, the chemical potential μ^* virtually coincides with the chemical potential μ^c of the "phase separation" obtained in Ref. [8]. This potential was calculated as the point of coexistence of FM and AFM order in a homogeneous system. In view of the rather rough estimate of μ^* we conclude that polarons, bi-polarons, up to phase separated FM regions, are energetically comparable as long as the size of the FM domains is optimally adapted. For $J_{\text{eff}} \gtrsim 0.12$ which is comparable with the antiferromagnetic exchange in manganites, individual polarons are energetically favored.

FM polarons, however, have a much higher entropy than the other objects and are therefore thermodynamically favored, even at low temperature. Moreover, at $T \neq 0$ the domains are not completely (anti)ferromagnetically aligned which further reduces the energy differences between polaron and bi-polaron/phase-separated states considerably. Therefore, even for values of $J_{\text{eff}} < 0.12$ we find individual polarons at very low temperatures. This conclusion is corroborated at $\beta = 50$ and $J_{\text{eff}} \simeq 0.10$ by the ensuing analysis of MC simulations.

In order to scrutinize the polaron arguments, we compute the mean particle numbers for the corespin configurations entering the Markov chain of unbiased MC

$$\langle \hat{N} \rangle_{\mathcal{S}} := \frac{\mathrm{tr}_c\big(\hat{N}\, \mathrm{e}^{-\beta(\hat{H}(\mathcal{S})-\mu\hat{N})}\big)}{\mathrm{tr}_c\big(\mathrm{e}^{-\beta(\hat{H}(\mathcal{S})-\mu\hat{N})}\big)} = \sum_{\nu=1}^{L} \frac{1}{1+\mathrm{e}^{\beta(\epsilon_\nu(\mathcal{S})-\mu)}} \,,$$

where $\epsilon_\nu(\mathcal{S})$ are the eigenvalues of $\hat{H}(\mathcal{S})$ for the configuration $\mathcal{S}$. As a conse-

quence of the above reasoning we expect a broad distribution of integer-valued particle numbers if the chemical potential is close to μ^*. The MC time series for $\langle \hat{N} \rangle_{\mathcal{S}}$ for a $L = 50$ site chain ($J_H = 6, J' = 0.02, \beta = 50$) is shown in Fig. 7.3. One time step corresponds to 1000 sweeps of the lattice. The inverse temperature $\beta = 50$ corresponds to $T \simeq 50 - 100$ K, *i.e.* a temperature relevant for experiments.

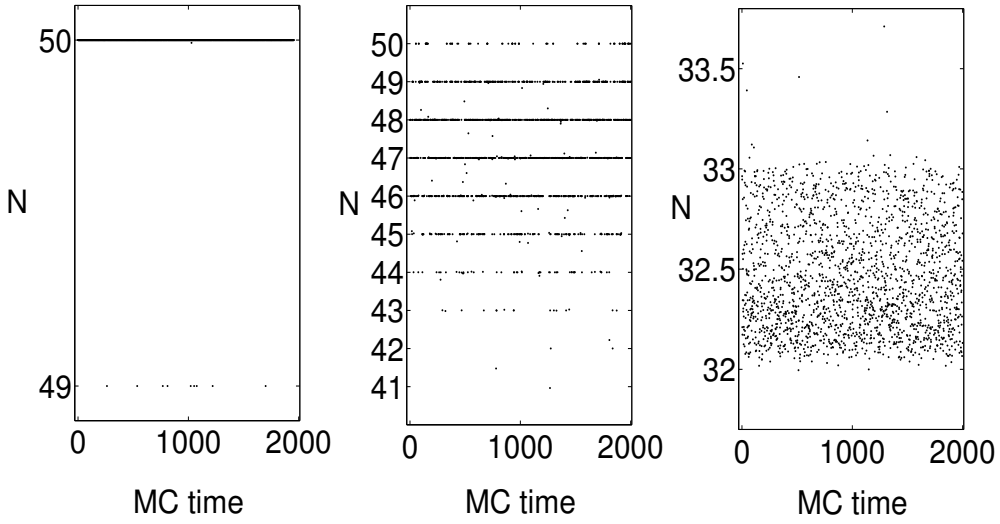

Figure 7.3: Mean particle numbers in a grand canonical MC simulation ($L = 50, J_H = 6, J' = 0.02, \beta = 50$) as a function of MC time. One time step corresponds to 1000 sweeps of the lattice. a) AFM case ($\mu = 1.22$) b) polaron regime ($\mu \simeq \mu^* \simeq 1.02$) c) FM regime ($\mu = 0.80$).

The left-hand panel corresponds to a situation where the chemical potential is far above the critical chemical potential, which has the value $\mu^* \simeq 1.02$ for the present parameter set. We see that the band is almost completely filled, with isolated dots at $N_e = 49$ corresponding to occasional FM polarons. At μ^* (central panel), in agreement with the polaron picture we find a broad distribution of *integer-valued* mean particle numbers. If the chemical potential is reduced below μ^*, the system becomes ferromagnetic and we find the standard result of free electrons with a narrow and continuous spread in $\langle \hat{N} \rangle$ not restricted to integer values.

Hole-dressed spin-spin correlations provide another piece of evidence in favor of FM polarons. The bulk of Monte Carlo snapshots (not shown), as taken from simulations for the FM Kondo model, contains isolated FM polarons of size $L_f = 3$ or $L_f = 4$. Once in a while two of them collide and form passing bi-polarons. The observed fraction of bi-polarons corresponds to a random distribution of polarons. In order to quantify the information revealed by the MC-snapshots, we introduce a modified corespin correlation function

$$S_n(l) = \frac{1}{L-l} \sum_{i=1}^{L-l} n_i^h \, \mathbf{S}_i \cdot \mathbf{S}_{i+l} \tag{7.8}$$

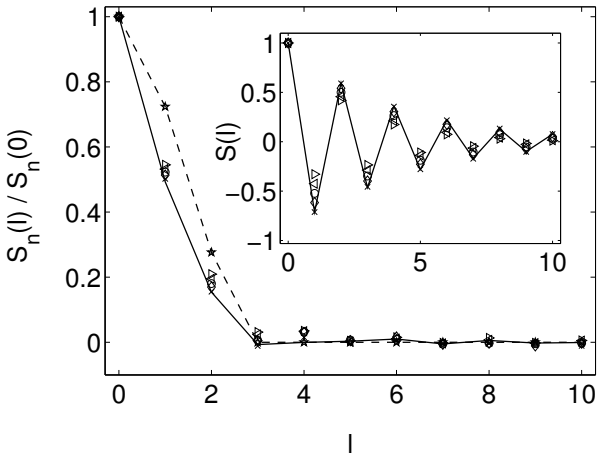

Figure 7.4: Modified spin-spin correlation function from unbiased MC for an $L = 50$-site chain containing one ($\times$), two ($\diamond$), three ($\circ$), four ($\triangleleft$), and five ($\triangleright$) holes. The inset shows the conventional spin-spin correlation function $S(l) = \frac{1}{L-l}\sum_{i=1}^{L-l} \mathbf{S}_i \cdot \mathbf{S}_{i+l}$. The dashed line is calculated within the simple polaron picture, while the solid line represents the generalized UHA result for a single polaron. Parameters are $\beta = 50$, $J' = 0.02$, and $J_H = 6$.

that measures the corespin correlations in the vicinity of a charge carrier (hole). The density operator n_i^h for holes at site i is related to the density operator for electrons via $n_i^h = 1 - n_i$. Figure 7.4 shows the results of an unbiased grand canonical MC simulation. The observables are evaluated at different subspaces with a fixed particle number. We observe ferromagnetic correlations that vanish at $l = 3$ corresponding to a polaron that extends over $L_f = 4$ lattice sites. It should be pointed out that the MC result is almost independent of the number of holes in the system. In particular, the data do not indicate any enlargement of the FM domain for a larger number of holes. This result can only be explained by individual FM polarons because the size of the FM domain would strongly increase if there were two or more holes trapped in it.

The inset of Fig. 7.4 shows the conventional corespin correlation function $S(l)$. We observe the expected antiferromagnetic correlations, which decrease slightly with increasing number of holes.

The result for the modified spin-spin correlation function can again be explained qualitatively by the simple polaron picture. We consider a single polaron in which one charge-carrier is confined. Let the probability for the hole to be at site ν in the FM region be p_ν, which is roughly given by the result for a particle in an infinite potential well (see Fig. 7.1): $p_\nu \propto \sin^2(\nu\ \pi/(L_f + 1))$. The spin correlation is computed assuming perfect FM order inside the polaron and perfect AFM order outside. The result of this simple idea for $L_f = 4$ is shown as the dashed line in Fig. 7.4. It agrees qualitatively with the MC data.

For a quantitative, but still fairly simple description, we will now generalize the

uniform hopping approximation, to allow for FM polarons.

7.4 UHA for FM polarons

In the previous section we have interpreted the MC data by using the simplest polaron ideas. In what follows we will refine our polaron picture by including thermodynamic fluctuations of the corespins. This is done by a generalization of the finite-temperature uniform hopping approach (UHA) introduced in Ref [9].

In the spirit of UHA, the impact of the corespins on the motion of the e_g electrons is now described by two UHA parameters, u_f and u_a, for the FM and AFM region, respectively. These two parameters are averages of the hopping amplitudes in the FM and AFM domains, respectively. Their distribution is given by a two-parameter density of states denoted by $\Gamma_{N_f,N_a}(u_f,u_a)$.

The size of individual polarons is fixed to L_f lattice sites. It is, however, possible that polarons overlap. The positions of the polarons are specified by the locations $\{i_1,\ldots,i_m\}$ of their left ends, where m is the number of FM polaron wells. If polarons overlap, they may form a bi-polaron or even greater accumulations of holes. The grand canonical partition function in this generalized UHA reads

$$\mathcal{Z}=\sum_m \sum_{\{i_1,\ldots,i_m\}} \iint_0^1 du_f du_a\, \Gamma_{N_f,N_a}(u_f,u_a)\ \mathrm{tr}_c\, \mathrm{e}^{-\beta(\hat{H}(u_f,u_a;i_1,\ldots,i_m)-\mu\hat{N})}\ . \tag{7.9}$$

For 1D chains, subject to open boundary condition, the joint density $\Gamma_{N_f,N_a}(u_f,u_a)$ depends merely upon the number N_f (N_a) of bonds in FM (AFM) regions. In higher dimensions, $\Gamma_{N_f,N_a}(u_f,u_a)$ would actually depend upon the location of the individual polarons. The generalized UHA Hamiltonian reads

$$\begin{aligned}\hat{H}(u_f,u_a;i_1,\ldots,i_m) = &-\sum_{<ij>} u_{ij}\ c_i^\dagger c_j - \frac{z}{2J_H}\sum_i \left(1-\frac{1}{z}\sum_\delta u_{i,i+\delta}^2\right) n_i \\ &+ J'\sum_{\langle ij\rangle}(2\ u_{ij}^2-1)\ ,\end{aligned} \tag{7.10}$$

where δ stands for n.n. vectors and z denotes the coordination number. The UHA parameter u_{ij} are either u_f or u_a, depending upon the type of magnetic order at the adjacent sites i and j. The integrand of the partition function in Eq. (7.9) defines the joint thermal probability density $p(u_f,u_a\,|\,\beta)$. From $p(u_f,u_a\,|\,\beta)$, we estimate mean values $\overline{u}_f,\overline{u}_a$ of u_f and u_a of a $L=20$-site chain reading

$$\overline{u}_f=0.937\ ,\quad \overline{u}_a=0.31 \tag{7.11}$$

for the standard parameter set $J'=0.02$ and $J_H=6$ and $\beta=50$. These mean values are independent of the number of polarons and their positions as long as the total volume of the polarons is small compared to the system size. In order

to simplify the following discussion, we will replace the thermal averaging of an observable by the value of that observable at $\overline{u}_f, \overline{u}_a$. For the partition function this yields the simple form

$$\mathcal{Z} = \sum_m \sum_{\{i_1,\ldots,i_m\}} \mathrm{tr}_c \, \mathrm{e}^{-\beta(\hat{H}(\overline{u}_f,\overline{u}_a;i_1,\ldots,i_m)-\mu(L-m))} \; , \tag{7.12}$$

where the influence of the thermal fluctuations of the corespins is contained in the average hopping amplitudes $\overline{u}_f$ and $\overline{u}_a$.

These average hopping amplitudes, however, are not sufficient for the determination of observables that do not directly derive from the partition function such as spin-spin correlations and one-particle spectral functions. In principle, these observables can be calculated in UHA by averaging over a set of *typical* thermal corespin configurations $\{\mathcal{S}\}$ obtained in UHA. In order to construct such a set, the azimuthal angles are also required, although they do not enter the energy and have a flat thermal probability density. The simplest way of constructing typical corespin configurations is to draw azimuthal angles at random. Starting from the reference spin $\mathbf{S}_\nu$ we proceed to the neighboring corespins by adding a random azimuthal angle χ to the fixed relative polar angle. Thus we obtain a collection of typical corespin configurations $\{\mathcal{S}\}$.

7.4.1 Static Correlations

We continue the discussion of the modified spin-spin correlation function $S_n(l)$. For a quantitative, but still fairly simple description, we take the deviations from perfect FM and AFM order into account, while for the hole the approximate probabilities p_ν are retained. We employ the mean UHA parameters $\overline{u}_f$ and $\overline{u}_a$ to describe the relative angles of neighboring corespins and average over typical corespin configurations with random hole positions. A comparison of the unbiased MC results with those of this approximate polaron approach, depicted in Fig. 7.4, reveals an excellent agreement.

Another observable to distinguish between polarons, bi-polarons, or even phase separated high density FM clusters is the density-density correlation function

$$C(l) := \frac{1}{L-l} \sum_{i=1}^{L-l} \langle (n_i^h - \langle n_i^h \rangle)(n_{i+l}^h - \langle n_{i+l}^h \rangle) \rangle \; . \tag{7.13}$$

If holes form independent FM polarons, the correlation function should be structureless, while if holes gather in one FM regime, the correlation function will exhibit a positive peak at a typical inter-particle distance. In Fig. 7.5 $C(l)$ is shown for the two-hole subspace, where only those spin configurations of the Markov chain are taken into account, for which $N_h \simeq 2$. The UHA-polaron result is derived as follows. The positions of two FM-regions of size $L_f = 4$ are chosen at random, including overlapping ones. The hopping parameters are $\bar{u}_f$ ($\bar{u}_a$) for FM (AFM) bonds and the resulting tight-binding model is solved. The lowest two eigenstates will then be localized in the two FM potential wells. The

resulting correlation functions are averaged over all possible positions of the FM potential wells. We observe a strikingly close agreement with the unbiased MC results. Similarly we proceed in the bi-polaron case, which is characterized by a single FM region of optimized size ($L_f = 7$). Here the two holes occupy the ground state and first excited state of the FM potential well. The resulting correlation function differs drastically from the MC data.

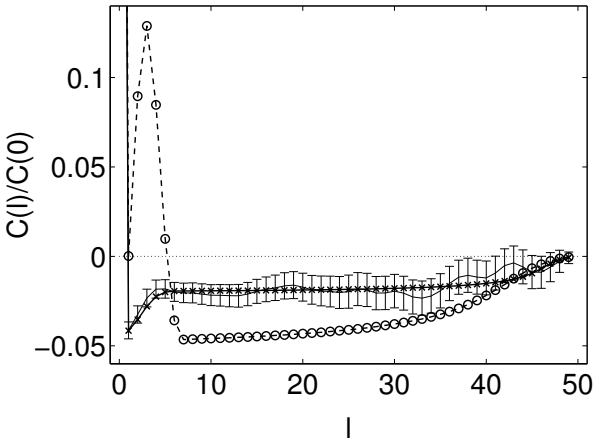

Figure 7.5: Density density correlation function for $L = 50, \beta = 50, J' = 0.01, J_H = 6$, and $N_h = 2$. Error bars represent unbiased MC data, crosses stand for polaron-, and circles for bi-polaron results in UHA.

This discrepancy increases with increasing hole number, which shows clearly that the physics of the 1D FM Kondo model is correctly described by single-hole polarons and not by phase separation.

7.4.2 Polaronic features in the spectral density

In this subsection, we compute the spin-integrated spectral density

$$A_k(\omega) = -\frac{1}{\pi} \sum_{\sigma} \Im \ll a_{k\sigma}; a^{\dagger}_{k\sigma} \gg_{\omega}$$

for the original DE model by unbiased MC simulations based on the expression Eq. (7.6). The results will again be analyzed by UHA in the framework of the polaron ansatz. In particular the pseudogap in the spectral density near $n = 1$, found in the FM Kondo model [51, 8], can readily be explained in the polaron picture. It is a consequence of the ferromagnetic box in which the hole moves.

The computation of $A_k(\omega)$ in UHA is based on the reasoning that led to the partition function in Eq. (7.12). I.e., for each polaron configuration and each value of $\bar{u}_a$, eigenvalues $\epsilon^{(\lambda)}$ and eigenvectors $|\psi^{(\lambda)}\rangle$ of the respective tight-binding Hamiltonian are determined, from which the Green's function

$$\ll c_i; c^{\dagger}_j \gg_{\omega}^{\bar{u}_a, \bar{u}_f} \quad .$$

is determined in local spin-quantization. The transformation to the global spin-quantization is given by Eq. (7.6)

$$\sum_{\sigma} \ll a_{i\sigma}; a^{\dagger}_{j\sigma} \gg^{\mathcal{S}}_{\omega} = \; u^{\uparrow\uparrow}_{j,i}(\mathcal{S}) \ll c_i; c^{\dagger}_{j} \gg^{\bar{u}_a,\bar{u}_f}_{\omega} \quad . \tag{7.14}$$

In the framework of UHA the relative angles of neighboring spins are fixed by the parameters $\bar{u}_a$ and $\bar{u}_f$. For a unique description of the entire spin configuration, however, azimuthal angles are again required. We proceed like in the discussion corresponding to Eq. (7.13), i.e. for fixed parameters $(\bar{u}_f, \bar{u}_a)$, spin configurations are generated with a flat sampling distribution in azimuthal angles. This is little numerical effort, as only the prefactor $u^{\uparrow\uparrow}_{ij}(\mathcal{S})$ is affected.

In the transition region ($\mu \simeq \mu^*$), the number of polaron wells is not well defined, as pointed out in conjunction with Fig. 7.3. In order to obtain a detailed understanding we compare unbiased MC data and results of the polaron ansatz in the subspace of fixed particle (polaron) number.

Antiferromagnetism at half filling

We begin the discussion with the spectrum of the AFM state for the completely filled lower Kondo band (no polarons). The unbiased MC data as shown in

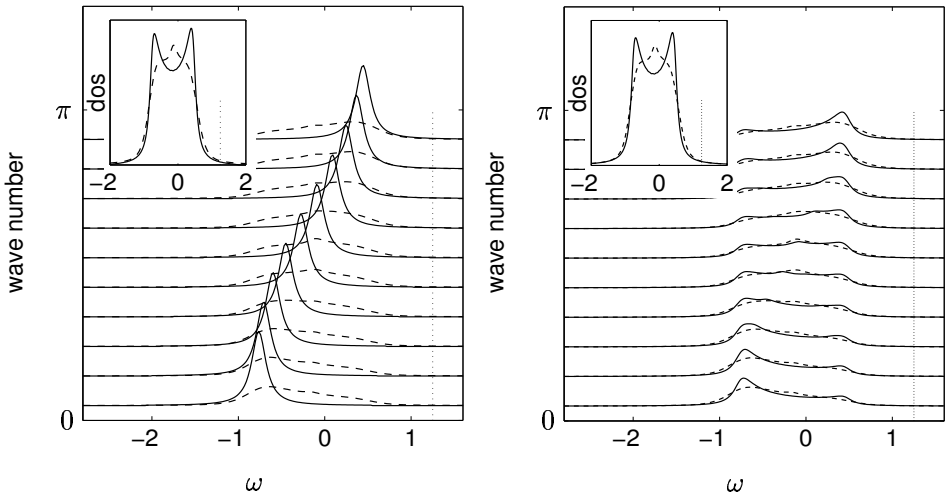

Figure 7.6: Spectral density of a half-filled Kondo chain with parameters $L = 20, \beta = 50, J' = 0.02, J_H = 6$, and $\mu = 1.25$. Dashed lines represent unbiased MC data, solid lines stand for UHA result ($\bar{u}_a = 0.31$). Inset: density of states. The vertical bar indicates the chemical potential. The left(right)-hand panel shows UHA-results in local (global) spin quantization. Error bars have been omitted for clarity.

Fig. 7.6 display broad structures due to incoherent motion of charge carriers in a spin background that exhibits random deviations from perfect AFM order. The

result can be described by the UHA ansatz. For the mean value of the hopping amplitude we have $\bar{u}_a = 0.31$ which corresponds to $\langle S_i S_{i+1} \rangle = \cos(\vartheta) \simeq -0.7$. Since there are no holes, and consequently no polarons, the UHA parameters are the same for all bonds. The left-hand panel in Fig. 7.6 shows the UHA result in local quantization, i.e. without the transformation given in Eq. (7.14). In local quantization, the spectral density is simply given by

$$A_k(\omega) = \delta(\omega - 2\bar{u}_a \cos(k)) \; .$$

The agreement with the unbiased MC result is rather poor at this stage although the band width is already well approximated. In the MC spectra, only very weak remnants of the tight-binding features are visible on top of the incoherent spectrum, which is almost k-independent.

However, if we take into account the necessary transformation Eq. (7.14) to a global spin quantization, the agreement is strikingly close (see right-hand panel). The quasi-particle dispersion is strongly smeared out due to the random azimuthal angles of the corespins. There are two minor discrepancies between UHA and unbiased MC. The tight-binding remnants are more pronounced in UHA, while the MC results exhibit a weak structure near $\omega = 0$, which is due to random fluctuations in the relative n.n. angles, resulting in locally trapped electrons. Nonetheless, at half-filling UHA and unbiased MC simulations yield compatible results for the spectral density and the density of states (insets of Fig. 7.6).

Ferromagnetic Polarons

Next we consider the case of one hole in the otherwise half-filled Kondo chain. To this end, we investigate the grand canonical MC data in the $N_h = 1$ subspace. The respective MC spectrum is shown in Figs. 7.7 and 7.8. The main feature of the spectrum is a broad incoherent background, similar to the one found in the AFM case. In addition, two dispersionless structures are visible at $\omega \approx \pm 1.5$. As discussed earlier [51, 8], a pseudogap shows up at the chemical potential. We find that an additional (mirror) gap appears at the opposite side of the spectrum.

Before discussing the UHA result, we want to provide a rough explanation of the MC data in terms of a simple polaron model. We assume an FM polaron-well of size $L_f = 4$, characterized by a tight-binding hopping parameter $\bar{u}_f$ embedded in an antiferromagnetic background with hopping parameter $\bar{u}_a$. Since the two hopping parameters are very different, we treat the various regions as separate chains and neglect their interaction. I.e. there is an isolated tight-binding chain of size L_f corresponding to the FM region, and one or two chains corresponding to the AFM background. A carrier is localized either in the FM or the AFM domain. The eigenvalues in the FM region, $\varepsilon_\nu^f = -2\bar{u}_f \cos(k_\nu^f)$, depend on the momentum $k_\nu^f = \nu\pi/(L_f + 1)$ with $\nu = 1, \ldots, L_f$. The energies of states corresponding to different localizations of the FM well ($i_0 = 1, \ldots, L - L_f$) are

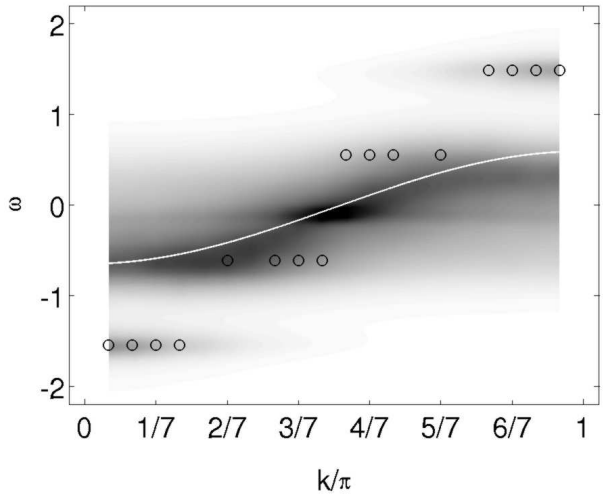

Figure 7.7: Spectral density for $N_h = 1$ holes (one polaron). Parameters like in Fig. 7.6, except $\mu = 1.1$. Comparison of MC data (gray scale plot) with results of the simple polaron-well model. Circles (solid bright lines) stem from states localized in the FM (AFM)-well. Hopping parameters for the polaron-well model are $\bar{u}_f = 0.937$, $\bar{u}_a = 0.31$, and $L_f = 4$.

degenerate. The corresponding eigenstates in real space read

$$\psi_i^{(k_\nu,i_0)} \propto \begin{cases} \sin((i-i_0+1)k_\nu), & i_0 \le i < i_0 + L_f \\ 0, & \text{otherwise.} \end{cases}$$

In this simple polaron-well model the expression for that part of the spectral density in local spin-quantization is

$$\begin{aligned} A_k^f(\omega) &\propto \sum_{\nu=1}^{L_f} \sum_{i_0=1}^{L-L_f} \left|\langle k|\psi^{(k_\nu,i_0)}\rangle\right|^2 \delta(\omega-\epsilon_\nu^f) \\ &\propto \sum_{\nu=1}^{L_f} c_\nu(k)\ \delta(\omega-\epsilon_\nu^f)\ , \end{aligned} \tag{7.15}$$

where $|k\rangle$ stands for the eigenvectors of the homogeneous tight-binding model with open boundary condition, i.e. $\langle j|k\rangle \propto \sin(j\,k)$. The coefficient $c_\nu(k)$ as function of k shows a broad hump at $k \simeq k_\nu$. Hence, the contributions of the FM regions to $A_k(\omega)$ are dispersionless structures at energies $\omega = \epsilon_\nu^f$ which are concentrated about $k = k_\nu^f$. These structures are marked by open circles in the grayscale plot of Fig. 7.7. They explain the additional features at the band edges, which are clearly visible in the spectral density in addition to the broad incoherent background. The latter is due to the motion of the hole in the AFM regions. Since the AFM regions are much larger than the FM well, a continuous tight-binding band develops, characterized by the hopping parameter $\bar{u}_a$. The band is shown as a white line in Fig. 7.7. This part of the spectrum is similar to

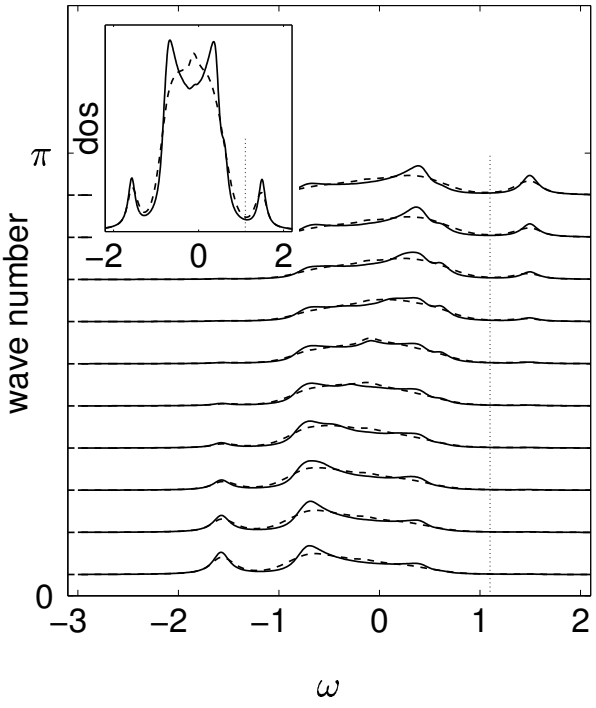

Figure 7.8: Spectral density for $N_h = 1$ hole (one polaron). Symbols like in Fig. 7.6 and parameters like in Fig. 7.7. The broad incoherent central part of the spectrum (width $\simeq 2\bar{u}_a$) derives from the motion of the electrons in the fluctuating AFM background. Polaronic peaks show up at $\omega \simeq \pm 1.5$. In between these two structures a pseudogap opens at the chemical potential μ^*. It is accompanied by a mirror pseudogap near $-\mu^*$.

that at half filling (Fig. 7.6). The remaining discrepancy as compared to the MC data is due to the fluctuations of the azimuthal angles of the corespins causing the white line to become more incoherent, as shown by the UHA calculations below. The transformation from local to global spin-quantization has, however, negligible impact on the polaron states in the spectrum, since they are due to the FM region, in which the fluctuations of the corespins are less relevant. As we can see in Fig. 7.7, our reasoning based on a single polaron well already describes the qualitative features correctly.

The origin of the pseudogap and its 'mirror image' on the opposite side of the spectrum can now be simply identified as the energy difference between the uppermost (lowest) state in the FM potential well ($E = \mp 2\bar{u}_f \cos(\pi/(L_f + 1))$) and the upper (lower) edge of the tight-binding band in the AFM region ($E = \mp 2\bar{u}_a$) leading to a width of the pseudogap $\Delta E = 2(\bar{u}_f \cos(\pi/(L_f + 1)) - \bar{u}_a)$, see Fig. 7.7.

A different picture would emerge if the FM domains were more extended, as for example in a PS scenario. They would then contain many energy levels (not only four as in Fig. 7.7) and should thus *not* give rise to a pseudogap.

For a more quantitative description we invoke the two-parameter UHA as described before. In Fig. 7.8 the UHA results, already in global quantization, are compared with those of unbiased MC simulations. The features of the spectral density are well reproduced. UHA even yields quantitative agreement as far as the pseudogap in the density of state is concerned.

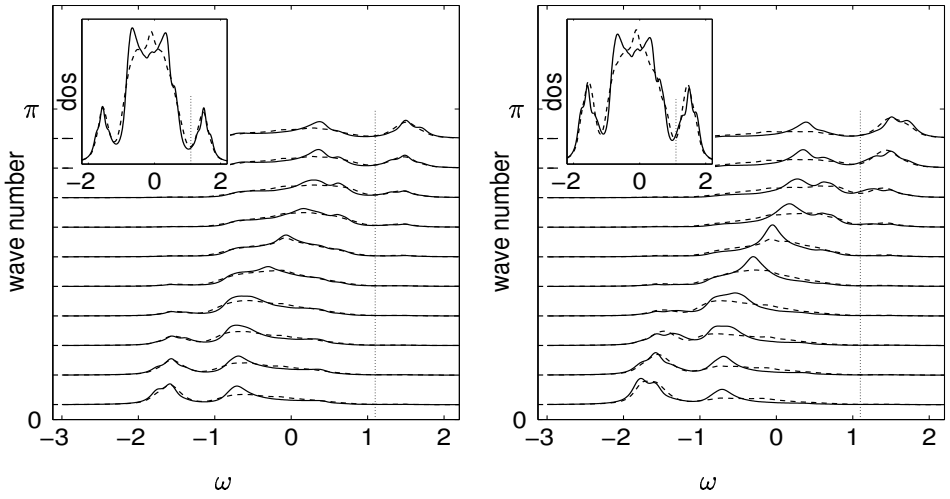

Figure 7.9: Spectral density for $N_h = 2$ holes (two polarons) in the left-hand panel and $N_h = 3$ holes (three polarons) in the right-hand panel. Parameters and meaning of symbols like in Fig. 7.8.

For the same value of the chemical potential $\mu = 1.1$, the two- and three- hole subspaces have been studied by projecting the grand canonical MC data on the $N_h = 2$ and $N_h = 3$ subspace, respectively. The results are depicted in Fig. 7.9. The spectra are qualitatively similar to those for the one-hole subspace. Only the spectral weight of the polaron peak increases and shoulders show up in the AFM part of the spectrum. They are due to the interstitial AFM regions enclosed by the FM-polaron wells. The argument is the same as before. The allowed energies are $\varepsilon(k) = -2\bar{u}_a \cos(k)$, but now the possible k-values depend on the size of the interstitial regions.

7.4.3 Discussion

The emerging global picture is as follows. There exists a critical chemical potential μ^*. The value of μ^* can be obtained from simplified energy considerations. For μ significantly above μ^*, the band is completely filled and antiferromagnetic. The spectral density in this case is shown in Fig. 7.6. At μ^*, according to Fig. 7.3, holes enter the e_g-band forming isolated FM domains each containing a *single* hole (see Figs. 7.4 and 7.5). In the grand canonical ensemble, the number of polarons strongly fluctuates and the height of the polaron peak in the spectrum is directly linked to the number of holes. The pseudogap appears around the critical chemical potential. For values below μ^*, the system switches from

predominantly AFM order to FM behavior and the pseudogap gradually disappears in favor of a single quasi particle band of tight-binding type. Our analysis yields compelling evidence against the PS scenario and in favor of FM polarons in 1D. Furthermore, it appears plausible that the formation of FM polarons will exist in symbiosis with lattice deformations (Jahn-Teller polarons) [16, 72].

For CMR oxides, Saitoh *et al* [73] have investigated the temperature dependence of angle resolved photoemission spectra (ARPES) for the phase transition from FM to PM order. These studies show that a pseudogap also develops above T_C, which can be rationalized in the polaron picture. In the PM phase we have the competition of ferromagnetism, driven by the DE mechanism, and spin disorder due to thermal fluctuations. Therefore, FM polarons will form in the paramagnetic background. They will, however, be more extended because the PM force is less pronounced than the AFM force at low temperatures [37]. With increasing temperature, the corespin fluctuations become stronger and the competition of the FM polarons with the PM background gets tougher. The existence of FM domains above T_C has been corroborated by neutron scattering experiments [74].

Furthermore, the ARPES experiments revealed that the bandwidth changes merely by about 4% across the FM to PM phase transition. On the other hand, it has been argued [73] that the DE model predicts a reduction of about 30% in the PM phase if there the mean angle between neighboring spins is taken to be $\pi/4$ and the mean hopping parameter is therefore reduced to $1/\sqrt{2}$. The authors in Ref. [73] therefore conclude that 'DE is probably not even the dominant mechanism ...'.

At first glance, the argument seems convincing. However, in the polaron picture we do not really expect such a dramatic change of the band width since it is determined by the polaronic peaks at $E = \pm 2\bar{u}_f \cos(\pi/(L_f + 1))$. Hence, the band edges depend on the hopping parameter of the FM region and not on that of the PM region. Moreover, by the same reasoning that leads to a bandwidth reduction of 30% in the PM state, one would expect that the bandwidth vanishes in the AFM phase at low temperatures, since here the neighboring corespins are mostly antiparallel. That conclusion is in strong contrast to the unbiased MC results depicted in Figs. 7.8 and 7.9. Even for the incoherent inner part of the spectrum, which is due to electronic motion in the AFM region, a considerable band width exists, due to the spin fluctuations which are present even at very low temperatures. On top of that, the band-edges at finite hole filling are not really determined by the AFM regime, but rather by the FM polarons.

7.5 Conclusions

In this paper, polaronic aspects of the ferromagnetic Kondo (double-exchange) model have been analyzed by unbiased finite temperature Monte-Carlo simulations and they have been explained by simple physical pictures. It has been found that in 1D, the physical effects of the FM Kondo model close to half

filling are not governed by phase separation, as previously reported, but rather by single-hole ferromagnetic polarons. They can be explained qualitatively on the back of an envelope by idealized polaron pictures.

It seems sensible to reassess the explanations of CMR based on PS. These explanations are primarily based on percolation ideas, which can equally well be applied to FM polarons as percolating units. It appears plausible that the formation of FM polarons will exist in symbiosis with lattice deformations (Jahn-Teller polarons). Single-hole FM polarons allow a direct explanation of the pseudogap, observed in the manganites, whereas for larger FM clusters the pseudogap would be filled up by additional states. The striking similarity of the bandwidth of the FM and the PM phase, observed in ARPES experiments, can also be explained by FM polarons in the frame of the DE model. Moreover, the infinite compressibility near the half filled band, which has previously been attributed to PS, is a consequence of the fluctuating number of polarons in the grand canonical ensemble. Work is in progress for higher-dimensional systems where the entropy is expected to have less influence on the thermodynamic behavior.

For the analysis of the Monte Carlo results, we have extended the uniform hopping approach (UHA) at finite temperatures to include polaronic effects. This ansatz reduces the numerical effort by several orders of magnitude, while retaining all crucial physical features. The key idea is to map the physics of the high-dimensional configuration space of the t_{2g} corespins onto an effective two-parametric model. A full thermodynamic evaluation of the UHA model takes into account entropy and fluctuations of the corespins. The results are in close agreement with the unbiased MC data and allow a realistic description of all FM polaron effects found in various physical quantities.

7.6 Acknowledgements

This work has been supported by the Austrian Science Fund (FWF), project no. P15834-PHY. We thank E. Dagotto for useful comments.

Chapter 8

Overall Conclusions

The aim of this work is to clarify several aspects of the ferromagnetic Kondo model, which is often applied to describe manganites. For that purpose an effective spinless fermion (ESF) model for the strong coupling multi-orbital ferromagnetic (FM) Kondo-lattice model is developed. The thereby reduced Hilbert space has the dimension of the corresponding double exchange (DE) model ($J_H \to \infty$). The comparison of Monte Carlo (MC) data shows the strikingly good performance of the effective model, even for moderate Hund coupling.

Although being of the same complexity like the DE model, it incorporates additional virtual spin-flip processes, which give rise to a pronounced antiferromagnetic (AF) coupling $J_{\text{eff}} = J' + 1/(2J_H)$ close to half-filling ($n = 1$). This effective coupling is crucial for the AF phase in this doping region.

An analysis of MC data for 1D chains exhibits two phase transitions from AF to FM order and vice versa, accompanied by a diverging compressibility (jump of the electron density as a function of the chemical potential). The critical chemical potential can be evaluated analytically using a uniform hopping approach (UHA), *i.e.* the fluctuating hopping parameters are replaced by a uniform mean value.

Canonical and grand canonical phase diagrams are determined in UHA for the 3D ESF model. Experimentally observed phases, like G-AF, A-AF, C-AF, and FM order are found, although grand canonical ensemble calculations show that only 3D AF and 3D FM order prevail. The transition between the two phases is accompanied by phase separation (PS) in UHA.

Calculations of 1D spectral functions show a remarkable center-symmetry. In the AF phase, at low and high electron density, a pseudo-gap structure is observed at the chemical potential and a mirror image at the opposite edge of the spectrum.

We further generalize UHA to make finite temperature calculations possible. The key idea is to map the physics of the high dimensional configuration space of the corespins onto an effective one-parametric model. The density of states

entering our approach can be determined by the Wang-Landau algorithm. Entropy and fluctuations of the corespins are thereby taken into account which allows a full thermodynamic evaluation. Tests for 1D systems reveal that UHA results are in close agreement with unbiased MC data for static and dynamic observables.

The FM to paramagnetic phase transition temperature of the one-orbital DE model for large 3D systems is determined by this method, yielding a Curie temperature that is comparable to the experimental data.

Unbiased finite temperature MC simulations of the 1D one-orbital FM Kondo model reveals features, which have been interpreted as PS in literature. An exhaustive analysis of the data leads to the conclusion that small single-hole FM polarons in an AF background rather account for the observed physical properties.

In order to underline our findings we extend the finite temperature UHA to include polaronic effects. This time the physics of the high-dimensional configuration space of the corespins is mapped onto an effective two-parametric model. One parameter accounts for the effective hopping parameter within the FM polaron, another parameter describes the hopping in the AF background. The results are in close agreement with the unbiased MC data and allow a realistic and intuitive description of all FM polaron effects found in various physical quantities.

In the light of this observations it might be necessary to reassess the explanations of CMR based on PS. These explanations are primarily based on percolation ideas, which can equally well be applied to FM polarons as percolating units. It appears plausible that the formation of FM polarons will exist in symbiosis with lattice deformations (Jahn-Teller polarons). Single-hole FM polarons allow a direct explanation of the pseudogap, observed in the manganites, whereas for larger FM clusters the pseudogap would be filled up by additional states. The striking similarity of the bandwidth of the FM and the PM phase, observed in ARPES experiments, can also be explained by FM polarons in the frame of the DE model. Moreover, the infinite compressibility near the half filled band, which has previously been attributed to PS, is a consequence of the fluctuating number of polarons in the grand canonical ensemble.

Based on this work an analysis of higher-dimensional systems, where the entropy is expected to have less influence on the thermodynamic behavior, should be carried out.

Furthermore the invocation of ESF in combination with UHA reduces the complexity of the model such that an incorporation of further degrees of freedom such as phonons and/or orbitals seems promising.

Appendix A

Asymptotic Estimate of $\Gamma_{N_p}(u)$ in the FM limit

This appendix is not included in the publication [9] and shall clarify the derivation of the asymptotic limit of $\Gamma_{N_p}(u)$.

We consider the nearest neighbor pair $< i, j >$ whose relative angle ϑ_{ij} is given by

$$\cos\vartheta_{ij} = u_i\, u_j + \sqrt{1-u_i^2}\,\sqrt{1-u_j^2}\,\cos(\phi_i - \phi_j)\ .$$

We expand this function about a ferromagnetic position ($u_i = u_j = 1, \phi_i = \phi_j = 0$). With $\partial\cos\vartheta_{ij}/\partial u_i = \partial\cos\vartheta_{ij}/\partial u_j = 1$ and $\partial\cos\vartheta_{ij}/\partial\phi_i = \partial\cos\vartheta_{ij}/\partial\phi_j = 0$ this yields to first order

$$\cos\vartheta_{ij} \approx 1 + (u_i - 1) + (u_j - 1) = u_i + u_j - 1\ .$$

The hopping amplitude then reads

$$u_{ij} = \sqrt{\frac{1+\cos\vartheta_{ij}}{2}} \approx \sqrt{\frac{u_i + u_j}{2}}\ .$$

Again we expand to first order,

$$u_{ij} \approx 1 + \frac{1}{4}\left(u_i - 1\right) + \frac{1}{4}\left(u_j - 1\right) = \frac{1}{2} + \frac{1}{4}\left(u_i + u_j\right)\ .$$

In order to obtain the average hopping amplitude, we sum over all N_p nearest neighbor pairs and divide by N_p.

$$u = \frac{1}{2} + \frac{1}{4N_p}\sum_{<i,j>}\left(u_i + u_j\right)$$

Assuming cyclic boundary conditions, in 1D ($N_p = L$) and in 3D ($N_p = 3L$) we find

$$u = \frac{1}{2} + \frac{1}{2L}\sum_i u_i$$

or, rearranging the terms

$$2L(1-u) = \sum_i (1-u_i) = \sum_i \delta u_i \ .$$

For a given u this is an equation for a hyperplane in the L-dimensional space of coordinates $\delta u_i > 0$. Therefore, the number of corespin states whose mean hopping amplitude lie in the interval $[u, 1]$ is

$$\int_u^1 \Gamma_{N_p}(u')\, du' = \frac{(2L)^L}{L!}\,(1-u)^L \ .$$

By differentiation we obtain the logarithm of $\Gamma_{N_p}(u)$ as

$$\log \Gamma_{N_p}(u) = (L-1)\,\log(1-u) + \text{const}$$

which is our asymptotic estimate for $\Gamma_{N_p}(u)$ in the ferromagnetic limit.

$\Gamma_{N_p}(u)$ in the AF limit

Unfortunately, this calculation cannot be carried out in the AF limit, because the square root would have to be expanded around zero, which does not work due to its divergent derivative. In 1D and for open boundaries one can calculate $\Gamma_{N_p}(u)$ exactly and then derive the asymptotic limit. All calculated cases ($L = 2, \ldots, 8$) yield

$$\log \Gamma_{N_p}(u) = (2L-1)\,\log(u) + \text{const}\,.$$

Bibliography

[1] E. Dagotto, T. Hotta, and A. Moreo, Colossal magnetoresistant materials: the key role of phase separation, Phys. Reports **344**(1-3), 1–153 (april 2001).

[2] M. Imada, A. Fujimori, and Y. Tokura, Metal-insulator transitions, Rev. Mod. Phys. **70**(4), 1039–263 (1998).

[3] G. H. Jonker and J. H. van Santen, Physica (Utrecht) **16**, 337 (1950).

[4] R. M. Kusters, J. Singleton, D. A. Keen, R. McGreevy, and W. Hayes, Magnetoresistance measurements on the magnetic semiconductor $Nd_{0.5}Pb_{0.5}MnO_3$, Physica B **155**, 362 (1989).

[5] R. von Helmholt, J. Wecker, B. Holzapfel, L. Schultz, and K. Samwer, Giant negative magnetoresistance in perovskitelike $La_{2/3}Ba_{1/3}MnO_x$ ferromagnetic films, Phys. Rev. Lett. **71**, 2331 (1993).

[6] A. Urushibara, Y. Moritomo, T. Arima, A. Asamitsu, G. Kido, and Y. Tokura, Insulator-metal transition and giant magnetoresistance in $La_{1-x}Sr_xMnO_3$, Phys. Rev. B **51**(20), 14103–14109 (may 1995).

[7] Y. Tokura, A. Urushibara, Y. Moritomo, T. Arima, A. Asamitsu, G. Kido, and N. Furukawa, Giant magnetotransport phenomena in filling-controlled Kondo lattice system: $La_{1-x}Sr_xMnO_3$, J. Phys. Soc. Jpn. **63**, 3931 (1994).

[8] W. Koller, A. Prüll, H. G. Evertz, and W. von der Linden, Effective spinless fermions in the strong-coupling Kondo model, Phys. Rev. B **66**, 144425 (2002).

[9] W. Koller, A. Prüll, H. G. Evertz, and W. von der Linden, Uniform Hopping Approach to the FM Kondo Model at finite temperature, cond-mat/ **0211672** (2002), accepted for publication in Phys. Rev. B.

[10] W. Koller, A. Prüll, H. G. Evertz, and W. von der Linden, Magnetic Polarons in the 1D FM Kondo Model, cond-mat/ **0301350** (2003).

[11] A. M. Oleś, M. Cuoco, and N. B. Perkins, Magnetic and Orbital Ordering in Cuprates and Manganites, in *AIP Conference Proceedings*, volume 527, pages 226–380, 2000.

[12] P. Allen and V. Perebeinos, Anti-Jahn-Teller polaron in $LaMnO_3$, Phys. Rev. B **60**(15), 10747–53 (oct 1999).

[13] H. A. Jahn and E. Teller, Proc. Roy. Soc. London A **161**, 220 (1937).

[14] J. Kanamori, J. Appl. Phys. Suppl. **31**, 14S (1960).

[15] J. Zaanen, G. A. Sawatzky, and J. W. Allen, Band Gaps and Electronic Structure of Transition-Metal Compounds, Phys. Rev. Lett. **55**(4), 418–421 (1985).

[16] D. M. Edwards, Ferromagnetism and electron-phonon coupling in the manganites, Adv. in Phys. **51**(5), 1259–1318 (2002).

[17] W. Nolting, *Quantentheorie des Magnetismus 1*, Teubner, 1986.

[18] T. Chatterji, editor, *Colosal Magnetoresistive Manganites*, chapter Theorie of Manganites, Kluwer Academic Publishers, 2002, cond-mat/0212466.

[19] A. Weiße, *Theoretische Untersuchungen magnetoresistiver Manganate*, PhD thesis, Universität Bayreuth, 2002.

[20] J. Kanamori, Prog. Theor. Phys. **30**, 275 (1963).

[21] J. S. Griffith, *The Theory of Transition-Metal Ions*, Cambridge, 1961.

[22] E. Dagotto, S. Yunoki, A. L. Malvezzi, A. Moreo, J. Hu, S. Capponi, D. Poilblanc, and N. Furukawa, Ferromagnetic Kondo Model for Manganites: Phase Diagram, Charge Segregation, and Influence of Quantum Localized Spins, Phys. Rev. B **58**(10), 6414–27 (sept 1998).

[23] K. Yosida, *Theory of Magnetism*, chapter 3.4, Springer, 1998.

[24] Y.-R. Chen and P. B. Allen, Spin versus Lattice Polaron: Prediction for Electron-Doped $CaMnO_3$, Phys. Rv. B **64**(6), 064401 (2001).

[25] J. B. Goodenough, A. Wold, A. J. Arnott, and N. Menyuk, Phys. Rev. **124**, 373 (1961).

[26] H. Y. Hwang, T. T. M. Palstra, S. W. Cheong, and B. Batlogg, Pressure effects on the magnetoresistance in doped manganese perovskites, Phys. Ref. B **52**, 15046 (1995).

[27] L. M. Rodriguez-Martinez and J. P. Attfield, Cation disorder and size effects in magnetoresistive manganese oxide perovskite, Phys. Ref. B **54**, R15622 (1996).

[28] A. Moreo, M. Mayr, A. F. S. Yunoki, and E. Dagotto, Giant Cluster Coexistence in Doped Manganites and Other Compounds, Phys. Rev. Lett. **84**, 5568 (2000).

[29] M. Mayr, A. Moreo, J. A. Vergés, J. Arispe, A. Feiguin, and E. Dagotto, Resistivity of Mixed-Phase Manganites, Phys. Rev. Lett. **86**, 135 (2001).

[30] R. Mathieu, P. Svedlindh, and P. Nordblad, Reentrant spin glass transition in $La_{0.96-y}Nd_yK_{0.04}MnO_3$: origin and effects on the colossal magnetoresistivity, Europhys. Lett. **52**, 441–447 (2000).

[31] J. Burgy, M. Mayr, V. Martin-Mayor, A. Moreo, and E. Dagotto, Colossal Effects in Transition Metal Oxides Caused by Intrinsic Inhomogeneities, Phys. Rev. Lett. **87**, 277202 (2001).

[32] M. B. Salamon and S. H. Chun, Griffiths singularities and magnetoresistive manganites, cond-mat/ **0301243** (2003).

[33] A. O. Sboychakov, A. L. Rakhmanov, K. I. Kugel, M. Y. Kagan, and I. V. Brodsky, Tunneling Magentoresistance of Phase-Separated Manganites, J. Exp. and Th. Phys. **95**(4), 753–761 (2002).

[34] R. A. Horn, *Matrix Analysis*, Cambridge University Press, 1990.

[35] H. G. Evertz, The Loop Algorithm, Adv. Phys. **52**, 1 (2003).

[36] T. A. Kaplan and S. D. Mahanti, *Physics of Manganites*, Kluwer Academic/ Plenum Publishers, New York, Boston, Dordrecht, London, Moscow, 1. edition, 1998.

[37] P. Horsch, J. Jaklic, and F. Mack, Double Exchange Magnets: Spin dynamics in the paramagnetic phase, Phys. Rev. B **59**(22), R14149–52 (jun 1999).

[38] J. Bala, A. M. Oles, and P. Horsch, Quasiparticles and the structure of orbital polarons in ferromagnetic LaMnO3, Phys. Rev. B **65**(13), 134420/1–15 (apr 2002).

[39] C. Zener, Phys. Rev. **82**, 403 (1951).

[40] N. Furukawa, *in: Physics of manganites*, Kluwer Academic Publisher, New York, 1. edition, 1998.

[41] S. Yunoki and A. Moreo, Static and Dynamical Properties of the Ferromagnetic Kondo Model with Direct Antiferromagnetic Coupling between the Localized t_{2g} Electrons, Phys. Rev. B **58**(10), 6403–13 (sept 1998).

[42] S. Yunoki, J. Hu, A. L. Malvezzi, A. Moreo, N. Furukawa, and E. Dagotto, Phase Separation in Electronic Models for Manganites, Phys. Rev. Lett. **80**(4), 845–8 (jan 1998).

[43] T. Hotta, A. L. Malvezzi, and E. Dagotto, Charge-orbital ordering and phase separation in the two-orbital model for manganites: Roles of Jahn-Teller phononic and Coulombic interactions, Phys. Rev. B **62**(14), 9432–52 (oct 2000).

[44] S. Yunoki, A. Moreo, and E. Dagotto, Phase Separation Induced by Orbital Degrees of Freedom in Models for Manganites with Jahn-Teller Phonons, Phys. Rev. Lett. **81**(25), 5612–15 (dec 1998).

[45] J. van den Brink and D. Khomskii, Double-exchange via degenerate orbitals, Phys. Rev. Lett. **82**(5), 1016–19 (feb 1999).

[46] W. von der Linden and W. Nolting, Electronic excitation spectrum of an antiferromagnetic semiconductor, Z. Phys. B **48**, 191 (1982).

[47] A. Auerbach, *Interacting Electrons and Quantum Magnetism*, Springer-Verlag, New York, Berlin, Heidelberg, 1. edition, 1994.

[48] S.-Q. Shen and Z. D. Wang, Phase separation and charge ordering in doped manganite perovskites: Projection perturbation and mean-field approaches, Phys. Rev. B **61**(14), 9532–41 (april 2000).

[49] S. Yarlagadda and C. S. Ting, Mean-field approach to charge, orbital, and spin ordering in manganites, Int. J. Mod. Phys. B **15**(19-20), 2719–26 (aug 2001).

[50] W. Koller, A. Prüll, H. G. Evertz, and W. von der Linden, Monte Carlo Approach to the FM Kondo model including Coulomb Repulsion, (2002), in preparation.

[51] A. Moreo, S. Yunoki, and E. Dagotto, Pseudogap Formation in Models for Manganites, Phys. Rev. Lett. **83**, 2773–2776 (october 1999).

[52] D. S. Dessau, T. Saitoh, C. H. Park, Z. X. Shen, P. Villella, N. Hamada, Y. Moritomo, and Y. Tokura, K-Dependent Electronic Structure, a Large "Ghost" Fermi Surface, and a Pseudogap in a Layered Magnetoresistive Oxide, Phys. Rev. Lett. **81**(1), 192 (1998).

[53] D. Meyer, C. Santos, and W. Nolting, Quantum effects in the quasiparticle structure of the ferromagnetic Kondo lattice model, J. Phys. Condens. Matter **13**, 2531–2548 (2001).

[54] W. Müller and W. Nolting, Temperature-dependent quasiparticle band structure of the ferromagnetic semiconductor EuS, Phys. Rev. B **66**, 085205 (2002).

[55] H. Yi, N. H. Hur, and J. Yu, Anomalous spin susceptibility and magnetic polaron formation in the double exchange systems, Phys. Rev. B **61**, 9501 (2000).

[56] Y. Motome and N. Furukawa, Critical temperature of Ferromagnetic Transition in Three-Dimensional Double Exchange Models, J. Phys. Soc. Jpn. **69**, 3785 (2000).

[57] A. Chattopadhyay, A. J. Millis, and S. Das Sarma, T=0 Phase Diagram of the Double-Exchange Model, Phys. Rev. B **64**(1), 012416 (2001).

[58] J. L. Alonso, L. A. Fernández, F. Guinea, V. Laliena, and V. Martín-Mayor, Hybrid Monte Carlo algorithm for the double-exchange model, Nucl. Phys. B **569**, 587 (2001).

[59] J. L. Alonso, J. A. Capitán, L. A. Fernández, F. Guinea, and V. Martín-Mayor, Monte Carlo determination of the phase diagram of the double-exchange model, Phys. Rev. B **64**, 54408 (2001).

[60] A. J. Millis, P. B. Littlewood, and B. I. Shraiman, Double Exchange Alone Does Not Explain The Resistivity of $La_{1-x}Sr_xMnO_3$, Phys. Rev. Lett. **74**(25), 5144–5147 (june 1995).

[61] H. Röder, R. R. P. Singh, and J. Zang, High-temperature thermodynamics of the ferromagnetic Kondo-lattice model, Phys. Rev. B **56**(9), 5084 (1997).

[62] P.-G. de Gennes, Effects of Double Exchange in Magnetic Crystals, Phys. Rev. **118**(1), 141–154 (april 1960).

[63] F. Wang and D. P. Landau, Determing the density of states for classical statistic models: A random walk algorithm to produce a flat histogram, Phys. Rev. E **64**(5) (november 2001).

[64] J. L. Alonso, L. A. Fernández, F. Guinea, V. Laliena, and V. Martín-Mayor, Variational Mean Field approach to the double-exchange model, Phys. Rev. B **63**, 54411 (2001).

[65] K. Binder and E. Luijten, Monte Carlo tests of renormalization-group predictions for critical phenomena in Ising models, Phys. Rep. **344**, 179–253 (2001).

[66] K. Binder and D. W. Heermann, *Monte Carlo Simulation in Statistical Physics - An Introduction*, Springer, Berlin, 1988.

[67] Y. A. Izyumov and M. V. Medvedev, Temperature-Dependent Pseudogaps in CMR Oxides, Sov. Phys.-JETP **32**, 302 (1971).

[68] W. Nolting, private communication (2002).

[69] E. L. Nagaev, *Colossal Magentoresistance and Phase Separation in Magnetic Semiconductors*, Imperial College Press, London, 1. edition, 2002.

[70] A. Moreo, S. Yunoki, and E. Dagotto, The Phase Separation Scenario for Manganese Oxides, Science **283**, 2034 (1999).

[71] T. Wu, S. B. Ogale, J. E. Garrison, B. Nagaraj, A. Biswas, Z. Chen, R. L. Greene, R. Ramesh, T. Venkatesan, and A. J. Millis, Electroresistance and electronic phase separation in mixed-valent manganites, Phys. Rev. Lett. **86**(26), 5998–6001 (2001).

[72] A. J. Millis, R. Mueller, and B. I. Shraiman, On the Fermi Liquid to Polaron Crossover I: General Results, Phys. Rev. B **54**, 5389–5404 (1996).

[73] T. Saitoh, D. S. Dessau, Y. Moritomo, T. Kimura, Y. Tokura, and N. Hamada, Temperature-Dependent Pseudogaps in Colossal Magnetoresistive Oxides, Phys. Rev. B **62**(2), 1039–43 (2000).

[74] T. G. Perring, G. Aeppli, and Y. Tokura, Antiferromagnetic short range order in a two-dimensional manganite exhibiting giant magnetoresistance, Phys. Rev. Lett. **78**, 3197 (1997).